Development of tissue-specific fluorescent contrast agents and direct application methods for improved clinical translation of fluorescence-guided surgery

Connor W. Barth

TABLE OF CONTENTS

LIST OF FIGURES

LIST OF TABLES

ACKNOWLEDGEMENTS

I would like to thank my mentor, Summer Gibbs, for all of the support and guidance towards my development as a researcher. I would also like to thank all of those who contributed to the science through experimental work or insightful discussion including Dr. Lei Wang, Dr. Vidhi Shah, Dr. Alexander Antaris, Dr. Jonathan Sorger, Jasmin Schaefer, Kayla Hackman, Meaghan McCoy, Broderick House, all of the members of the Gibbs lab, Dr. Theresa Koppie, Dr. Larry David, Dr. Scott Davis, Dr. Kimberley Samkoe, Dr. Margaret Folaron, Dr. Vince Rossi, and Rendy Strawbridge. Finally I would like to thank my family and friends for their love and support, especially my fiancé Shelby Mason for her unconditional care, patience, and motivation.

This work was funded by grants from the National Cancer Institute (R01CA188491), the Oregon Clinical and Translational Research Institute, and the National Institute of Biomedical Imaging and Bioengineering (K01-EB-010201, R01EB021362).

ABSTRACT

Over 300 million surgeries are performed worldwide each year. The ultimate goal of surgery is to repair damage or remove diseased tissues, while minimizing comorbidities by preserving vital structures such as nerves and blood vessels. However, surgeons still rely mainly on the basic tools of naked eye visualization and palpation for guidance during surgery, leaving incomplete resection rates high and comorbidities like nerve damage as a major problem. Fluorescence-guided surgery (FGS) has the potential to revolutionize surgery by enhancing visualization of specific tissues intraoperatively. Using optical imaging of targeted fluorescent probes, FGS offers sensitive, real-time, wide-field imaging using compact imaging systems that are easily integrated into the operating room. Several imaging systems are clinically available for FGS applications, however only a handful of contrast agents have been approved. Numerous preclinical studies for new agents have shown promise for improved surgical outcomes such as tumor resection or nerve-sparing. However, as non-curative diagnostic agents these new probes must overcome an enormous regulatory challenge to achieve clinical translation. The work presented herein has been carried out to develop novel targeted contrast agents for tumor margin detection and nerve identification as well as create more clinically viable administration methods to aid in their clinical translation. Utilizing local, direct administration rather than systemic administration to deliver these agents, microdose levels of the new compounds can be used in first-in-human trials under the exploratory investigational new drug (eIND) regulatory pathway, requiring substantially less preclinical toxicology testing. This work has applied this principle to antibody targeted probes for tumor margin detection during breast conserving surgery (BCS) using an innovative dual probe specimen staining method (DDSI) and novel nerve-specific small molecule fluorophores for improved nerve detection during procedures like the nerve-sparing

radical prostatectomy (RP). Following optimization of concentration, incubation, and washing parameters for each of these technologies, the direct administration methods developed herein were validated for their diagnostic accuracy and function in clinically relevant scenarios. Additional steps were taken toward clinical translation including the creation and screening of a library of novel nerve-specific fluorophores to identify candidate molecules for translation and development of clinically viable formulation strategies for their administration in the surgical field. Using the innovations developed herein, we anticipate clinical translation of these FGS technologies within the next five years, a rapid timeline for novel probes.

Chapter 1

Fluorescence image-guided surgery: promise and challenges

INTRODUCTION

Over 300 million surgeries are performed worldwide each year.[1] Despite many recent advances in the treatment of cancer and other diseases, surgery remains the most effective treatment option for a number of diseases and injuries.[2-5] The ultimate goal of surgery is to remove or repair tissues while minimizing comorbidities by preserving vital structures such as nerves and blood vessels. Recent technological advances including minimally invasive robot assisted laparoscopic surgery have improved outcomes and made it possible to perform difficult procedures robustly with minimal risk.[6-9] Furthermore, preoperative three-dimensional imaging technologies such as magnetic resonance imaging (MRI) and computed tomography (CT) have vastly improved diagnostic accuracy, staging, and preoperative planning.[10, 11] However, surgeons still rely mainly on the basic tools of naked eye visualization and palpation for guidance during surgery.

Identifying vital structures for preservation or tumor tissue for resection can be difficult using these methods alone. For instance, many breast tumors are non-palpable and 20-60% of patients undergoing breast conserving surgery are left with involved or close margins.[2, 12] Furthermore, iatrogenic nerve damage plagues many surgical procedures, including the nerve-sparing radical prostatectomy, after which up to 60% of patients report nerve damage despite efforts to preserve important nerve structures.[6, 13, 14] The current intraoperative guidance techniques, or lack thereof, handicap a surgeons ability to successfully complete the goals of a procedure. Therefore, an imaging modality that can provide intraoperative guidance by highlighting important tissues or structures would greatly benefit surgical outcomes and significantly reduce comorbidities.

FLUORESCENCE GUIDED SURGERY

Fluorescence-guided surgery (FGS) has the potential to revolutionize surgery by enhancing visualization of specific tissues intraoperatively, effectively bridging the gap between preoperative imaging and surgical guidance. Using optical imaging of targeted fluorescent probes, FGS offers sensitive, real-time, wide-field imaging using compact imaging systems that are easily integrated into the operating room. Several imaging systems have already been developed for FGS applications and are

in use clinically.[15-23] Utilizing near-infrared (NIR) light (650-900 nm), many of these systems can identify targeted tissue at millimeter to centimeter imaging depths due to the increased tissue penetration of light and minimal background autofluorescence at these wavelengths (**Fig. 1.1**).[24, 25] Additionally, the use of NIR light allows these systems to be implemented in the surgical field without affecting conventional white light visualization. FGS systems have been successfully utilized in a wide variety of clinical applications to improve outcomes, including tumor resection, sentinel lymph node mapping, angiography, lymphography, and ureter and bile duct anatomic imaging.[26-38] For example, FGS applications in glioma resection using 5-aminominolevulinic acid (5-ALA) and its fluorescent metabolite protoporphyrin IX (PpIX) has significantly enhance complete resection rates and revolutionized neurosurgical treatment of brain tumors over the past decade.[39] The promise of FGS has been demonstrated in a variety of clinical and preclinical applications over the past several decades, however few efforts in clinical translation of new targeted imaging agents for FGS have been successful, largely due to the enormous regulatory challenge and cost of introducing diagnostic imaging agents into the clinic.

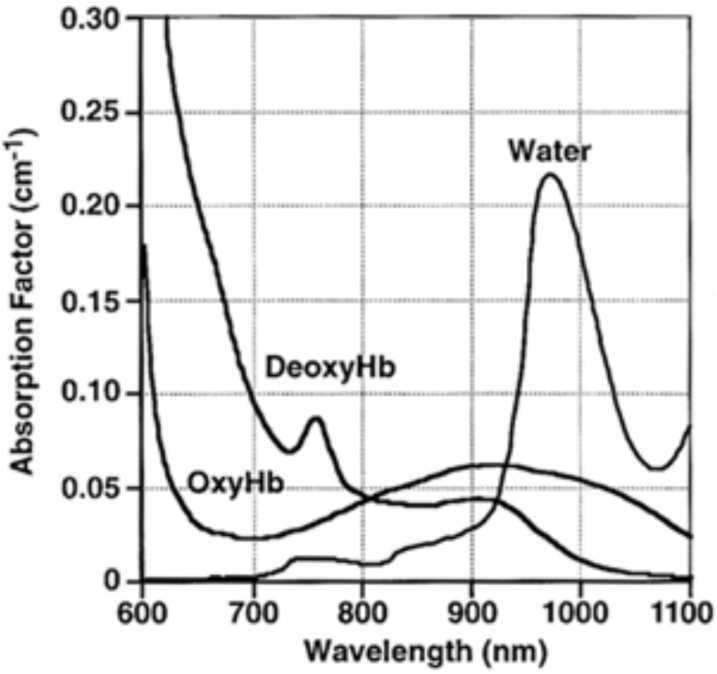

Figure 1.1. Absorption spectra of endogenous tissue components. Due to low absorbance of all major tissue components between 650 - 900 nm, the near-infrared (NIR) is the optimal medical optical imaging window. OxyHb = oxygenated hemoglobin, DeoxyHb = deoxyhemoglobin. Figure reprinted from Chance.[24] With permission. Copyright Clearance Center Rightslink.

CLINICAL TRANSLATION: ITS CHALLENGES

Although many FGS imaging systems are available for clinical use, only four fluorescent contrast agents are clinically approved, three of which were grandfathered in from their application as colorimetric dyes prior to the widespread use of fluorescence imaging.[25] Of these four dyes, only two, indocyanine green (ICG) and methylene blue, emit NIR fluorescence and both are blood pool agents. There is a great need for the development and clinical translation of tissue-specific fluorescent contrast agents for FGS. However, as non-curative diagnostic agents not requiring long term administration, there is low financial incentive for their development and translation, resulting in a lack of investment from commercial sources.[40, 41] This makes clinical translation challenging, as most preclinical development must be done through academic institutions with early clinical work requiring additional federal grants. Therefore, any effort to ease the regulatory burden on clinical translation of this promising technology would aid in translation to the clinic.

One option for easing the regulatory burden for first-in-human studies of new agents is to utilize the food and drug administration's (FDA's) exploratory investigational new drug (eIND) pathway. First in human studies conducted under an eIND require significantly less preclinical toxicology testing by allowing researchers to administer "microdoses" denoted as less than 100 μg or 30 nmol per administration for small molecule or protein products, respectively.[42] Due to the lower administered dose, substantially fewer preclinical toxicology studies are required prior to first-in-human clinical trials as compared to traditional translation under an IND, allowing proof of concept phase 0 studies to be performed with relative ease and significantly decreased financial burden (**Fig. 1.2**). This alternative route to clinical use has been utilized with success in the recent phase 0 clinical trials of a promising tumor targeted FGS affibody probe ABY-029.[43, 44] Thus, eIND guidance offers a promising alternative for ease of clinical translation for new FGS imaging probes.

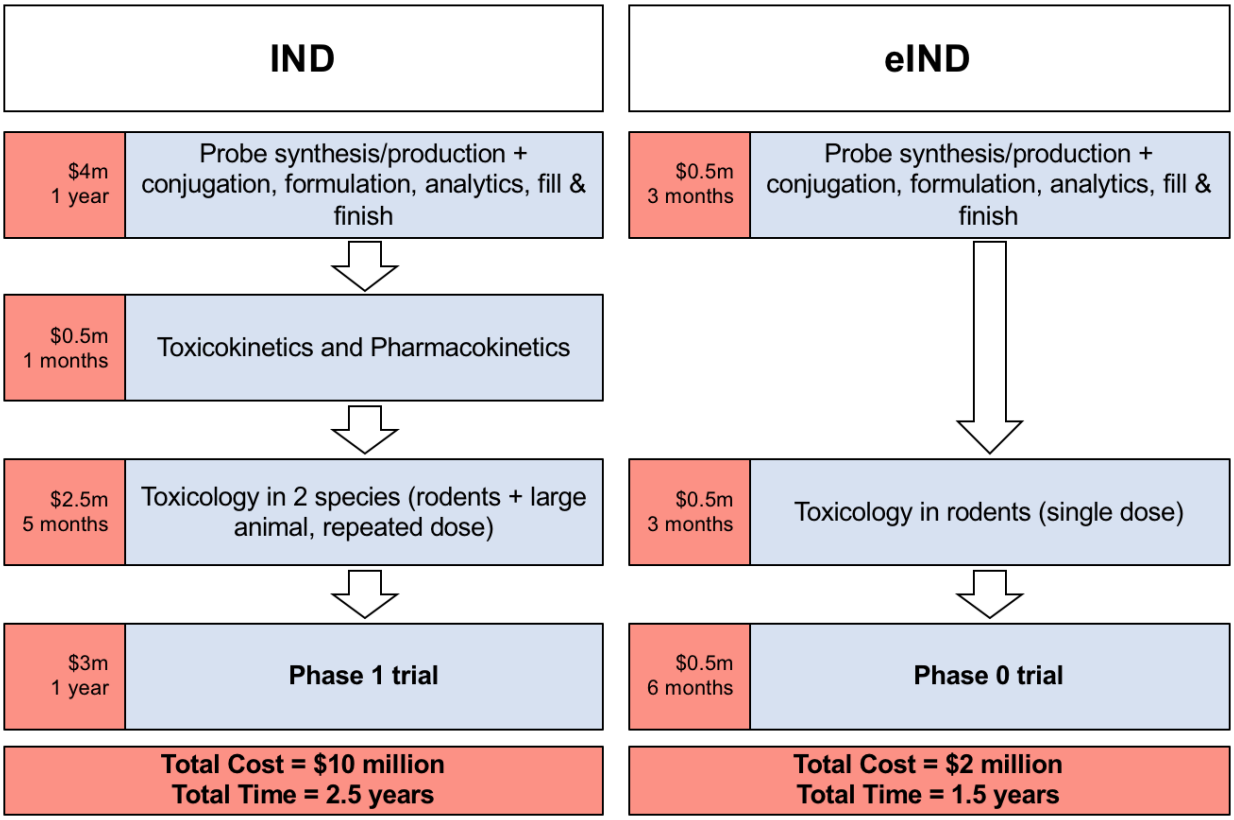

Figure 1.2. Comparison of steps, cost and time required for Phase I trial under a traditional IND vs. a Phase 0 trial under an exploratory IND (eIND). A traditional IND requires more steps and significantly more cost, while a eIND is shorter and can be financed through a single National Institute of Health (NIH) grant. Figure adapted from Jacobson-Kram & Mills, *Clin Cancer Res* **14** (2008) and Pogue et al., *Proc SPIE Int Soc Opt Eng* (2015).

DIRECT APPLICATION

A major challenge with introducing new imaging agents for clinical use via an eIND is that administering probes in the microdosing range can yield low fluorescence signals, making it difficult to obtain contrast over autofluorescence. Systemically administered probes are subject to the body's biodistribution and clearance, which can mask specific binding due to low levels of accumulation following administration of a microdose in the targeted tissue. One method for ensuring adequate binding in the tissue of interest and improving sensitivity for eIND studies is direct administration at the surgical site. By directly applying the fluorescent probe to the tissues of interest within the surgical field, selective labeling can be attained with a significantly lower dose than systemic administration, yielding

equivalent to higher intensity fluorescence signal in the tissue of interest. Aside from significantly lowering the required dose for signal, direct administration provides rapid and highly selective staining, which is beneficial for certain applications to avoid unwanted background signal that can be caused upon systemic administration. Additionally, direct administration methods can be utilized in retrospective analysis of excised tissues such as tumors for tumor margin detection, allowing for indirect, yet still rapid FGS and post-surgical diagnostics.

TUMOR MARGIN DETECTION

Post-surgical tumor margin status is one of the most important prognostic factors for local cancer recurrence and is considered the main measure of a tumor resection's success.[12, 45-47] Patients undergoing breast conserving surgery (BCS), the most common treatment option for patients with early stage breast cancer, are left with involved or close surgical margins 20-60% of the time, determined by pathological assessment following completion of the surgery.[2, 12] Involved or close margins require follow up re-excision surgery and result in negative patient outcomes.[12, 48-51] FGS offers a rapid and accurate approach to intra-surgical margin assessment that does not compromise tissue integrity. Direct administration of tumor-specific fluorescent probes to resected specimens is an attractive alternative to systemic administration that incurs no risk of toxicity to the patient and would provide an extremely rapid route to the clinic. However, early efforts to stain tissues in this manner resulted in high non-specific uptake and poor tumor to normal tissue contrast. Use of a dual probe staining approach, containing a targeted and untargeted probe, enabled correction for non-specific uptake resulting in highly specific tumor signal.[52] With spectrally distinct fluorescence signals, the dual probe stain removes nonspecific signal via the subtraction of the untargeted signal from the targeted signal followed by division of the untargeted signal. This yields a ratiometric image that depicts the specific binding of the targeted probe to the biomarker.

FLUORESCENCE GUIDED NERVE VISUALIZATION

Iatrogenic nerve injury plagues surgical outcomes, affecting up to 63 million patients worldwide per year.[13, 53] These rates remain high despite efforts to improve

nerve sparing in procedures that have a high incidence of injury. For example, nerve sparing radical prostatectomy (RP) methods have been practiced for over 30 years, but up to 60% of patients report nerve damage post-surgery.[6, 13, 14] Currently, surgeons rely mainly on naked eye visualization to identify nerve tissue during RP. However, positive nerve identification remains difficult due to the depth and narrowness of the pelvis as well as the small size of nerves surrounding the prostate and thus the degree of nerve sparing is positively correlated to a surgeon's experience level.[54] Nerve stimulation and several imaging modalities have been employed to aid in the identification of nerve tissue during RP including transrectal ultrasound, optical coherence tomography, and confocal endomicroscopy.[55-60] However, these lack specificity, resolution, and wide-field imaging functionality, making it difficult to identify nerve tissues in real time. FGS is well suited to aid in the preservation of these vital structures.

Direct administration is an especially suited administration strategy for fluorescence-guided nerve sparing RP because nerve labeling via systemic administration would generate high background from nerves in the prostate, which are not able to be spared, and renal nerve-specific fluorophore clearance generates significant fluorescence in the urine within the adjacent bladder.[61-63]

Currently, no NIR nerve-specific fluorophore exists and further fluorophore development is required to obtain a proper candidate for clinical translation. Several classes of nerve specific fluorophores have been studied for FGS.[20, 64-74] Of these, the Oxazine fluorophore scaffold is the most promising candidate for development of a NIR nerve-specific agent, where the lead candidate, Oxazine 4, shows high nerve-specificity and red shifted absorption and emission spectra close to the NIR wavelengths.[74]

THESIS OUTLINE

This thesis describes work undertaken to develop novel fluorescent probes and direct application methods for FGS. The work presented herein represents significant progress in the development and characterization of clinically viable administration methods and novel imaging probes for tumor margin detection and nerve identification. **Chapter 2** describes the development of a direct dual-probe staining method for resected breast tumor specimens that allows for highly specific

tumor biomarker imaging in mouse orthotopic tumor models. In **Chapter 3**, the development of a direct administration method for staining nerve tissue using small molecule, nerve-specific fluorophores is outlined and several major advantages of direct administration are identified. **Chapter 4** reports on the development and screening of a library of nerve-specific, small molecule fluorophores based on the oxazine fluorophore scaffold and identifies several promising NIR candidates for clinical translation. In **Chapter 5** and **Chapter 6** novel formulation strategies are explored for the lead nerve-specific fluorophores for direct and systemic administrations, respectively. **Chapter 7** provides a summary of the results presented herein and gives perspectives into future work.

Chapter 2

Optimizing fresh specimen staining for rapid identification of tumor biomarkers during surgery

This manuscript was originally published in *Theranostics*. Barth, C.W., Schaefer, J.M., Rossi, V.M., Davis, S.C. & Gibbs, S.L. Optimizing fresh specimen staining for rapid identification of tumor biomarkers during surgery. *Theranostics* 7, 4722-4734 (2017).

ABSTRACT

Rationale: Positive margin status due to incomplete removal of tumor tissue during breast conserving surgery (BCS) is a prevalent diagnosis usually requiring a second surgical procedure. These follow-up procedures increase the risk of morbidity and delay the use of adjuvant therapy; thus, significant efforts are underway to develop new intraoperative strategies for margin assessment to eliminate re-excision procedures. One strategy under development uses direct application of dual probe staining and a fluorescence imaging strategy termed dual probe difference specimen imaging (DDSI). DDSI uses a receptor-targeted fluorescent probe and an untargeted, spectrally-distinct fluorescent companion imaging agent directly applied to fresh resected specimens, where the fluorescence from each probe is imaged and a normalized difference image is computed to identify tumor-target distribution in the specimen margins. While previous reports suggested this approach is a promising new tool for surgical guidance, advancing the approach into the clinic requires methodical protocol optimization and further validation.

Methods: In the present study, we used breast cancer xenografts and receiver operator characteristic (ROC) curve analysis to evaluate a wide range of staining and imaging parameters, and completed a prospective validation study on multiple tumor phenotypes with different target expression. Imaging fluorophore-probe pair, concentration, and incubation times were systematically optimized using n=6 tissue specimen replicates per staining condition. Resulting tumor vs. normal adipose tissue diagnostic performance were reported and staining patterns were validated via receptor specific immunohistochemistry colocalization. Final staining conditions were tested in receptor positive and receptor negative cohorts to confirm specificity.

Results: The final staining conditions were found to be a one minute stain in a 200 nM probe solution (area under the curve (AUC) = 0.97), where the choice of fluorescent label combination did not significantly affect the diagnostic performance. Using an optimal threshold value determined from ROC curve analysis on a training data set, a prospective study on xenografts resulted in an AUC=0.95 for receptor positive tumors and an AUC = 0.50 for receptor negative (control) tumors, confirming the diagnostic performance of this novel imaging technique.

Conclusions: DDSI provides a robust, molecularly specific imaging methodology for identifying tumor tissue over benign mammary adipose tissue. Using a dual probe imaging strategy, nonspecific accumulation of targeted probe was corrected for and tumor vs. normal tissue diagnostic potential was improved, circumventing difficulties with *ex vivo* tissue specimen staining and allowing for rapid clinical translation of this promising technology for tumor margin detection during BCS procedures.

INTRODUCTION

Breast conserving surgery (BCS), including partial mastectomy and lumpectomy, remains the most common treatment option for patients with early stage breast cancer and is carried out for 61% of the ~200,000 breast cancer patients diagnosed annually in the United States.[2] However, despite recent technological advances and efforts to improve surgical methods, 20-60% of these patients are left with involved or close surgical margins, determined by pathological assessment following completion of the surgery.[2, 12] Pathological findings of involved or close margins require follow up re-excision surgery within days to weeks of the original excision, resulting in increased risk of morbidity, undue patient stress, increased cost to both the patient and healthcare system, as well as delay of adjuvant therapy, all negatively affecting patient outcomes.[12, 48-51] Technologies currently deployed in the clinic to improve margin detection include frozen section analysis (FSA),[75] touch prep cytology,[76] specimen radiography,[77] specimen ultrasound,[78] and radiofrequency spectroscopy.[79] Each technique has shown improvement in tumor re-excision rates, but sensitivity and specificity performance has been mixed and lengthy tissue processing procedures in some cases limit translation to the clinic.[75, 76, 80-88]

It has thus been recognized that rapid, accurate approaches that do not compromise tissue integrity are needed and widespread efforts are underway to develop novel approaches for intra-surgical margin assessment. A multitude of optical techniques are under development for this application.[16, 76, 89-102] These strategies are in various stages of clinical translation where the ability to produce high contrast and high-resolution images have been demonstrated, but requirements of long scan times and *in vivo* application of exogenous contrast agents diminish clinical viability. While *in vivo* administration of fluorescent contrast agents is attractive, since it enables imaging guidance within the surgical cavity, the availability of clinically approved contrast agents is limited and securing approval for new agents with appropriate safety profiles is a long and challenging process.[25, 103] Direct application of tumor-specific fluorescent probes is a conceptually simple approach to identify tumor in specimen margins and an appealing alternative to the difficulties of *in vivo* contrast agent administration. In one iteration of this approach, activatable fluorescent probes were used to detect the presence of tumor-specific enzyme, marking positive tumor margins.[104-106] An orthogonal approach uses

fluorescently-labeled tumor targeting moieties (such as antibodies, antibody fragments, peptides, etc.) to rapidly stain, wash and image the excised specimen. In principle, this technique enables rapid tumor-receptor-specific staining of the specimen without compromising follow-up pathology and doesn't require the safety profile of agents administered *in vivo*.

However, early efforts to deploy this simple strategy produced non-specific uptake of targeted fluorescent probes in normal tissue despite efforts to apply blocking solution prior to staining, particularly in surrounding adipose tissue, a main component of resected breast specimens. Thus, simple, single-agent staining of excised tissue specimens, including tissues from BCS resulted in poor diagnostic performance. To address this, we and others have shown that non-specific uptake can be quantified and removed by including a second non-specific companion imaging probe in the staining solution and that the targeted and untargeted images together improve cancer detection.[52, 98-102, 107] In this paradigm, each probe is labeled with a spectrally-distinct fluorophore, enabling the specific and non-specific probe distribution to be assessed with multi-color imaging. The targeted and untargeted probe pairs are chosen to have similar molecular weights in an attempt to ensure similar tissue transport kinetics of both agents. Therefore, the normalized difference between the targeted and untargeted probes' fluorescence emphasizes the difference between each probe's uptake, enhancing the signal from the tumor biomarker-targeted probe. The resulting image is thus a direct representation of the targeted probe's specific binding to the tumor biomarker. We have termed this approach Dual-Probe Difference Specimen Imaging (DDSI). We previously reported a proof-of-concept study for the DDSI technique using a HER2-targeted probe and a spectrally distinct untargeted probe[52] While the DDSI technique showed a significant increase in tumor to surrounding adipose tissue contrast and improved diagnostic performance when compared to targeted stain alone, the staining protocol was not optimized for speed and diagnostic accuracy, and many questions remained unanswered. To date, a full investigation of the relevant parameter space, including stain concentration, incubation times, and fluorescent labels has not been reported.

In this study, we explored this parameter space in an effort to optimize the DDSI staining protocol for future clinical translation. Throughout this study, we used receiver operator characteristic (ROC) curve analysis as the metric of evaluation, and acquired confirmatory immunohistochemistry (IHC) and hematoxylin and eosin (H&E) stained microscopy images of tissue samples. In the

first set of experiments, we examined the effect of stain concentration and incubation time on the diagnostic performance of HER2-targeted DDSI imaging, with the aim of choosing the condition that provided the highest diagnostic performance in a short time. Next, in an effort to confirm that the reported diagnostic performance was not driven or otherwise affected by the binding behavior of the fluorescent label itself, an underappreciated issue in fluorescence imaging of tissue,[108] we examined the effect of switching the fluorescent labels between targeted and untargeted probes. Finally, to evaluate the diagnostic performance in a semi-blinded, pre-clinical study, we used ROC curve analysis on a training data set to define an optimal diagnostic threshold and applied this result prospectively to a data set that included normal tissue, HER2(+) tumors and HER2(-) tumors.

MATERIALS & METHODS

General Study Design

The three primary objectives of this study were:

1. Identify a tissue staining/washing protocol that provided high diagnostic performance within a clinically relevant time frame that stained the target-of-interest. This was accomplished by repeating DDSI imaging for different staining concentrations and incubation times (100 and 200 nM, 1 and 10 min), where six replicates per condition were completed (**Fig. 2.1**). The concentration range and incubation times tested herein were chosen to determine the effect of increased concentration and decreased incubation time on stain performance, with the 100 nM concentration, 10 min incubation time utilized in preliminary studies.[52]
2. Confirm that the fluorophore label did not have a major impact on diagnostic performance. This was accomplished by repeating all staining conditions (100 and 200 nM, 1 and 10 min, 6 replicates per condition), with the fluorescent labels reversed between the targeted and untargeted probes (**Fig. 2.1**).
3. Determine the diagnostic accuracy of the final DDSI method. This was accomplished by selecting the most clinically viable staining condition once parameter testing studies were completed with 6 replicate tumor and adipose tissue pairs per condition. A diagnostic threshold derived from ROC curve analysis on a training data set was then determined and used on a prospective testing data set that included normal tissue, HER2(+) and HER2(-) tumors. Six

replicates per HER2 expression condition were used for the testing data set experiments.

For each replicate, tumor and normal adipose tissues were stained with the DDSI protocol resulting in a total of 60 tissue pairs. Color and fluorescence images were acquired using a custom-built widefield imaging system capable of acquiring co-registered images of each probe's fluorescence. Following DDSI image processing and analysis, each condition's performance was evaluated using ROC curve analysis as assessed through the area under the curve (AUC) to determine tumor vs. normal tissue diagnostic performance. Confirmatory Her2-IHC and H&E were also completed for each sample.

Fluorophores & Antibodies

Alexa Fluor 647 (AF647, Thermo Fisher Scientific, Waltham, MA) and Cy3B (GE Healthcare Life Sciences, Little Chalfont, UK) were used for all fluorescence imaging studies. These fluorophores were selected because they are photostable, have relatively high quantum yields and are readily available. Each fluorophore was purchased in its N-hydroxysuccinimide (NHS) ester form and solubilized in anhydrous DMSO at 10 mM for antibody conjugation reactions. Trastuzumab (Herceptin, Genentech, South San Francisco, CA, molecular weight (MW) = 145.5 kDa) was used as the targeted probe for all studies. Lyophilized Herceptin was made into a stock solution at 2 mg/mL using 1x phosphate buffered saline (1x PBS) at pH 7.4. Donkey anti-rabbit IgG (Jackson ImmunoResearch, West Grove, PA, MW = 150 kDa) was used as the untargeted probe for all studies.

Mice & Cell Lines

The MCF7 parent line and MCF7 cell line transfected with HER2/neu (MCF7-HER2) [109] were grown to 90% confluence and harvested for tumor implantation. 32-38 day old female athymic nude mice (Homozygous 490, Charles Rivers Labs, Wilmington, MA) weighing 19-21 g were used for growth of MCF7-HER2 and MCF7 tumor xenografts. All animal studies were approved by the Institutional Animal Care and Use Committee (IACUC) at Oregon Health and Science University (OHSU).

Tumor Implantation & Growth

Four days prior to MCF7-HER2 implantation, mice were implanted with 0.72 mg/pellet 90-day release 17β-estradiol pellets (Innovative Research of America, Sarasota, FL), explained as follows. One hour prior to pellet implantation, mice were injected intraperitoneally (IP) with 0.05 mg/kg buprenorphine (Reckitt Benckiser Pharmaceuticals Inc., Slough, UK) to mitigate any pain from the procedure. Mice were then anaesthetized with 100 mg/kg ketamine (Hospira Inc., Lake Forest IL) and 10 mg/kg xylazine (AnaSed, Shenandoah, IA) injected IP. Depth of anesthesia was assessed using the toe pinch method to ensure mice were fully anesthetized prior to any surgical manipulation. In a sterile surgical field, the lateral dorsal neck of the mice was sterilized with povidine-iodine (Purdue Products, Stamford, CT). A small incision (~5 mm) was made on the right side of the neck between the right ear and shoulder using autoclaved instruments and a single 17β-estradiol pellet was placed beneath the skin using a 10-gauge trochar (Innovative Research of America, Sarasota, FL). The incision was sealed with Vetbond™ (3M, St. Paul, MN) and monitored over the next week for healing. Estradiol implantation is necessary for MCF7 cell line tumorigenicity.[109]

Four days later, MCF7-HER2 tumors were implanted, detailed as follows. Mice were anaesthetized with 100 mg/kg ketamine and 10 mg/kg xylazine injected IP. The peritoneal region of the animal was sterilized with providine-iodine in a sterile surgical field. A small incision (~3 mm) was made bilaterally adjacent to the inferior nipple on the left and right sides of each mouse. Forceps were used to retract the mammary adipose pad through the incision followed by a 200 μL injection of MCF7-HER2 cell suspension ($1x10^6$ cells) into each mammary adipose pad. The injected mammary adipose pad was carefully inserted back through the incision after which the incision was sealed with Vetbond™. All incisions were monitored daily for a week to ensure healing. Mice were monitored weekly for tumor growth and overall health. The tumors were allowed to grow for 4-6 weeks or until tumor diameter reached 1 cm^3 as measured by calipers.

The training data set consisted of a cohort of 15 mice implanted with MCF7-HER2 tumors bilaterally for determination of the final dual probe staining concentration and incubation time. Of the 30 total implantation sites, 24 tumors grew, which were bisected and used in the parameter testing studies. A second cohort of 2 mice were implanted with MCF7-HER2 tumors for a testing set for staining

with the selected probe pair, protein concentration and incubation time. Of the 4 total implantation sites, 3 tumors grew, which were bisected and used in the testing set. An additional cohort of 3 mice were implanted with the MCF7 parent cell line bilaterally for a testing set with HER2 negative tumors. Of the 6 total implantation sites, 3 tumors grew, which were bisected and used in the testing set.

Antibody-Fluorophore Conjugations

Each antibody was conjugated to each fluorophore, resulting in the following labeled antibodies: Herceptin-AF647, Herceptin-Cy3B, DkRb-AF647, and DkRb-Cy3B, which were prepared individually as follows. The antibody was buffer exchanged into 1x PBS, pH 8.0 at a concentration of 2.0 mg/mL for Herceptin and 1.3 mg/mL for DkRb. 1.5 µL of the 10 mM fluorophore stock solution in anhydrous DMSO was added to 220 µL of Herceptin and 1 µL of 10 mM fluorophore stock solution in anhydrous DMSO was added to 220 µL of DkRb, resulting in a 5:1 fluorophore to antibody molar ratio in a total volume of 1 mL. The mixture was shaken gently at room temperature for 3 h protected from light. The resulting mixture was concentrated in 10 kDa molecular weight cut off spin filter (MWCO, Amicon® Ultra 0.5 mL 10 kDa, Fisher Scientific, Waltham, MA) into a clean microcentrifuge tube to remove unreacted fluorophore, followed by purification through a 6 kDa MWCO desalting column (Bio-Scale™ Mini Bio-Gel® P-6 5 mL, Bio-Rad, Hercules, CA) using a fast protein liquid chromatography system (FPLC, NGC Quest™ 10 Plus, Bio-Rad, Hercules, CA). The fluorophore to protein ratio for each antibody conjugate was quantified using absorbance spectroscopy (SpectraMax M5 Microplate Reader, Molecular Devices, Sunnyvale, CA). The antibody absorbance was measured at 280 nm (Herceptin extinction coefficient = 225,000 $M^{-1}cm^{-1}$, Donkey anti-rabbit extinction coefficient = 210,000 $M^{-1}cm^{-1}$). Cy3B absorbance was measured at 560 nm (Cy3B extinction coefficient = 130,000 $M^{-1}cm^{-1}$), while AF647 absorbance was measured at 650 nm (AF647 extinction coefficient = 270,000 $M^{-1}cm^{-1}$). Calibrated absorbance and fluorescence spectra and the Beer-Lambert law were used to determine the concentration of fluorophore and antibody for each conjugate.[110] All fluorophore-to-antibody ratios used in this study were between 3:1 and 4:1.

DDSI staining solution was made by mixing Herceptin-AF647 with DkRb-Cy3B or Herceptin-Cy3B with DkRb-AF647 in a solution containing 1x PBS pH

7.4, 0.1% Tween-20, and 1% bovine serum albumin (BSA). Final antibody solution concentrations and probe mixtures used for DDSI staining studies were as follows: Herceptin-Cy3B + DkRb-AF647 at concentrations of 100 and 200 nM measured by protein concentration and Herceptin-AF647 + DkRb-Cy3B at concentrations of 100 and 200 nM measured by protein concentration.

Tumor Resection & DDSI Staining

MCF7-HER2 tumor bearing mice were euthanized using CO_2 asphyxiation followed by cervical dislocation after 4-6 weeks of tumor growth or a maximum tumor size of 1 cm^3. Tumors were extracted and bisected prior to DDSI staining, with bisected pairs being used to test different staining conditions. Bisection would not be necessary in clinical use, but was performed in this study in order to test multiple conditions using the same tumor for increased control over potential variation in specimen composition. For each bisected tumor sample, a corresponding mammary adipose sample was extracted from each mouse. MCF7-HER2 tumor and mammary adipose samples were stained and washed together following a previously published procedure (**Fig. 2.1A**).[52] Briefly, tumor and adipose sample pairs were incubated in 1 mL of 2% BSA in PBS blocking solution for 10 min. Then each sample pair was incubated in 1 mL of DDSI staining solution for 1 or 10 min. Specimens were stained with both probes simultaneously to minimize the required staining time, making the technique feasible for integration into routine clinical workflow. Each DDSI stained sample pair was transferred to 50 mL of wash solution composed of 0.1% Tween-20 in PBS and gently agitated for 5 min. Tumor and adipose pairs were immediately transferred to glass slides for imaging with the bisected cut face facing up towards the light source and camera. With two staining solutions at two concentrations (100 and 200 nM) and two incubation times (1 and 10 min) a total of 48 bisected tumor and mammary adipose pairs were collected resulting in n=6 tissue pairs per DDSI staining condition for the parameter testing studies (**Fig. 2.1B**). Following selection of the most clinically viable staining parameters, an additional testing cohort consisting of n=6 MCF7-HER2 and n=6 MCF7 tumor specimens were stained and imaged for validation of DDSI method's diagnostic ability and subsequent immunohistochemical (IHC) analysis, making a total of 60 tissue pairs stained and measured for this study.

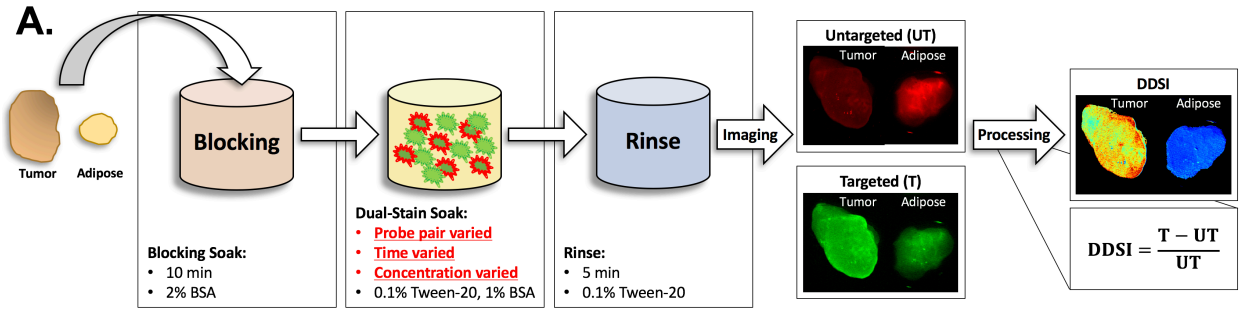

B.

Probe Pair A: Targeted: Herceptin – Cy3b, Untargeted: Dk-anti-Rb – AF647			Probe Pair B: Targeted: Herceptin – AF647, Untargeted: Dk-anti-Rb – Cy3b		
	Incubation Time:			Incubation Time:	
Stain Concentration:	1 min	10 min	Stain Concentration:	1 min	10 min
100 nM	x	x	100 nM	x	x
200 nM	x	x	200 nM	x	x

Fig. 2.1: *Staining protocol and experimental conditions*. **(A)** Schematic of DDSI staining protocol and imaging approach. The parameters for each step of the staining protocol are listed in their respective boxes. The dual-stain soak experimental parameters that were tested are highlighted in red. DDSI image processing was performed by subtracting the untargeted image from the targeted image and then dividing by the untargeted image as shown. **(B)** Table of experimental conditions tested to optimize the staining protocol.

DDSI Macroscopic Imaging

Tumor and adipose tissue pair imaging was performed using a custom-built wide field imaging system consisting of a QImaging EXi Blue monochrome camera (Surrey, British Columbia, CA) for fluorescence detection with a removable Bayer filter for collecting co-registered color images.[63, 111, 112] A PhotoFluor II light source (89 North, Burlington, VT) was focused onto the field of view (FOV, 34 mm × 45 mm) through a liquid light guide and used unfiltered for white light illumination. For fluorescence excitation of the dual probe stain, the PhotoFluor II was filtered with a 545 nm ± 12.5 nm or 620 nm ± 30 nm bandpass excitation filter for Cy3B or AF647, respectively. The fluence rate for each channel was 12 mW/cm^2 and 15 mW/cm^2 for the Cy3B and AF647 excitation, respectively. Fluorescence was collected with a 605 nm ± 35 nm or a 700 nm ± 37.5 nm bandpass emission filter for Cy3B or AF647, respectively. All filters were obtained from Chroma Technology (Bellows Falls, VT). In addition to tumor and adipose tissue pairs, an aliquot of each dual probe staining solution in a covered optical well plate (Greiner Bio-One, Monroe, NC) was imaged for normalization between channels and stain concentrations. Camera exposure times ranged from 10-50 ms and 150-500 ms for fluorescence image

collection of calibration drop images and tissue specimens, respectively. Image resolution for fluorescence and color images was 70 μm.

DDSI Image Processing

Co-registered images captured of targeted and untargeted fluorescence were processed and used to create DDSI images of each tumor-adipose tissue pair. Image processing was completed using custom-written MatLab Code (MathWorks, Natick, MA). Image processing began by subtracting the median background signal from the entire image in a user selected region of interest (ROI) in which no tissue was present. To account for any fluorescence variance between experiments, the staining solutions for each study were imaged and a user defined ROI was quantified for each probe pair and concentration used for staining. Images from each fluorescence channel were normalized by dividing each pixel by the average intensity value of the ROI representing the DDSI staining solution corresponding to the probe pair and concentration used for staining. A mask was then applied to each normalized image so that only pixels of measurable fluorescence (0.8-1.2x the average pixel value of the area containing tissue) were used in the DDSI image calculation. The DDSI image was then calculated as $I_{DDSI} = (I_{Targeted} - I_{Untargeted}) / I_{Untargeted.}$ Tumor and normal tissue areas were determined via user selected ROIs encompassing the entire tissue area and intersected with the tissue mask for statistical analysis.

Confocal Microscopy

Following macroscopic imaging, representative tumor and adipose tissue pairs were imaged immediately using the Zeiss LSM880 (Carl Zeiss Microscopy GmbH, Jena, Germany) to collect high resolution images of the targeted and untargeted probe fluorescence. Using a plan-apochromatic 20x (NA = 0.8) objective, images were collected with the following settings: laser: 561 nm, 10% transmission (DPSS 561-10, Cy3B); 633 nm, 2% transmission (HeNe633, AF647); beam splitter: MBS 458/514/561/633; filter: 566-628 nm (Cy3B), 638-755 nm (AF647); pixel time: 1.5 μs; average: line 1; master gain: 750 (Cy3B), 700 (AF647); pinhole size: 90 μm; and acquisition area 512 × 512 pixels, 16-bit. Zen imaging software (Zeiss) was used to merge each fluorescence channel image colorimetrically with the red channel representing Cy3B fluorescence and the green channel representing AF647 fluorescence.

IHC Staining & Microscopy

Following imaging, each tumor and adipose tissue pair was flash frozen in optimal cutting temperature (OCT) compound for tissue preservation. To enable IHC staining of each tissue pair, the OCT blocks were thawed and re-embedded in paraffin for sectioning, H&E staining, and HER2 IHC staining. The tissue face imaged for DDSI analysis was placed in the paraffin blocks so that it would be sectioned for staining. All blocks were faced prior to collecting serial sections for H&E and IHC staining, thus the exact tissue face that was imaged for DDSI analysis was not used for IHC staining. However, tissue within a few hundred microns was used for IHC analysis of HER2 expression levels. A different HER2 antibody (1:400, EP1045Y, ab134182, AbCam, Cambridge, MA) targeted to the intracellular domain of HER2 was used for IHC, to ensure staining of all HER2 proteins, even those already stained with Herceptin.[113] After paraffin embedding, H&E, and IHC staining was performed by Oregon Health and Science University's (OHSU) Histology Shared Resources. H&E and IHC slides were imaged using the Zeiss AxioScan.Z1 Microscope (Zeiss). Bright field images were obtained at 10x magnification. Using the ZEN Slide scanner software, the ROI (tumor and mammary adipose) was detected using Automatic Tissue Recognition due to the visibility of the H&E and IHC stains. Six field of views (FOVs) were used to set the focus map. The ROI was then scanned at 10x magnification, acquiring tiles over the entire tissue specimen, which were automatically stitched by the ZEN software to create the final image.

Statistical Analysis

Statistical analysis was performed using MatLab. To determine the tumor-to-normal adipose tissue diagnostic detection ability, ROC curves were generated for the untargeted probe images, targeted probe images, and calculated DDSI images. ROC curves and corresponding AUC measurements were calculated using the perfcurve function in MatLab on a pixel-by-pixel basis with individual pixel values for each tissue type used as the response variable input. Additionally, the optimal tumor vs. normal adipose tissue threshold values were determined using the ROC point generated from the perfcurve function and back calculated to actual pixel value thresholds. Histogram plots of the untargeted probe image, targeted probe image and DDSI image pixel values for tumor and normal adipose pixels were generated and the optimal threshold point determined via ROC curve analysis was plotted. Statistical significance between staining conditions was determined using the

method described by Hanley and McNeil[114] with standard error measurements and correlation coefficients for pixel intensity values in each channel used for z-score value calculations. z-score values >2 were considered statistically significant.[114] Sensitivity and specificity measurements were determined for the testing dataset using the optimal threshold value determined from the chosen final DDSI staining condition in the training parameter testing studies.

RESULTS

DDSI Staining Condition Testing and Qualitative Assessment of HER2 Expression by IHC

Varied DDSI probe pairs (Herceptin-Cy3B + DkRb-AF647, Herceptin-AF647 + DkRb-Cy3B), stain solution concentrations (100 and 200 nM), and staining incubation times (1 and 10 min) were examined to establish a DDSI staining protocol with speed and accuracy permitting both diagnostic performance and clinical feasibility (**Fig. 2.1B**). Qualitatively, DDSI images showed improved tumor-to-adipose tissue contrast when compared to untargeted or targeted probe images across all conditions and probe pairs tested (**Fig. 2.2**). Upon comparison, both probe pairs demonstrated the ability to differentiate between tumor and adipose tissues, showing that neither fluorophore label was dominating the tissue biodistribution kinetics of the targeted and untargeted probes.[108, 115] DDSI images also showed more homogeneous intensities across staining conditions and replicates compared to targeted or untargeted single probe images (**Fig. 2.2**). IHC assessment of HER2 staining patterns revealed similar HER2 expression with DDSI staining patterns across probe pairs and staining conditions (**Fig. 2.3**). By comparison, HER2 IHC staining patterns were not well aligned with single probe targeted staining patterns, often showing inverse staining patterns. Targeted and untargeted probes routinely showed similar staining pattern to one another, suggesting non-specific uptake dominated the staining pattern. DDSI corrected for the non-specific uptake, yielding staining patterns that were well matched with the ground truth HER2 IHC staining patterns (**Fig. 2.3**).

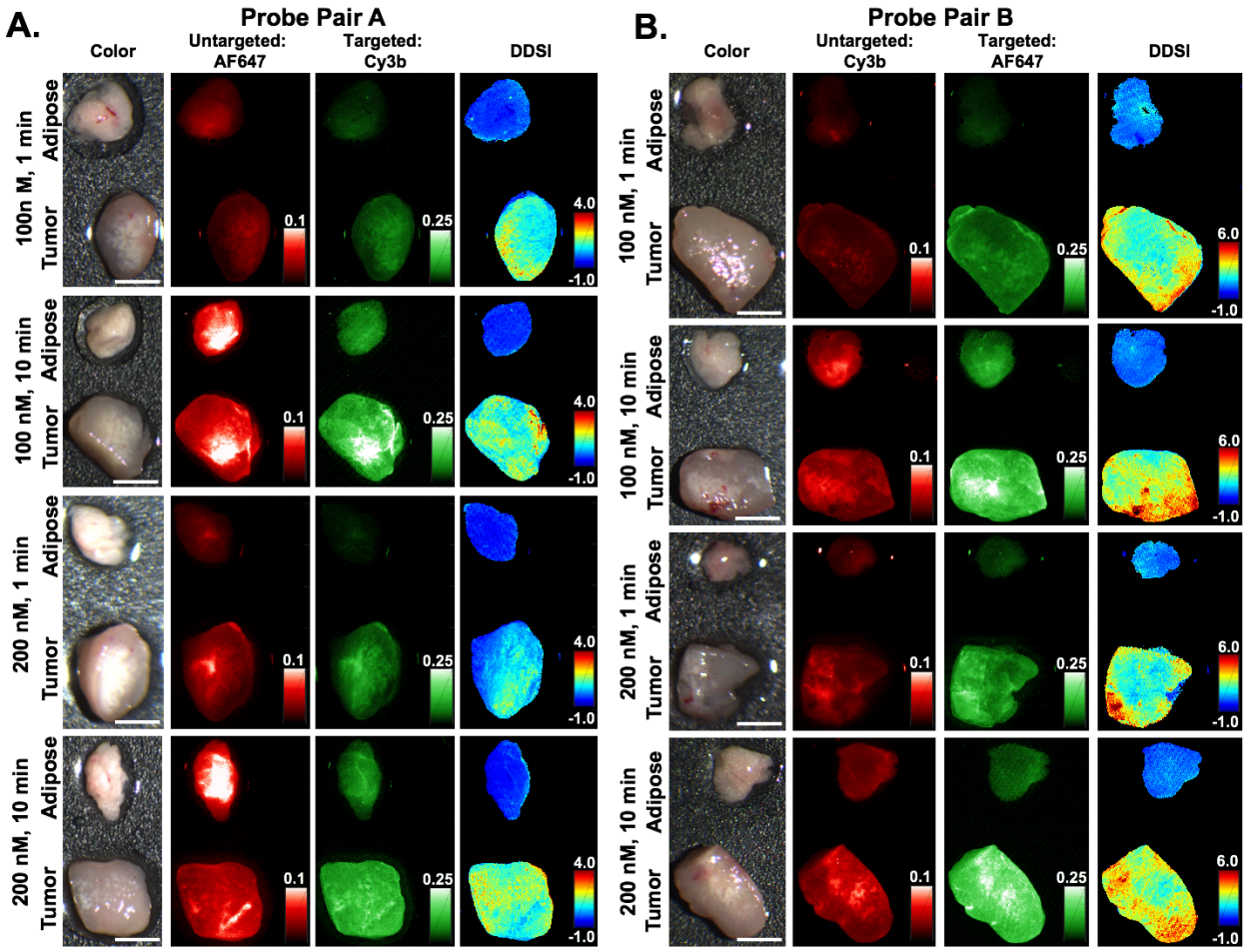

Fig. 2.2: *DDSI staining condition testing*. Representative color, fluorescence, and DDSI images of tumor and adipose tissue pairs following staining using a range of dual-stain soak concentrations and incubation times for **(A)** probe pair A (Herceptin-Cy3b, DkRb-AF647) and **(B)** probe pair B (Herceptin-AF647, DkRb-Cy3b). All images are representative of data collected for n=6 tumor and adipose tissue pairs per staining condition. All untargeted and targeted channel images are background corrected, normalized by their exposure time and calibration drop intensity, and displayed on equivalent color scales across staining conditions and probe pairs. DDSI images are displayed with equivalent color scales across staining conditions. Scale bars = 5 mm.

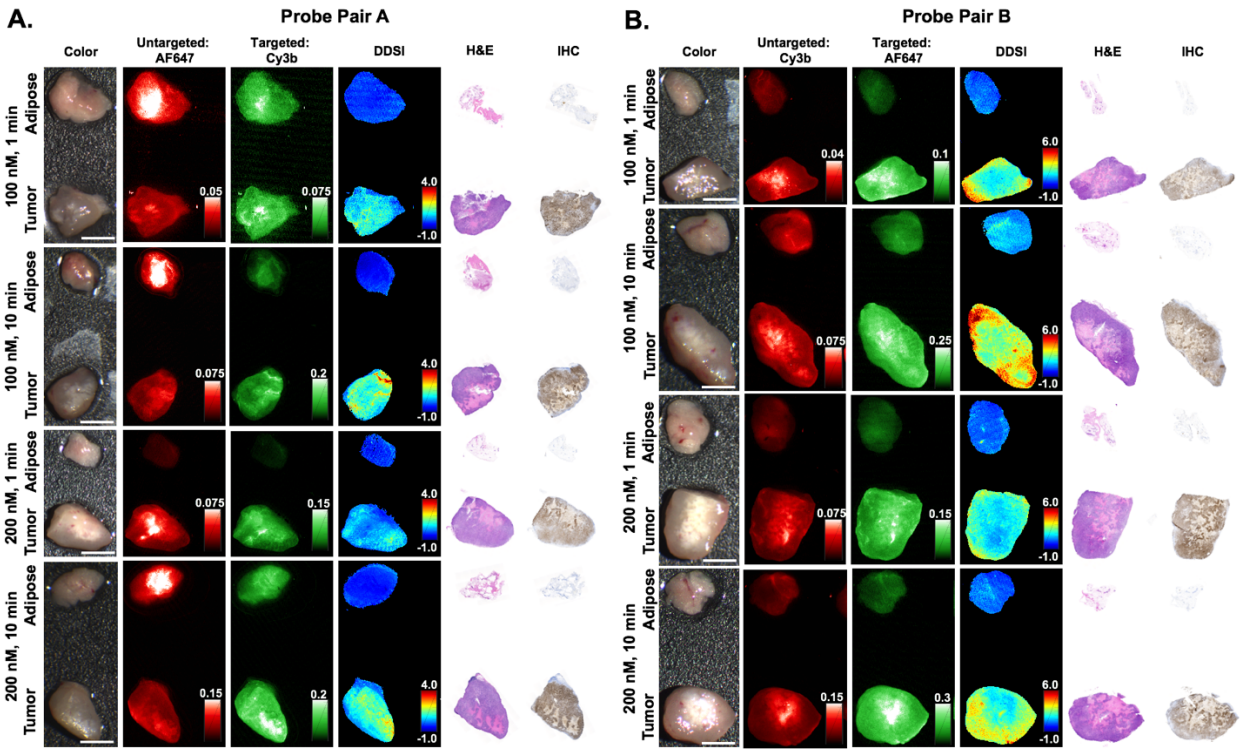

Fig. 2.3: *Immunohistochemical analysis and DDSI staining pattern validation.* Representative color, fluorescence, DDSI, H&E, and HER2 targeted IHC images of tumor and adipose tissue pairs following staining using a range of dual-stain soak concentrations and incubation times for **(A)** probe pair A (Herceptin-Cy3b, DkRb-AF647) and **(B)** probe pair B (Herceptin-AF647, DkRb-Cy3b). All images are representative of data collected for n=6 tumor and adipose tissue pairs per staining condition. All untargeted and targeted channel images are background corrected, normalized by their exposure time and calibration drop intensity. DDSI images are displayed with equivalent color scales across staining conditions. H&E and IHC images were acquired from serial sections of the same tissue face imaged in the whole specimen DDSI images. H&E: hematoxylin and eosin; IHC: immunohistochemistry. Scale bars = 5 mm.

Diagnostic Potential Quantification and Final Staining Parameter Selection using Training Tumor Xenograft Cohort

Untargeted, targeted, and DDSI image data was quantified using ROC curve analysis to determine the most clinically relevant probe pair and staining conditions. AUC for each ROC curve was calculated to assess the ability to differentiate tumor from adipose tissue for each tested staining condition (**Fig. 2.4A & 2.4B**). DDSI significantly improved tumor vs. normal adipose tissue AUC values when compared to targeted single probe staining alone across all DDSI probe pairs and tested staining conditions (**Fig. 2.4, Table 2.1**). These results are in agreement with a similar and promising analysis performed in human breast cancer specimens using

dual probe ratiometric imaging of SERS nanoparticles to guide tumor margin assessment.[116] The highest three AUC values were generated using the 200 nM, 10 min staining condition for the Herceptin-AF647 + DkRb-Cy3B probe pair (AUC = 0.989), 100 nM, 10 min staining condition for the Herceptin-Cy3B + DkRb-AF647 probe pair (AUC = 0.978), and 200 nM, 1 min staining condition for the Herceptin-AF647 + DkRb-Cy3B probe pair (AUC = 0.974) (**Fig. 2.4A, 4B**).

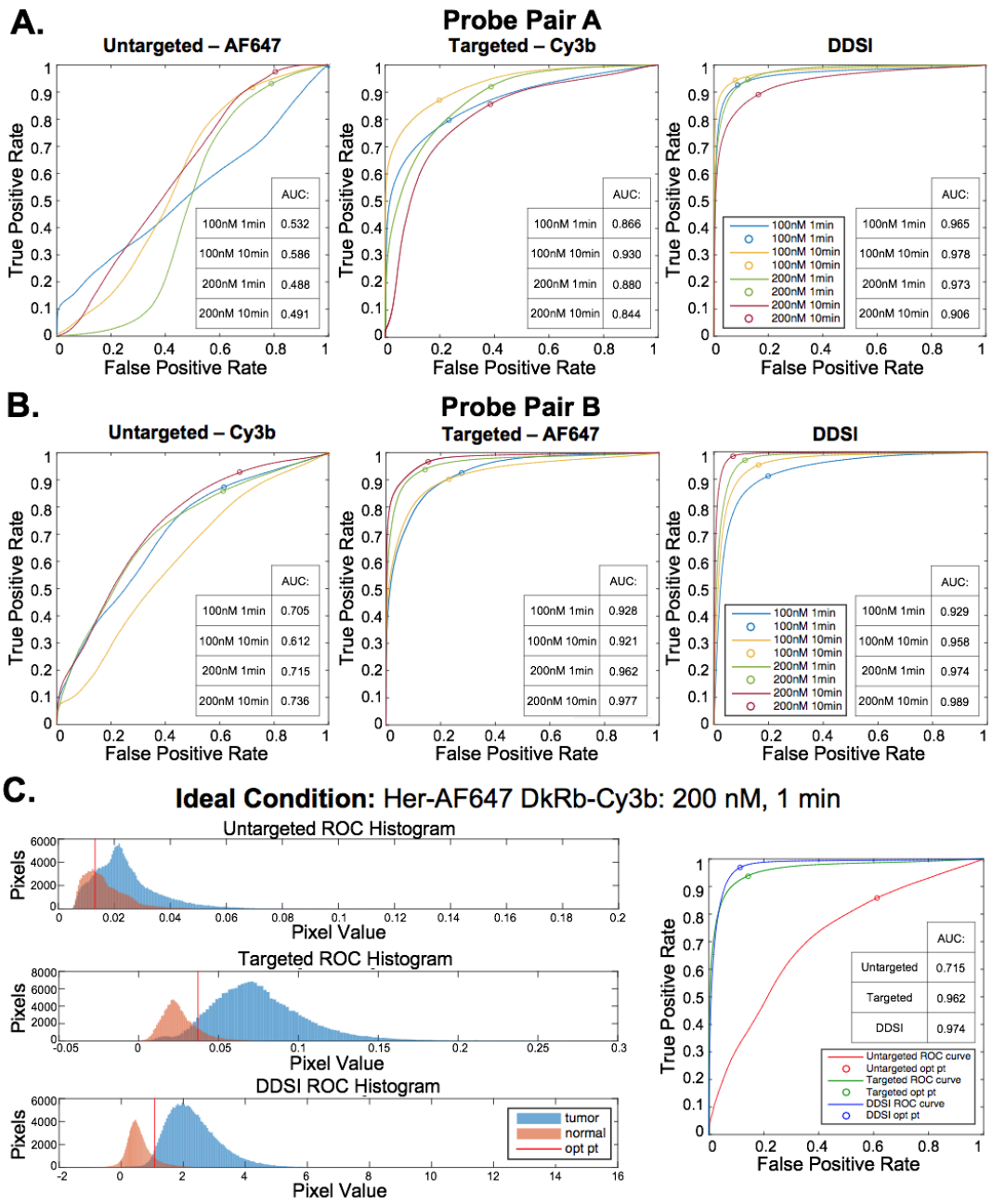

Fig. 2.4: *ROC curve analysis and final DDSI staining condition selection*. ROC curves and AUC values for untargeted, targeted, and DDSI images of tumor vs. normal adipose tissue differentiation following staining using a range of dual-stain soak concentrations and incubation times for **(A)** probe pair A (Herceptin-Cy3b, DkRb-AF647) and **(B)** probe pair B (Herceptin-AF647, DkRb-Cy3b). **(C)** Tumor and normal tissue pixel intensity histograms, ROC curves, and AUC values for untargeted, targeted, and DDSI images following staining using probe pair B at 200 nM concentration and 1 min incubation time. Optimal points determined from ROC curve analysis are displayed on each ROC curve and as a vertical line on each pixel value histogram. ROC: receiver operator characteristic; AUC: area under curve; opt pt: optimal point.

The 200 nM, 1 min staining condition using the Herceptin-AF647 + DkRb-Cy3B probe pair was chosen as the most clinically viable staining condition since its AUC was not appreciably different than the 10 min staining conditions and the 1 min incubation time would be more clinically feasible for margin assessment in the operating room. Histograms of the untargeted, targeted, and DDSI pixel values demonstrated the improved separation of intensity distribution between MCF7-HER2 tumor and normal adipose tissue using the DDSI method compared to the targeted or untargeted probe alone (**Fig. 2.4C**). Additionally, a more normal distribution for both tissue types was obtained using DDSI compared to the single probe targeted stain, signifying the improvement in ROC AUC values (**Fig. 2.4C**) and intensity normalization between replicates as a result of DDSI. Additionally, the optimal cutoff values determined using ROC curve analysis were plotted on the untargeted, targeted, and DDSI histograms to demonstrate the ability to perform automated differentiation between tumor and adipose tissue using a single threshold.

Table 2.1: *ROC AUC values and z-statistics for DDSI stain condition testing.*

Probe Pair A Targeted: Herceptin-Cy3B, Untargeted: Dk-anti-Rb-AF647							**Probe Pair B** Targeted: Herceptin-AF647, Untargeted: Dk-anti-Rb-Cy3B						
Stain Concentration:	**Incubation Time:**						**Stain Concentration:**	**Incubation Time:**					
	1 min			**10 min**				**1 min**			**10 min**		
100 nM	UT	T	DDSI	UT	T	DDSI	**100 nM**	UT	T	DDSI	UT	T	DDSI
	0.532	0.866	0.965	0.586	0.930	0.978		0.705	0.928	0.929	0.612	0.921	0.958
	z-stat:	155.7		z-stat:	114.6			z-stat:	3.1		z-stat:	72.1	
200 nM	UT	T	DDSI	UT	T	DDSI	**200 nM**	UT	T	DDSI	UT	T	DDSI
	0.488	0.880	0.973	0.491	0.844	0.906		0.715	0.962	0.974	0.736	0.977	0.989
	z-stat:	172.2		z-stat:	163.0			z-stat:	29.8		z-stat:	48.2	

*UT: untargeted channel; T: targeted channel; ROC: receiver operator characteristic; AUC: area under curve; z-stat: z-statistic obtained from comparison of targeted vs. DDSI ROC AUC values for each staining condition (z-stat > 2 signifies significantly different AUC values).

Final DDSI Method Validation in MCF7-HER2 and MCF7 Testing Tumor Xenograft Cohort

The selected probe pair (Herceptin-AF647 + Dk-Rb-Cy3B) and staining condition (200 nM, 1 min) was applied to a testing MCF7-HER2 (HER2+) paired tumor and normal adipose tissue cohort and to a matched MCF7 (HER2-) tumor and normal adipose tissue cohort for validation of the diagnostic potential of the final DDSI staining condition (**Fig. 2.5**). MCF7-HER2 tumors stained using the chosen probe pair and staining conditions demonstrated similar improvements in DDSI tumor vs. normal adipose AUC values when compared to the single probe targeted

stain (Targeted AUC = 0.84, DDSI AUC = 0.95, z = 131.0). Additionally, similar optimal cutoff values to the staining condition testing training MCF7-HER2 tumor cohort were determined for the testing cohort upon ROC curve analysis (**Fig. 2.5C**). Applying the optimal threshold value determined from the training cohort (**Fig. 2.4C**) to the testing cohort (**Fig. 2.5C**) provided a sensitivity of 91% and a specificity of 84% for tumor vs. normal tissue differentiation. The MCF7 tumor cohort stained using the selected probe pair and staining conditions demonstrated significantly lower DDSI image intensities and DDSI tumor vs. normal adipose tissue AUC values compared to the MCF7-HER2 tumor cohort. Additionally, the tumor vs. normal adipose tissue AUC value was decreased from 0.67 for the single probe targeted stain to 0.50 for DDSI in the MCF7 tumor line tumor. This was the expected behavior as MCF7 is a HER2 negative cell line that should not generate HER2 specific signal; however, when targeted probe alone was assessed, some nonspecific uptake of HER2 was seen (AUC = 0.67), which was corrected using the DDSI protocol (AUC = 0.50). HER2 targeted IHC completed on the same representative tissue confirmed the expected HER2 overexpression in MCF7-HER2 tumors, which was again closely matched with the DDSI pattern. Furthermore, high resolution images of the targeted probe and IHC staining pattern confirmed the membrane bound fluorescence staining pattern expected from HER2 targeted imaging (**Fig. 2.6**). HER2 IHC staining showed minimal HER2 expression in MCF7 parent line tumors, supporting the DDSI AUC of 0.50 between tumor and normal tissues based on HER2 expression (**Fig. 2.5**).

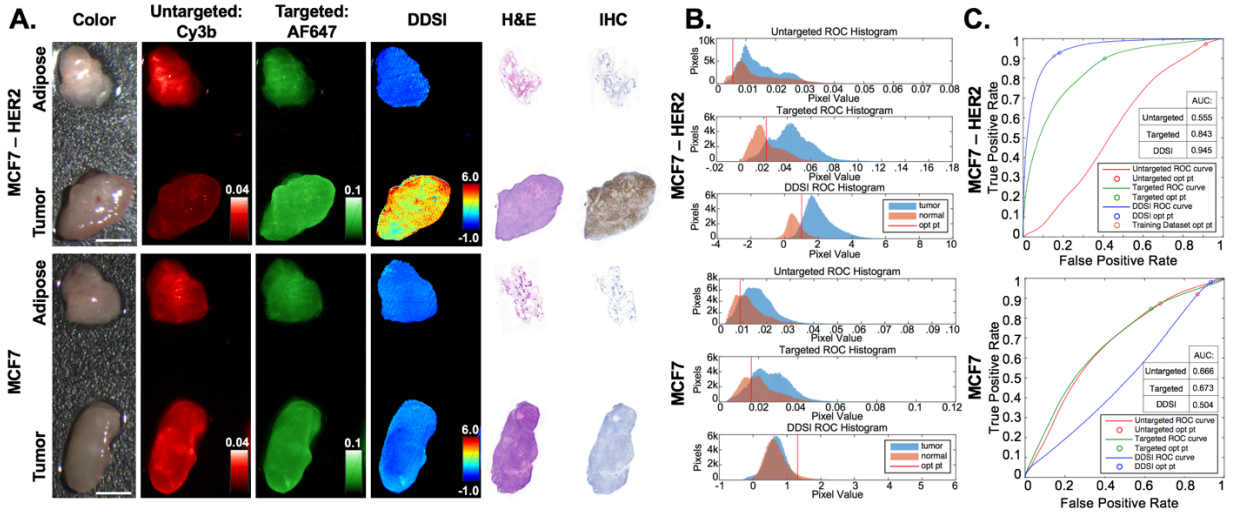

Fig 2.5: *HER2(+) and HER2(-) testing cohort for DDSI staining and IHC validation.* **(A)** Representative color, fluorescence, DDSI, H&E, and HER2 targeted IHC images of MCF7-HER2 (HER2+) and MCF7 (HER2-) tumor and adipose tissue pairs following staining using the final staining condition (Probe pair B, 200 nM concentration, 1 min incubation time). All images are representative of data collected for n=6 tumor and adipose tissue pairs per tumor cell line. All untargeted and targeted channel images are background corrected, normalized by their exposure time and calibration drop intensity, and displayed on equivalent color scales. DDSI images are displayed with equivalent color scales. H&E and IHC images were acquired from serial sections of the same tissue face imaged in the whole DDSI specimen images. Scale bars = 5 mm. **(B)** Tumor and normal tissue pixel intensity histograms, **(C)** ROC curves, and AUC values for untargeted, targeted, and DDSI images corresponding to each cell line. Optimal points determined from ROC analysis are displayed on each ROC curve (blue marker) and as a vertical line on each pixel value histogram. The optimal point determined from the training cohort data is displayed on the MCF7-HER2 tumor specimen ROC curve to demonstrate the diagnostic reproducibility under final staining conditions (orange marker). H&E: Hematoxylin & Eosin; IHC: immunohistochemistry; ROC: receiver operator characteristic; AUC: area under curve; opt pt: optimal point.

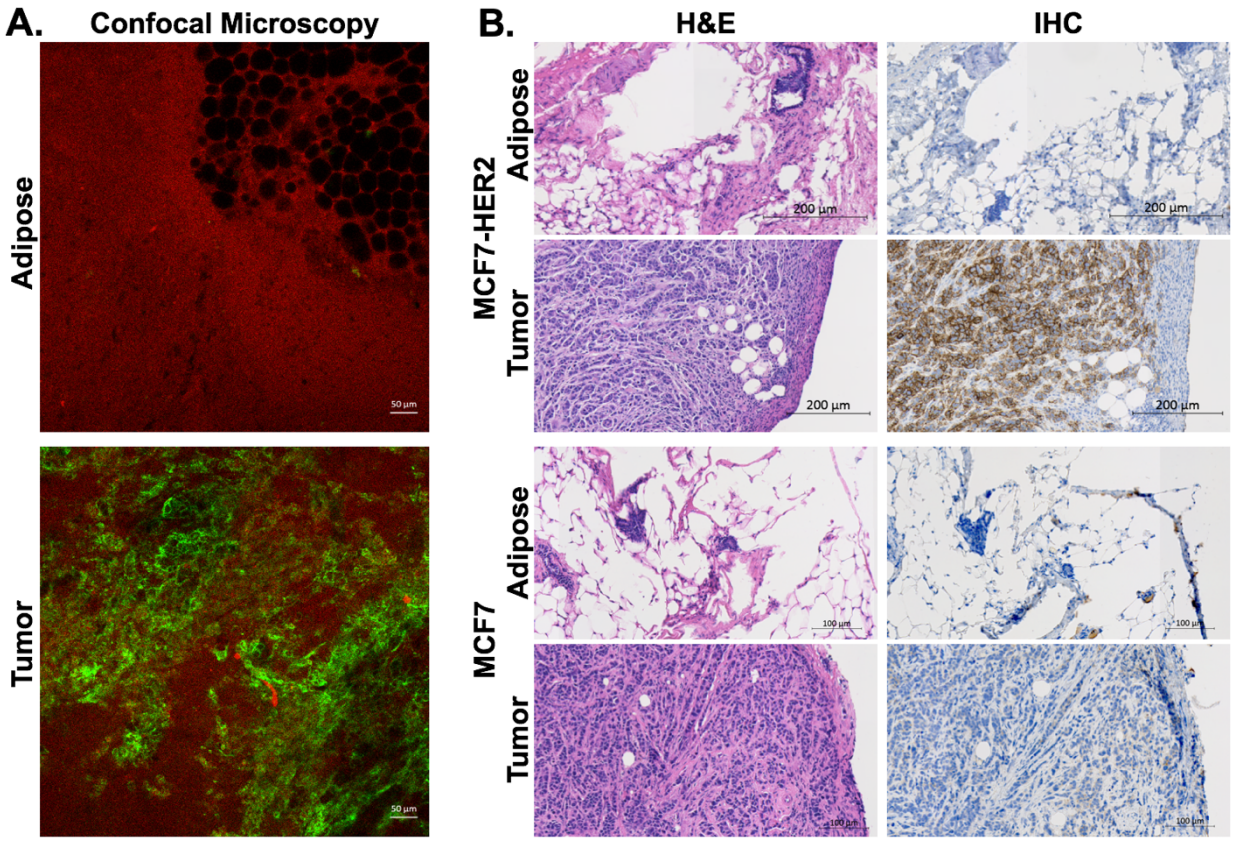

Fig. 2.6: *High resolution confocal microscopy and HER2 immunohistochemical analysis.* **(A)** Representative high-resolution fluorescence confocal images of fresh MCF7-HER2 tumor and adipose tissue specimens imaged following completion of the final DDSI staining methodology (Probe pair B, 200 nM concentration, 1 min incubation time). Images were taken from the same cut face used for macroscopic images. Red channel = Cy3b fluorescence, Green channel = AF647 fluorescence. **(B)** Representative high-resolution H&E and HER2 targeted IHC images of of MCF7 – HER2 and MCF7 parent line tumor and adipose tissue pairs following staining using the final staining condition (Probe pair B, 200 nM concentration, 1 min incubation time). H&E and IHC images are acquired from serial cryosections of the same face imaged in the whole specimen images. H&E = Hematoxylin & Eosin, IHC = immunohistochemistry.

DISCUSSION

The primary aims of this study were to optimize and validate the DDSI staining technique for improved tumor margin assessment during BCS. Incomplete tumor resection during BCS plagues surgical outcomes, requiring expensive, invasive follow-up surgery, increasing the chances of morbidity, and negatively affecting patient outcomes.[12, 48-51] Contrast guided resection techniques have shown

promise for improved margin assessment using molecularly specific probes;[33, 34] however clinical translation of contrast agents for *in vivo* applications remains challenging. To circumvent these difficulties, staining of the resected tumor specimens has gained in popularity. However non-specific contrast uptake dominates resected specimen staining, significantly decreasing tumor to normal tissue contrast. Using the novel DDSI technique developed herein, non-specific uptake can be overcome and excised tumor tissue can be distinguished from normal tissue with high sensitivity and specificity.[52]

In the present study, we examined a wide range of staining conditions where probe concentration, staining time and fluorophore were varied from conditions used in the prior proof-of-concept study to identify a suitable protocol for future clinical studies (**Fig. 2.1**). We evaluated the diagnostic performance of a single condition, which could both minimize staining time and optimize diagnostic potential. The diagnostic potential was evaluated using a semi-blinded, pre-clinical study through ROC curve analysis on a training data set to define an optimal diagnostic threshold and applied prospectively to a testing data set that included normal tissue, HER2(+) tumors and HER2(-) tumors.

The DDSI staining conditions tested provided a robust and rapid diagnostic technique for intraoperative tumor margin assessment. Across both fluorescent probe pairs and all staining conditions, DDSI showed improved tumor to normal adipose tissue differentiation as compared to targeted probe alone (**Fig. 2.2, Fig. 2.4A & 2.4B**). The fluorophore labels chosen for this study, AF647 and Cy3B, did not significantly affect DDSI performance, with consistent tumor to normal adipose tissue differentiation across both fluorophore antibody probe pairs. While probe pair B demonstrated an increase in DDSI values compared to probe pair A, this increase occurred in both tumor and normal tissue equally, causing negligible overall change in probe pair B's diagnostic ability over probe pair A (**Fig. 2.2, Fig. 2.4A & 2.4B**). Additionally, the DDSI protocol normalized tumor HER2 intensities between staining conditions, where intensities were significantly less affected by the varied staining parameters than single targeted probe intensities. The selected final staining condition provided high tumor vs. normal tissue sensitivity (97%) and specificity (89%) determined via retrospective ROC curve analysis with a 1 min incubation in a 200 nM solution of the Herceptin-AF647 + DkRb-Cy3B probe pair (**Fig. 2.4C**) decreasing overall staining time and imaging time to a total of 16 min, while improving ability to differentiate between benign and malignant tissues.

Importantly, DDSI staining does not interfere with downstream pathology, enabling utilization of current gold standard diagnostic methods to validate intraoperative observations for first in human clinical trials. As a demonstration, DDSI staining patterns were correlated to HER2 expression using HER2 targeted IHC (**Fig. 2.3**). DDSI staining patterns were found to closely align with HER2 expression levels and patterns across staining conditions. By comparison, single probe targeted staining patterns were not well aligned with IHC staining patterns, with higher targeted fluorescence intensities in regions of low HER2 IHC expression (**Fig. 2.3**). These results demonstrate that the DDSI method accommodates non-specific uptake of the targeted probe as well as other imaging anomalies inherent to single probe optical imaging such as variations in imaging system illumination power, detector non-uniformities, detector working distance, etc. Thus, DDSI provided the ability to rapidly visualize biomarker-bound fluorescence, enabling specific molecularly-targeted imaging to be completed on resected tissues.

The performance of the selected DDSI protocol was confirmed in an independent testing tumor cohort consisting of HER2+ (MCF7-HER2) and HER2- (MCF7) tumor specimens. The HER2+ testing dataset showed similar diagnostic AUC and optimal cutoff values to the prior HER2+ training dataset, demonstrating the repeatability and robustness of the DDSI staining and analysis method. Applying the optimal threshold calculated from training dataset values, high tumor vs. normal tissue sensitivity (91%) and specificity (84%) was achieved. As expected, the HER2- testing dataset showed lower DDSI signal intensities and AUC values compared to the HER2+ tumor line (**Fig. 2.5**). Notably, for HER2- tumor specimens, both targeted and untargeted AUC values were above 0.50, signifying higher uptake in the tumor tissue compared to the normal adipose tissue even though the tissue lacked the HER2 biomarker. DDSI was able to correct for this nonspecific uptake of the targeted stain by the HER2- tumor tissue, bringing the AUC value back down to the expected value of 0.50. These results validate the ability to provide specific molecular imaging on resected tissues with the DDSI technique.

Continued stain protocol development will be necessary to further reduce the overall staining time generating a clinically relevant staining protocol. Total resected specimen staining time could be additionally reduced by optimizing the washing and blocking conditions, which can likely be reduced to <10 min for rapid margin assessment in the operating room. Expanding and screening this technique with a panel of tumor specific biomarkers such as epidermal growth factor receptor

(EGFR), estrogen receptor (ER), and progesterone receptor (PgR) for breast cancer, is also needed to utilize DDSI tumor margin assessment on patient specimens with varied tumor subtype, heterogeneous cellular phenotypes and expression patterns, where multiplexed biomarker imaging could be achieved through the addition of other targeted fluorescence channels.[117, 118] This will facilitate translation of the DDSI technique to human specimens excised during BCS for complete validation of this promising technique for margin detection during BCS. Although studies testing mixed tumor and adipose samples are not feasible using xenograft models, DDSI staining on resected human breast tissue samples composed of varying percentages of tumor and adipose mixed tissues will be imperative for validation of the clinical diagnostic performance of the DDSI method.

The animal model system used for this study provided a controlled platform that allowed examination of several different processing conditions and probe pairs; however, as with any translational animal study, the model system has its limitations in recapitulating the challenges in diagnosing human tissue. The small normal tissue volumes and lack of infiltrative tumor growth patterns are relevant limitations of mouse models for this application. However, the dual-probe technique is designed to accommodate/remove the effects of diffusion and other non-specific kinetic behavior regardless of tissue type and structure, and our results suggest that the DDSI parameter is indeed reporting receptor-specific information. These results also provide a robust, evidenced-based protocol for translation to humans. The next phase of development involves validating the final stain protocol developed herein on thick slices of discarded human breast specimens from tumor mastectomy patients and then initiating an observational clinical study in the operating room.

In summary, the selected DDSI staining technique showed significant improvement in distinguishing tumor from normal adipose tissue in excised specimens over targeted staining alone. Perturbations in antibody-fluorophore probe pairs had little effect on DDSI performance with consistent tumor vs. normal tissue diagnostic performance across all tested staining conditions. Using antibody-based probes and visible fluorophores, the probe penetration and imaging depth are inherently surface weighted and likely limited to a few microns at best. However, according to new consensus criteria for breast cancer margin status, margins are considered to be negative for tumor when there is no tumor at the “ink” or surface of the resected specimen, making the current probe composition viable for clinical translation.[119] DDSI was also demonstrated to be an accurate reporter of tumor

specific molecular expression levels of HER2, and provided a validated diagnostic method for intraoperative tumor margin detection with high sensitivity and specificity for BCS. The DDSI framework is generalizable to surgical resection of other cancers, and we are actively studying its application for other indications. With further development and application to a range of cancer biomarkers, this technique could provide the ability to identify diverse cancer phenotypes for improved tumor margin assessment intraoperatively, reducing re-excision rates and improving patient outcomes.

Chapter 3

Direct administration of nerve-specific contrast to improve nerve sparing radical prostatectomy

This manuscript was originally published in *Theranostics*. Barth, C.W. & Gibbs, S.L. Direct Administration of Nerve-Specific Contrast to Improve Nerve Sparing Radical Prostatectomy. *Theranostics* 7, 573-593 (2017).

ABSTRACT

Nerve damage remains a major morbidity following nerve sparing radical prostatectomy, significantly affecting quality of life post-surgery. Nerve-specific fluorescence guided surgery offers a potential solution by enhancing nerve visualization intraoperatively. However, the prostate is highly innervated and only specific nerve structures, namely the cavernosal nerves within the neurovascular bundle, require preservation to maintain continence and potency. Systemic administration of a nerve-specific fluorophore would lower nerve signal to background ratio (SBR) in vital nerve structures, making them difficult to distinguish from all nervous tissue in the pelvic region. A direct administration methodology to enable selective nerve highlighting for enhanced nerve SBR in a specific nerve structure has been developed herein. The direct administration methodology demonstrated equivalent nerve-specific contrast to systemic administration at optimal exposure times. However, the direct administration methodology provided a brighter fluorescent nerve signal, facilitating nerve-specific fluorescence imaging at video rate, which was not possible following systemic administration. Additionally, the direct administration methodology required a significantly lower fluorophore dose than systemic administration, that when scaled to a human dose falls within the microdosing range. Furthermore, a dual fluorophore tissue staining method was developed that alleviates fluorescence background signal from adipose tissue accumulation using a spectrally distinct adipose tissue specific fluorophore. These results validate the use of the direct administration methodology for specific nerve visualization with fluorescence image-guided surgery, which would improve vital nerve structure identification and visualization during nerve sparing radical prostatectomy.

INTRODUCTION

Prostate cancer is the most prevalent cancer in men and the second leading cause of male cancer death in the United States.[120] The main treatment options are active surveillance, radiotherapy, and radical prostatectomy.[121] Radical prostatectomy is the most effective prostate cancer therapy, significantly reducing prostate cancer mortality as compared to active surveillance[122] or radiotherapy.[123-125] While the ultimate goal of radical prostatectomy is cancer cure, preserving the nerve structures responsible for continence and potency is vital to quality of life. To enhance nerve preservation, the nerve sparing method was developed over 30 years ago.[126] However, nerve damage continues to plague radical prostatectomy and is reported in up to 60% of patients one-year post surgery.[6, 127] Furthermore, the outcome of the nerve sparing procedure is highly reliant on the surgeon's experience and ability to master the technique.[14, 128] These shortcomings are largely due to the inability to directly visualize the vital nerve structures intraoperatively. Surprisingly, no clinically approved method exists to enhance direct nerve visualization in the surgical suite. Current nerve detection is completed through visual inspection, which is hampered by the small size of the vital nerves as well as the depth and narrowness of the pelvis making distinguishing nerves from surrounding tissues challenging.[54, 129]

Fluorescence image-guided surgery offers the potential for improved visualization of specifically highlighted tissues, such as nerves, intraoperatively in real time. Using optical imaging technologies, fluorescence image-guided surgery can provide real time imaging with specific labeling in minimally invasive systems that are readily implemented into current surgical workflows.[15, 17, 20, 130, 131] Other technologies, such as confocal endomicroscopy and optical coherence tomography, have demonstrated visualization of the nerves surrounding the prostate intraoperatively with high resolution, however these lack widefield imaging functionality, diminishing the ability to identify nerve tissues in real time.[55-58] In addition, these imaging probe-based technologies often require that the probe be in direct contact with the nerve tissue, generating point based measurements instead of images and potentially interfering with minimally invasive procedure workflows.

Non-imaging technologies such as optical nerve stimulation have also been used to identify nerves by measuring intracavernous pressure upon stimulation of nerve tissue, however without direct imaging capability and a lag time of 2-5 s between stimulation and measurement, real time nerve identification is again difficult to achieve.[132-135] The utility of fluorescence image-guided surgery has been demonstrated using developed imaging systems, such as the FLARE[15-20], Fluobeam 800[21], Photodynamic eye[22], HyperEye Medical System[23], and the FDA approved fluorescence-imaging channel in the da Vinci surgical robot (Intuitive Surgical, Inc., Sunnyvale, CA). However, to date, only two FDA approved near infrared (NIR) fluorescent contrast agents exist, including methylene blue and indocyanine green, both blood pool agents that do not provide nerve-specific contrast. Fluorescence imaging in the NIR region (650-900 nm) is advantageous as endogenous tissue chromophore absorbance, scattering and autofluorescence are all at local minima, creating a black background upon which tissue-specific contrast can be added.[25] Fluorophores positioned in the NIR window can be visualized with minimal background at up to centimeter depths in tissue, compared to micron to millimeter depths in the visible region, due to increased photon penetration.[24, 131] Several classes of small molecule fluorophores have been shown to stain nerve and/or brain tissue in preclinical *in vivo* studies, including stilbene derivatives,[64] a coumarin analog,[65] distyrylbenzene derivatives,[20, 66-70] styryl pyridinium fluorophores,[71, 72] a tricarbocyanine fluorophore,[73] and an oxazine fluorophore.[74] These fluorophores have been shown to readily penetrate the blood-nerve barrier (BNB) and/or blood-brain barrier (BBB) following systemic administration providing nerve- and/or myelin-specific contrast. However, only three classes of these fluorophores have demonstrated red to near infrared (NIR) excitation and/or emission wavelengths, where the oxazine fluorophore, Oxazine 4, has demonstrated both strong nerve specificity following systemic administration as well as red-shifted excitation and emission wavelengths.[74]

Although systemic administration of Oxazine 4 highlights all nerve tissue,[74] utility for radical nerve sparing prostatectomy may be limited. The prostate is a highly innervated organ where the nerves responsible for continence and potency branch from the pelvic plexus and lie within fibrofatty tissue along the lateral surfaces of the prostate.[136, 137] During nerve sparing prostatectomy, preservation of all nerve tissue is not possible. Fortunately, only preservation of the cavernous nerves, which are thought to lie within the neurovascular bundle (NVB), are required

for recovery of urinary continence and erectile function post-surgery.[61, 62] Therefore, systemic administration of Oxazine 4 would potentially diminish the signal-to-background ratio (SBR) of the cavernous nerves due to extensive nerve fluorescence throughout the prostate. A direct/direct administration methodology where the fluorophore is applied to the nerve tissue of interest to highlight the desired nerve structure has the potential to alleviate these difficulties by selectively labeling the vital nerve structures during nerve sparing radical prostatectomy. This selective labeling technique would be feasible during a nerve-sparing procedure where the prostatic pedicles containing the prostatic arteries and NVB are isolated following incision of the lateral prostatic fascia, allowing application of the nerve-specific fluorophore to an isolated region within the prostate containing the vital nerve structures.[138] In addition, by only highlighting relevant prostatic nerves rather than every nerve in the body via systemic administration, a direct administration methodology would inherently require a significantly lower dose of fluorophore, making clinical translation more feasible.

The goal of the current work was to develop a direct administration methodology that provided at least equivalent nerve contrast to systemic administration and could be completed within a clinically relevant time frame through testing of several unique parameters. Direct administration cannot create nerve-specific contrast using biodistribution and clearance afforded to an intravenously injected fluorophore. Therefore, significant non-specific tissue accumulation can occur following direct tissue application that must be removed to create nerve-specific contrast. Through optimization of the fluorophore dose, incubation time, and washing protocol, non-specific fluorescence background signal was minimized while maintaining nerve-specific fluorescence. Furthermore, to ensure nerve-specific staining could be completed in a clinically relevant time frame (15-20 minutes), the total length of the direct administration methodology was reduced to facilitate seamless integration into current surgical practice. Additionally challenging to development of a direct administration methodology, was the well documented non-specific accumulation of nerve-specific fluorophores in adipose tissue due to their inherent lipophilicity.[20, 66, 68, 69] Since the vital nerve structures in the prostate are embedded in a fibrofatty plate in the pelvic region,[137, 139] a dual fluorophore staining protocol using Oxazine 4 to highlight nerves and Nile Red to delineate adipose was also developed to mitigate non-specific adipose fluorescence, which would diminish nerve SBR. Nile Red is a fluorogenic, lipid-specific oxazine

fluorophore that is spectrally distinct from Oxazine 4,[140-144] facilitating separation of nerve and adipose tissue fluorescence using a two-color imaging strategy. Translation of the final direct administration methodology to radical nerve-sparing prostatectomy could significantly improve cavernous nerve visualization and preservation, decreasing patient morbidity and improving post-surgical quality of life for prostate cancer survivors.

MATERIALS AND METHODS

Study Design

This study was designed to optimize the direct administration of nerve-specific fluorophores for image-guided surgery as a clinically relevant alternative to systemic administration. Aspects of the fluorophore dose, incubation time, and removal of non-specific fluorophore accumulation were testing in murine nerve models *in vivo*, specifically utilizing the readily accessible brachial plexus and sciatic nerves. The performance of each dose, incubation time, and washing protocol variation was evaluated using a custom-built small animal imaging system to detect fluorescence signal to background ratio at the selected nerve site as well as color images of the surgical field of view. The final direct administration protocol developed in murine peripheral nerves was applied to rat autonomic nerves to demonstrate the utility of the staining procedure in a surgically accessible rodent model of the prostatic nerves.

For direct administration studies, only 2 nerve sites per mouse or rat were stained and imaged due to detectable non-specific accumulation of the fluorophores in other areas of the body following completion of the staining and imaging procedures on the initial nerve sites. Staining on 2 nerve sites per animal was performed concurrently on either the brachial plexus or sciatic nerve sites in mice or on the aortic plexus and hypogastric nerve sites in rats. Power analysis performed on preliminary data showed that n=3 nerve sites were needed for each group to obtain power of 0.9 and alpha of 0.01. Direct administration optimization studies were completed with 3 replicates (2 brachial plexuses and 1 sciatic nerve) per treatment group, while systemic administration, final direct administration, and rat autonomic nerve studies were completed with 4 replicates per treatment group (2

brachial plexuses and 2 sciatic mouse nerves or 2 aortic plexuses and 2 hypogastic rat nerves, respectively per treatment group).

Contrast Agents

Oxazine 4 perchlorate was obtained from Fisher Scientific Inc. (Pittsburgh, PA). Nile Red was obtained from Sigma-Aldrich (Saint Louis, MO). To solubilize both fluorophores a slightly modified version of the previously reported co-solvent formulation containing 10% dimethyl sulfoxide (DMSO), 5% Kolliphor EL, 65% serum, and 20% phosphate buffered saline (PBS) was used [20]. Oxazine 4 had peak absorbance in PBS, pH 7.4 at 616 nm and peak emission at 635 nm.[74] Nile Red had peak absorbance in model lipids representing the main molecular composition of adipose tissue at 530-550 nm and peak emission at 620-635 nm.[142] The absorbance and emission spectra of each fluorophore was determined using a SpectraMax M5 microplate reader (Molecular Devices, Sunnyvale, CA). Absorbance and emission spectra were collected in PBS, co-solvent formulation, and olive oil at 10 μM fluorophore concentration in each solvent. Olive oil was chosen as the solvent to mimic a lipid environment for accurate representation of Nile Red's absorption and emission *in vivo*, which is solvatochromic where emission maximum shifts based on the solvent polarity and degree of solubility.[142]

Animals

Approval for the use of all animals in this study was obtained from the Institutional Animal Care and Use Committee (IACUC) at Oregon Health and Science University (OHSU). Male CD-1 mice weighing 22-24g and Male Sprague Dawley rats weighing 276-300g were purchased from Charles River Laboratories (Wilmington, MA). Prior to surgery, animals were anaesthetized with 100 mg/kg ketamine and 10 mg/kg xylazine (Patterson Veterinary, Devens, MA). The brachial plexus, aortic plexus, hypogastric and sciatic nerves were surgically exposed by removal of overlaying adipose and muscle tissues for direct nerve staining and imaging.

Intraoperative Fluorescence Imaging System

A custom-built small animal imaging system capable of real-time color and fluorescence imaging was used to acquire rodent *in vivo* images. The imaging system consisted of a QImaging EXi Blue monochrome camera (Surrey, British Columbia,

CA) for fluorescence detection with a removable Bayer filter for collecting co-registered color and fluorescence images. A PhotoFluor II light source (89 North, Burlington, VT) was focused onto the surgical field through a liquid light guide and used unfiltered for white light illumination. For fluorescence excitation, the PhotoFluor II was filtered with a 545 ± 12.5 nm or a 620 ± 30 nm bandpass excitation filter for Nile Red or Oxazine 4, respectively. Resulting fluorescence was collected with a 605 ± 35 nm or a 700 ± 37.5 nm bandpass emission filter for Nile Red or Oxazine 4 image collection, respectively (**Fig. 3.1**). All filters were obtained from Chroma Technology (Bellows Falls, VT). Camera exposure times ranged from 2.5 – 300 ms for fluorescence image collection. All images collected for comparison between treatment groups were acquired with the same exposure time and are displayed under equal normalized brightness and contrast levels where indicated. For dual fluorophore tissue separation studies, Oxazine 4 and Nile Red fluorescence merged images were created in ImageJ[145] by subtracting the Oxazine 4 fluorescence image from the coregistered Nile Red fluorescence image after which the two fluorescence images were merged with the Oxazine 4 image false colored green and Nile Red image false colored red. For rat autonomic nerve and prostate staining studies, Oxazine 4 fluorescence and color merged images were created in ImageJ [145] by converting the color image to an RGB stack, copying and pasting the coregistered fluorescence image into the green channel of the RGB stack with the paste transfer setting set to "maximum", and then converting the merged image back to an RGB color image.

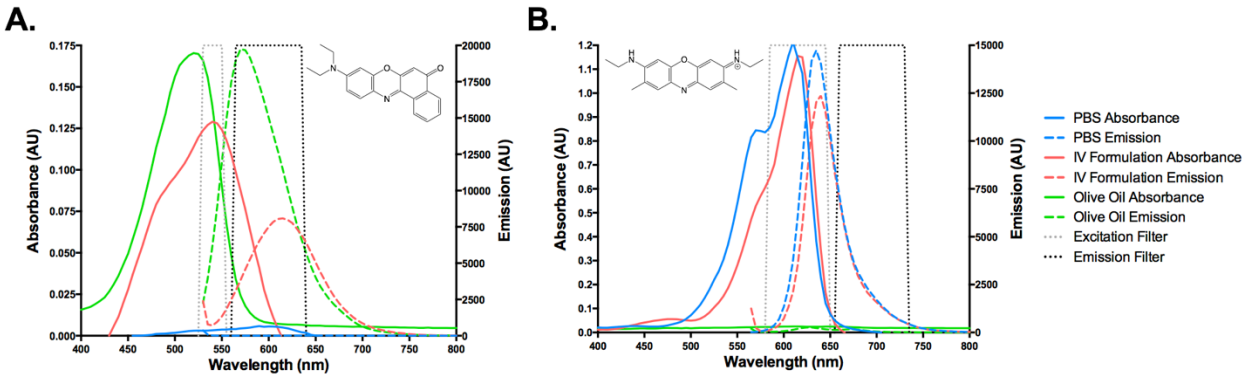

Figure 3.1: *Fluorescence spectra and structures of Oxazine 4 and Nile Red fluorophores.* **(A)** Absorbance and emission spectra for 10 µM **(A)** Nile Red and **(B)** Oxazine 4 in PBS, co-solvent formulation, or olive oil with overlaid excitation and emission filter spectra used for *in vivo* imaging. The fluorophore's chemical structures are inlaid into each graph.

Single Fluorophore Direct Administration Dose Ranging Studies

For direct administration of the nerve-specific fluorophore Oxazine 4, mouse brachial plexus or sciatic nerves were exposed and 100 μL of fluorophore co-solvent solution was applied covering the entire nerve site, submerging surrounding muscle, cut muscle, and adipose tissues in the fluorophore solution. Fluorophore dose testing studies were performed where 2.475 – 79.2 μg Oxazine 4 or 0.995 – 15.92 μg Nile Red in the co-solvent formulation were applied to the selected nerve site formulated in 100 μL of the co-solvent formulation (n=3 nerve sites/group; 6 Oxazine 4 groups, 5 Nile Red groups). Fluorophore solutions were incubated on the nerve site for 5 min before being removed by absorption with a clean gauze pad. Following removal of the fluorophore solution, the nerve site was washed using the incubation wash method where enough washing solution was applied to cover the nerve site and incubated for 1 min prior to removal. Three incubation washes were performed following fluorophore incubation with varied washing solutions including blank co-solvent formulation, PBS + 0.1% Triton X-100, and PBS + 0.1% Tween 20 in that order. The final Oxazine 4 and Nile Red doses were determined based on the calculated nerve and adipose to background tissue ratios, respectively.

Dual Fluorophore Staining for Spectral Tissue Separation & Cross Talk Quantification

Dual fluorophore staining and cross talk studies were performed using the chosen Oxazine 4 and Nile Red doses, which were determined to be 4.95 μg Oxazine 4 and 1.99 μg Nile Red in the co-solvent formulation. The Oxazine 4 and Nile Red solutions were incubated on the nerve site serially in both orders, Oxazine 4 then Nile Red (Oxa4/NR) or Nile Red then Oxazine 4 (NR/Oxa4), with a single wash of blank co-solvent formulation between incubations. Additionally, Oxazine 4 and Nile Red were also incubated on the nerve site simultaneously as a mixed co-stain solution containing both fluorophores in the co-solvent formulation (n=3 nerve sites/group; 3 groups). Each fluorophore solution was incubated on the nerve site for 5 min, followed by three incubation washes, 1 min in length each using blank co-solvent formulation, PBS + 0.1% Triton X-100, then PBS + 0.1% Tween 20. The final dual fluorophore staining order and degree of cross talk between Oxazine 4 and Nile Red fluorescence *in vivo* was determined based on the calculated nerve and adipose to background tissue ratios.

Fluorophore Incubation Time for Direct Administration

Incubation time testing studies using a serial stain of 4.95 μg Oxazine 4 in co-solvent formulation followed by 1.99 μg Nile Red in co-solvent formulation were performed with a 1, 3, or 5 min incubation time for each fluorophore with a single wash of blank co-solvent formulation between fluorophore incubations (n=3 nerve sites/group; 3 groups). Following the final fluorophore incubation, three incubation washes were performed using blank co-solvent formulation, PBS + 0.1% Triton X-100, then PBS + 0.1% Tween 20. The final staining time for Oxazine 4 and Nile Red fluorescence *in vivo* was determined based on the calculated nerve and adipose to background tissue ratios.

Nonspecific Fluorophore Removal Through Optimization of Washing Technique

The efficacy of incubation washing (1 min per wash with the three washing solutions including blank co-solvent formulation, PBS + 0.1% Triton X-100, and PBS + 0.1% Tween 20 utilized in that order) vs. flushing the nerve site with excess washing solution was tested using a serial stain of 4.95 μg Oxazine 4 in co-solvent formulation followed by 1.99 μg Nile Red in co-solvent formulation with 5 min incubation times for each fluorophore. Incubation washing was completed by applying enough washing solution to cover the nerve site and incubating for 1 min prior to removal. Flushing was completed by adding excess washing solution to the nerve site followed by removing it directly after application three times (n=3 nerve sites/group; 2 groups). For washing solution studies, PBS, PBS + 0.1% Tween 20, PBS + 0.1% Triton X-100, or blank co-solvent formulation was used as the sole washing solution per group and a series of 10 flush type washes were performed. The first flush step was completed during the serial staining procedure between Oxazine 4 and Nile Red fluorophore incubations and was considered flush step 1 with 9 subsequent flush steps following the Nile Red fluorophore incubation to reach 10 total flush steps (n=3 nerve sites/group; 4 groups). The final washing protocol and number of necessary flush steps was determined based on the calculated nerve and adipose to background tissue ratios.

Optimized Direct Administration of Fluorophores and Comparison to Systemic Administration in Murine Nerve Models

The most clinically viable fluorophore dose, incubation time, washing method, and washing solution were used for final direct administration studies to complete direct nerve staining on a clinically relevant time scale. 4.95 μg Oxazine 4 in 100 μL of the co-solvent formulation was incubated for 5 min on the nerve site for the Oxazine 4 individual stain and dual fluorophore staining groups. Blank co-solvent formulation was incubated on the nerve site for the control group (n=4 nerve sites per group; 3 groups). Following the first incubation, 3 flush steps were performed with 3 flushes of PBS per step. For the individual stain and control studies, blank co-solvent formulation was incubated on the nerve site for 5 min. For the dual fluorophore staining group, 1.99 μg Nile Red in 100 μL of the co-solvent formulation was incubated for 5 min on the nerve site following Oxazine 4 incubation serving both to stain adipose tissue and wash the Oxazine 4 stained tissue with the co-solvent formulation. Following the second incubation with either Nile Red or blank co-solvent formulation, 3 additional flush steps were performed with 3 flushes of PBS per step. During the final direct administration studies, the entire staining procedure was timed to quantify total staining time.

The nerve to background tissue ratios were compared between the final direct administration methodology and systemically administered fluorophore. For systemic administration of the nerve-specific fluorophore, the kinetics and dose of Oxazine 4 were previously optimized for rodent studies and utilized herein [74]. The Nile Red dose was scaled from the final direct administration dose determined in this study. For mice 200 nmol (79.2 μg) of Oxazine 4 or 100 nmol (31.8 μg) of Nile Red were administered intravenously, each formulated in 100 μL of co-solvent formulation. Intravenous administration was performed 4 hours prior to imaging, which has been shown previously to provide the highest nerve to background tissue fluorescence for Oxazine 4 and several other nerve specific fluorophores.[20, 66, 74] Animals were administered either Oxazine 4 individually for nerve-specific fluorescence imaging or both Oxazine 4 and Nile Red for dual fluorophore staining studies. Animals were administered blank co-solvent formulation for all control images (n=4 nerve sites/group; 3 groups).

Fluorophore Peritoneal Murine Biodistribution

To assess peritoneal background fluorescence, mice were administered 200 nmol (79.2 μg) of Oxazine 4 or 100 nmol (31.8 μg) of Nile Red intravenously in 100 μL of co-solvent formulation. 4 hours after administration the peritoneal cavity was exposed by excising overlying skin and muscle tissue. Images of the exposed peritoneal cavity were collected to include liver, stomach, intestine, pancreas, spleen, kidney, adipose, muscle, and bladder tissues. Mice were administered either Oxazine 4 individually or both Oxazine 4 and Nile Red. Mice were administered blank co-solvent formulation for all control images (n=3 mice/group; 3 groups).

Optimized Direct Administration of Fluorophores and Comparison to Systemic Administration to Highlight Autonomic Nerves in Rat Models

Rat hypogastric nerves and aortic plexuses were stained using the final direct administration methodology developed in murine models. The hypogastric nerves and aortic plexus were selected as representative autonomic nerves with close proximity to the prostatic nerves that were surgical accessible in the peritoneal cavity of rats.[139, 146, 147] Nerve SBR in the hypogastic nerves and aortic plexuses after direct administration was compared to nerve SBR in these same nerve structures following systemic administration. For direct administration, the Oxazine 4 and Nile Red doses were scaled by body surface area from murine studies to 9.9 μg and 3.98 μg, respectively formulated in 200 μl of co-solvent maintaining equivalent fluorophore concentration to that used for murine studies. Similar to the murine direct administration studies, formulated fluorophore was applied to the exposed nerve site fully submerging the nerve as well as the surrounding muscle and adipose tissues. For comparison to systemic administration, Oxazine 4 and Nile Red doses were again scaled by body surface area to 158.4 μg and 63.6 μg, respectively which were each administered in 200 μl of co-solvent formulation.[42]

For direct administration studies, the nerve sites were exposed and stained using the final protocol for either Oxazine 4 alone or Oxazine 4 and Nile Red dual fluorophore staining as described for mouse studies. For systemic administration, Oxazine 4 alone or Oxazine 4 and Nile Red were administered intravenously 4 hours prior to exposure of the selected nerve sites for imaging. The nerve SBR for each administration route using both single and dual staining techniques were compared (n=4 nerve sites/group; 5 groups). To aid in visualization of the nerves in the context of prostate tissue, the rat nerves stained using the direct administration method were

resected along with surrounding muscle, adipose and connected prostate tissue following sacrifice. The resected tissue was imaged to show the nerve-specific signal modeling the pedicle isolation completed during radical nerve-sparing prostatectomy as well as show the retrograde transport of the fluorophore in the nerves tissue following completion of direct administration staining. Additionally, the stained hypogastric and aortic plexus nerve sites were covered in varying amounts of blood and imaged to simulate light and heavy bleeding that could occur during a prostatectomy procedure. To further demonstrate the ability to stain prostate innervation using the direct administration procedure, rat prostate and hypogastric nerve tissue was stained *in vivo* using the direct administration procedure and imaged following resection.

Histological Confirmation of Rat Autonomic Nerve Tissue

Rat hypogastric nerve tissue stained *in vivo* with the final direct administration procedure was resected along with adjacent muscle following euthanasia 30 min after the final flush step of the staining procedure and snap frozen in optimal cutting temperature (OCT) compound using liquid nitrogen. Serial cryosections were cut at 10 μm onto superfrost plus slides (Fisherbrand, Fisher Scientific). Three consecutive sections were stained with hematoxylin and eosin (H&E), left unstained and mounted with glycerol for imaging of Oxazine 4 fluorescence, or costained first with FluoroMyelin Red (ThermoFisher Scientific, Waltham, MA) fluorescent myelin stain (1:300 dilution in deionized water) and then NeuroTrace Blue (ThermoFisher Scientific, Waltham, MA) fluorescent Nissl stain (1:100 dilution in PBS) according to the manufacturer's instructions. Fluorescence and color microscopy images were collected on an AxioObserver inverted fluorescence microscope (Zeiss, Thornwood, NY) at 10x magnification. Color H&E images were collected using the built in transillumination white light unfiltered and an Axiocam 105 color camera (Zeiss). For fluorescence excitation, a Photofluor LM-75 light source (89 North, Burlington, VT) filtered with a 405 ± 20 nm, 545 ± 12.5 nm, or 620 ± 60 nm was used to excite Neurotrace Blue, Fluoromyelin Red, or Oxazine 4 fluorescence, respectively. Resulting fluorescence was collected with a 550 ± 25 nm, 605 ± 35 nm, or 700 ± 37.5 nm bandpass emission filter for Neurotrace Blue, Fluoromyelin Red, or Oxazine 4 image collection, respectively (**Fig. 3.1**). All filters were obtained from Chroma Technology (Bellows Falls, VT). Fluorescence images were acquired using

an Axiocam 506 (Zeiss). Camera exposure times ranged from 50 – 6000 ms for fluorescence image collection.

Intraoperative Nerve Imaging and Image Analysis

Nerve specific contrast was assessed for all fluorophore optimization studies using the intraoperative fluorescence imaging system to collect images of the nerves and surrounding tissues. For systemic administration mouse studies, the brachial plexus and sciatic nerves were exposed and images were collected for each mouse 4 hours post injection. For systemic administration rat studies, the hypogastic nerve and aortic plexus were exposed and images were collected for each rat 4 hours post injection. Additional vehicle injected control animals were imaged to assess tissue autofluorescence for comparison to the systemically administered animals. For direct administration mouse studies, the brachial plexus and sciatic nerves were exposed and images were collected prior to any staining enabling each animal to act as its own control. Similarly, for direct administration rat studies, the hypogastic and aortic plexus were exposed and images were collected prior to any staining enabling each animal to act as its own control. In addition, the final direct administration procedure was completed with blank co-solvent formulation to ensure no nerve-specific fluorescence could be attributed to the co-solvent formulation alone. For all murine direct administration optimization studies, images were collected following every incubation or wash step. For the final murine direct administration studies, images were collected prior to the second co-solvent incubation, after the final wash step, and at 5 min intervals for up to 30 min after the final wash step to observe any changes in SBR that occurred following completion of staining. For the rat direct administration studies, images were collected after the final wash step and 30 min after the completion of the final wash step to observe any changes in the SBR that occurred following completion of staining.

Region of interest analysis was performed for each collected image of the nerve site to determine the fluorescence intensity from nerve, muscle, cut muscle, and adipose tissues. For images captured of Oxazine 4 fluorescence, the nerve to muscle (N/M), nerve to cut muscle (N/CM), and nerve to adipose (N/A) ratios were calculated using the intensity measurements for each tissue type. For images captured of Nile Red fluorescence, the adipose to muscle (A/M), adipose to cut muscle (A/CM), and adipose to nerve (A/N) ratios were calculated. This enabled the mean nerve to background tissue ratios (N/M, N/CM, N/A) and adipose to

background tissue ratios (A/M, A/CM, and A/N) to be calculated for each group. Due to differences in the surgical model, no cut muscle tissue was stained during the rat direct administration studies, so this tissue type was excluded from that analysis. For murine peritoneal biodistribution studies, region of interest analysis was performed for each image of the peritoneal cavity to determine the fluorescence intensity from liver, stomach, intestine, pancreas, spleen, kidney, adipose, muscle, and bladder tissue. The peritoneal cavity fluorescence intensities were then divided by the exposure time in seconds to obtain intensity per second measurements for each tissue type.

Statistical Analysis

Significant differences between fluorophore incubation group means were evaluated using a one-way ANOVA followed by Tukey's multiple comparison test to compare all mean nerve and adipose to background tissue ratios in each study with three or more treatment groups. For the incubation time testing study, an unpaired two-tailed Student's t test with equal variance was used to evaluate significant differences between the two incubation times. To compare the final direct administration procedure with systemic administration in both the final murine and rat nerve studies an unpaired two-tailed Student's t test with equal variance was used to evaluate significant differences between the two administration routes. The α value was set to 0.05 for all analyses. Results were presented as mean ± standard deviation (S.D.). All statistical analysis was performed using GraphPad Prism (La Jolla, CA).

RESULTS

Single Fluorophore Dose Ranging Studies

A range of Oxazine 4 (2.475 – 79.2 μg/nerve site) or Nile Red (0.995 – 15.92 μg/nerve site) doses in co-solvent formulation (10% dimethyl sulfoxide (DMSO), 5% Kolliphor EL, 65% serum, and 20% phosphate buffered saline (PBS) [20, 112]) were tested to optimize the fluorophore dose for direct administration to nerve tissue. Co-solvent formulated Oxazine 4 or Nile Red was applied to exposed murine brachial plexus or sciatic nerves *in vivo* (**Fig. 3.2**). Images of each nerve site were collected following washing to remove unbound fluorophore using a 2.5 ms exposure time for

equal comparison across all doses. Lower doses of fluorophore resulted in decreased nerve or adipose tissue fluorescence intensity. However, a greater decrease in non-specific muscle tissue fluorescence with decreasing fluorophore dose led to an increase in the nerve to muscle (N/M) contrast for Oxazine 4 (**Fig. 3.2A**) and adipose to muscle (A/M) contrast for Nile Red (**Fig. 3.2B**).

Region of interest analysis was performed to calculate the N/M, nerve to cut muscle (N/CM), nerve to adipose (N/A), A/M, adipose to cut muscle (A/CM), and adipose to nerve (A/N) ratios from representative tissues. Lower doses of Oxazine 4 (19.8 – 2.475 μg/nerve site) had significantly higher N/M ratios than the highest Oxazine 4 dose (79.2 μg/nerve site: $p=0.0011$ for 19.8 μg, $p=0.023$ for 9.9 μg, $p=0.0011$ for 4.95 μg, and $p=0.0038$ for 2.475 μg). The N/M ratio linearly increased for Oxazine 4 as the fluorophore dose was reduced from 79.2 to 19.8 μg/nerve site, while minimal N/M ratio change was observed when the fluorophore dose was further reduced to 2.475 μg/nerve site. The N/CM ratio linearly increased for Oxazine 4 when the dose was reduced from 39.6 to 9.9 μg/nerve site. Little N/CM difference was seen when the dose was reduced from 79.2 to 39.6 μg/nerve site or from 9.9 to 4.95 μg/nerve site. However, the mean N/CM ratio decreased when the Oxazine 4 dose was reduced from 4.95 to 2.475 μg/nerve site. The mean N/A ratio remained relatively constant across all tested doses (**Fig. 3.2C**). The Oxazine 4 dose that yielded the highest N/M and N/CM ratios was 4.95 μg/nerve site, which was selected as the final dose for direct administration.

The mean A/M ratio showed no significant change across the entire tested Nile Red dose range (15.92 – 0.995 μg/nerve site). The mean A/CM ratio showed no significant change following doses ranging from 15.92 to 1.99 μg/nerve site, however the mean A/CM ratio decreased at the lowest tested dose (0.995 μg/nerve site). The mean A/N ratio also showed no significant change across all tested doses (**Fig. 3.2D**). The final Nile Red dose selected for direct administration was 1.99 μg/nerve site, which minimized fluorophore dose while maintaining high A/M, A/CM, and A/N ratios.

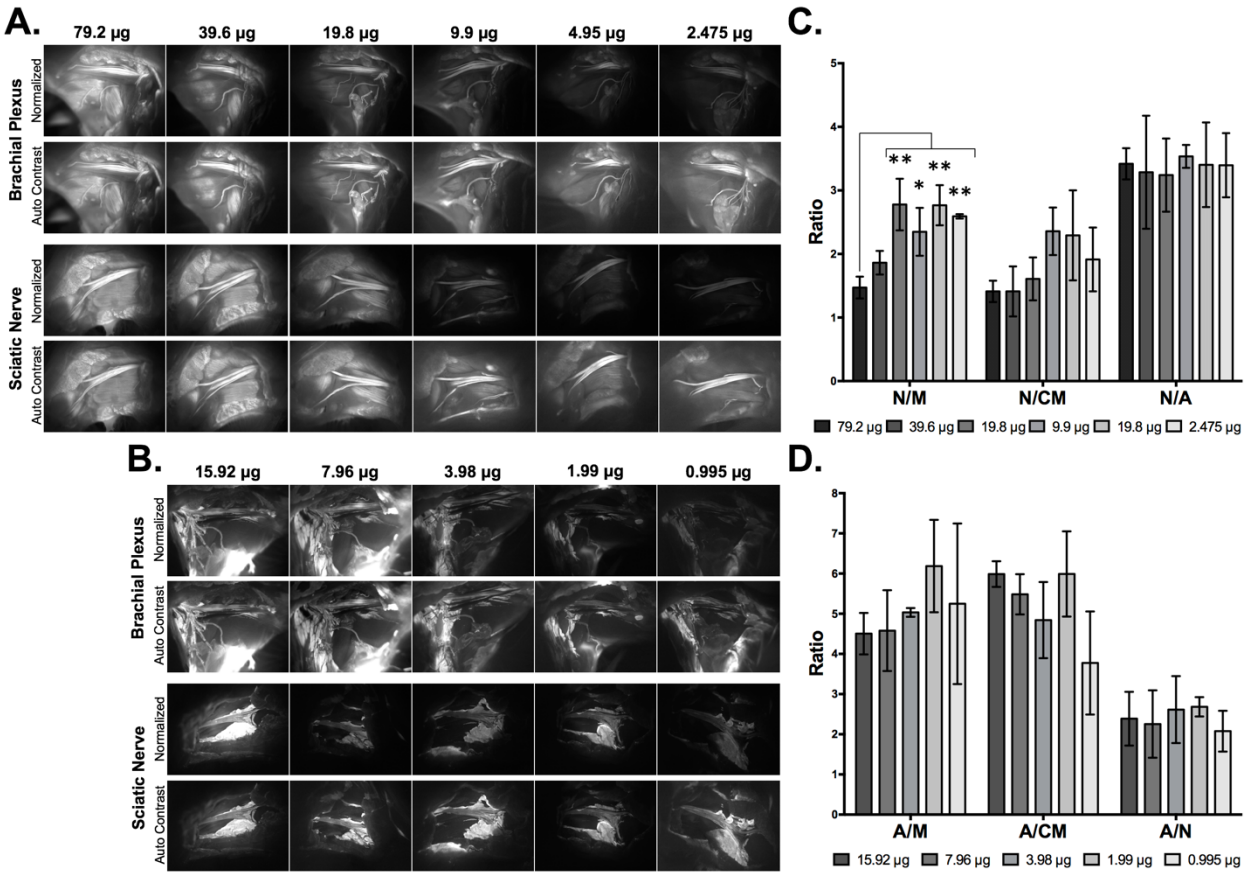

Figure 3.2: *Single fluorophore direct administration dose ranging studies*. Representative fluorescence images of the brachial plexus and sciatic nerve sites following direct fluorophore administration are shown for **(A)** Oxazine 4 and **(B)** Nile Red. All images are representative of data collected for n=3 nerve sites per dose. Doses were administered in a 100 µL volume of co-solvent formulation. All images were collected after the final wash step at 2.5 ms exposure time and images within each row labeled "Normalized" are displayed with equal contrast and brightness. The images labeled "Auto Contrast" are displayed with optimal contrast and brightness for each image to enable visualization of the nerve and adipose to background tissue contrast. The nerve to background tissue **(C)** and adipose to background tissue **(D)** ratios were determined using region of interest analysis on images collected following the final wash step, presented as the mean +/- the standard deviation. N/M = nerve to muscle ratio, N/CM = nerve to cut muscle ratio, N/A = nerve to adipose ratio, A/M = adipose to muscle ratio, A/CM = adipose to cut muscle ratio, A/N = adipose to nerve ratio. * = p value < 0.05, ** = p value < 0.01.

Dual Fluorophore Staining for Spectral Nerve and Adipose Tissue Separation

Adipose tissue accumulation has plagued previous nerve-specific fluorophores, yielding relatively low N/A ratios.[20, 66, 68, 69] A dual fluorophore staining technique was investigated using the final dose of the nerve-specific Oxazine 4 (4.95 µg/nerve site) and adipose-specific Nile Red (1.99 µg/nerve site) to

specifically highlight both nerve and adipose tissues (**Fig. 3.3**). The dual staining protocol was tested where serial staining, in which Oxazine 4 was incubated first followed by Nile Red (Oxa4/NR) or vice-versa (NR/Oxa4), and simultaneous staining, where both fluorophore solutions were co-incubated on the tissue, were tested. The serial staining techniques yielded higher nerve and adipose to background tissue contrast than the simultaneous staining technique. While the serial and simultaneous staining techniques yielded similar nerve and adipose fluorescence intensities, the non-specific muscle fluorescence was lower using the serial staining technique (**Fig. 3.3A**).

The Oxa4/NR serial stain resulted in the highest mean N/M, N/CM, and N/A ratios when compared to the NR/Oxa4 serial, simultaneous dual or individual fluorophore staining techniques, with a significantly higher N/M ratio than the simultaneous dual staining technique ($p=0.023$, **Fig. 3.3B**). The Oxa4/NR serial stain also resulted in the highest mean A/M, A/CM, and A/N ratios compared to the other dual fluorophore staining techniques. The Nile Red individual staining yielded the highest mean adipose to background tissue ratios, however, this was not pursued further in the current study as our goal was to provide nerve-specific contrast.

Both the Nile Red and Oxazine 4 fluorophores have relatively broad emission spectra with some overlap (**Fig. 3.1**), necessitating quantification of the degree of cross talk between the intraoperative imaging channels. The fluorescence intensities for nerve, muscle, cut muscle, and adipose tissues stained serially, simultaneously, or individually were determined using region of interest analysis throughout the staining procedure to quantify cross talk between Oxazine 4 and Nile Red using the *in vivo* fluorescence imaging system (**Figs. 3.4A and 3.4B**). Nile Red fluorescence was not detected in the Oxazine 4 imaging channel (**Fig. 3.4A**). However, staining with Oxazine 4 prior to the Nile Red incubation showed an increase in fluorescence intensity from baseline for nerve, muscle, and cut muscle tissues in the Nile Red channel (**Fig. 3.4B**). These results suggest that Oxazine 4 fluorescence was detected in the Nile Red channel, but no Nile Red fluorescence was detected in the Oxazine 4 channel. Therefore, there was no interference with the nerve specific fluorescence imaging from the addition of the adipose specific fluorophore.

To elucidate the mechanism of nerve and adipose tissue contrast following direct administration, the N/M, N/CM, N/A, A/M, A/CM, and A/N ratios were calculated after each step in the direct administration staining protocol (**Figs. 3.4C and 3.4D**). As previously demonstrated, the serial Oxazine 4 then Nile Red staining

yielded the highest mean N/M, N/CM, and N/A ratios (**Fig. 3.4C**). This co-staining technique resulted in similar nerve tissue intensity, but lower nonspecific muscle, cut muscle, and adipose tissue intensities, than all other nerve tissue staining techniques (**Fig. 3.4A**). As expected, the Nile Red individual staining technique yielded the highest mean A/M, A/CM, and A/N ratios (**Fig. 3.4D**). Individual Nile Red staining showed similar nonspecific nerve, muscle, and cut muscle tissue intensities to all other Nile Red staining techniques, but higher adipose tissue intensity (**Fig. 3.4B**). Thus, nerve and adipose to background tissue contrast using Oxazine 4 and Nile Red were created by two different mechanisms. Oxazine 4 initially stained nerve, muscle and adipose tissue where muscle and adipose tissue fluorescence was largely removed through washing of unbound fluorophore. On the other hand, Nile Red staining created specific fluorescence in the adipose tissue with little detectable fluorescence signal in surrounding nerve and muscle tissues.

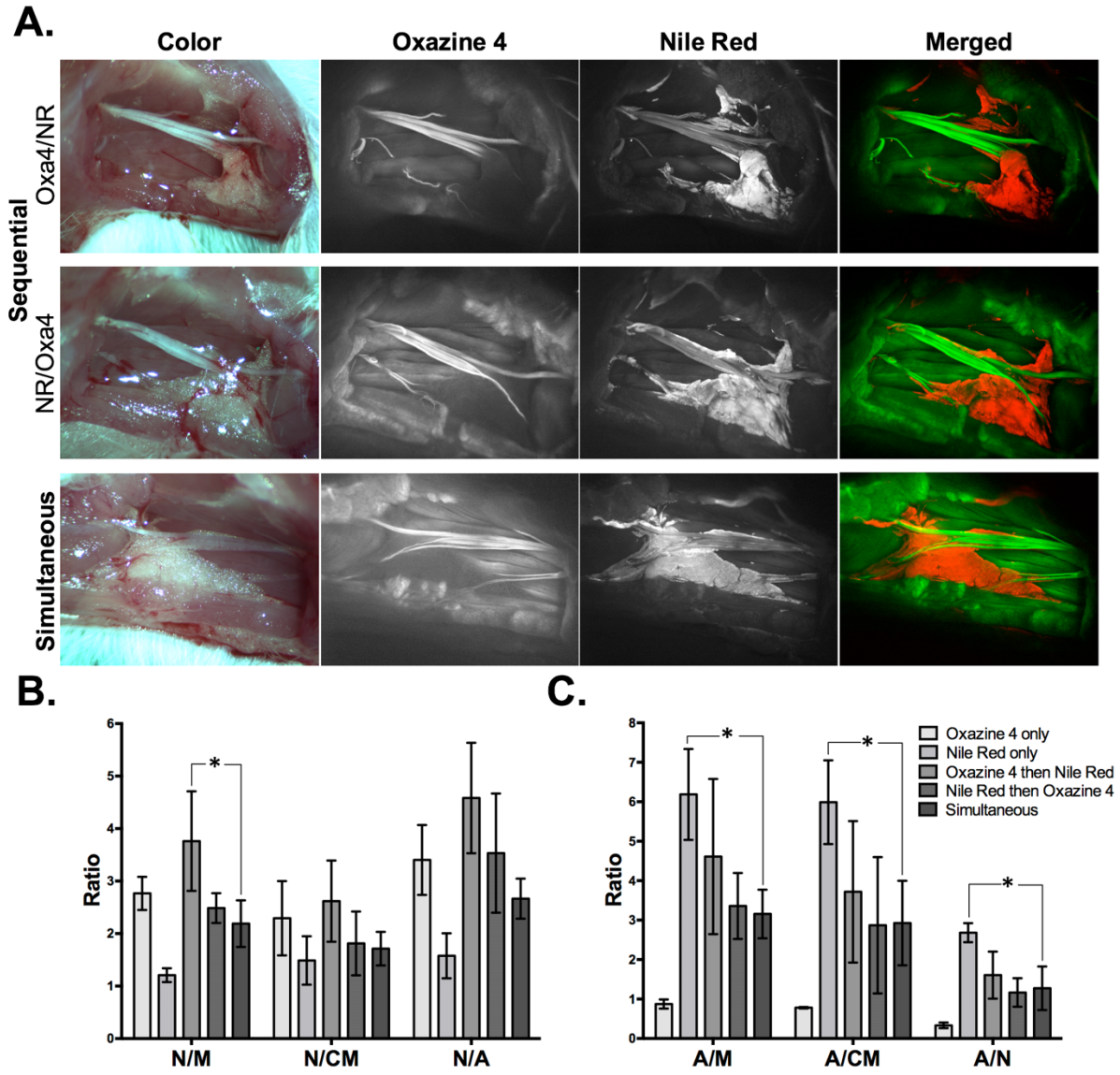

Figure 3.3: *Dual fluorophore staining technique for nerve and adipose spectral separation*. **(A)** Representative color and fluorescence images for sequential and simultaneous dual fluorophore tissue separation staining techniques using Oxazine 4 and Nile Red are shown. All images are representative of data collected for n=3 nerve sites per staining technique. All images were collected after the final wash step at 2.5 ms exposure time. Merged images were created by merging the Oxazine 4 signal false colored green with the Nile Red false colored red minus the Oxazine 4 signal (to remove any potential overlap due to crosstalk). **(B)** The Oxazine 4 nerve to background tissue ratios and **(C)** Nile Red adipose to background tissue ratios were determined using region of interest analysis on images collected after the final wash step for individual and dual fluorophore staining techniques in each fluorophore's respective channel, presented as the mean +/- standard deviation. N/M = nerve to muscle ratio, N/CM = nerve to cut muscle ratio, N/A = nerve to adipose ratio, A/M = adipose to muscle ratio, A/CM = adipose to cut muscle ratio, A/N = adipose to nerve ratio. * = p value < 0.05.

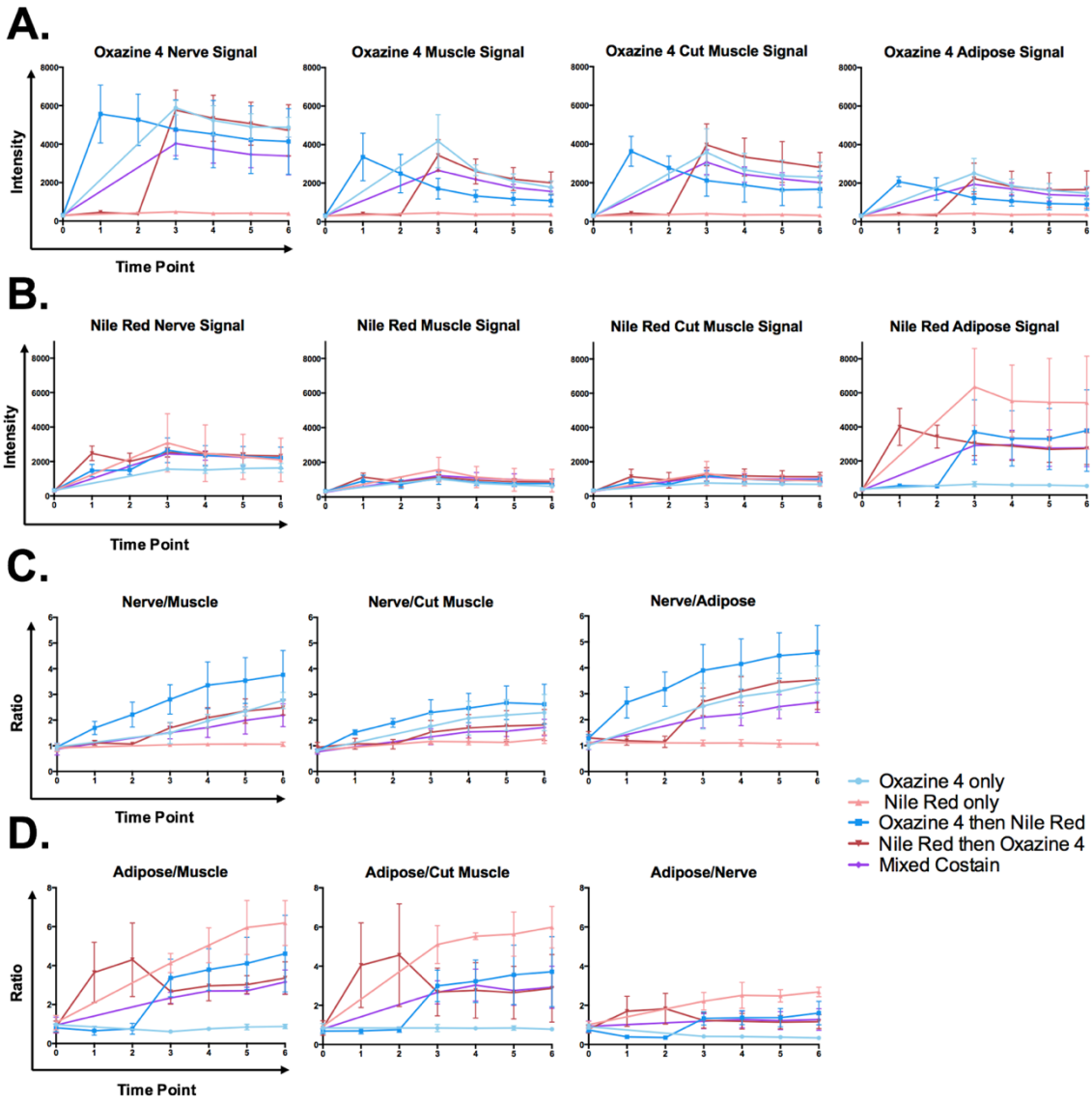

Figure 3.4: *Fluorophore cross-talk between Oxazine 4 and Nile Red.* Fluorescence signal intensities for each major visible tissue type and nerve to background tissue ratios were determined using region of interest analysis on images collected in the **(A)** Oxazine 4 fluorescence channel or **(B)** Nile Red fluorescence channel. The **(C)** nerve or **(D)** adipose to background tissue ratios were calculated from the intensity values determined through region of interest analysis. All data was determined from images collected for n=3 nerve sites at several time points: 0 = prior to the initial Oxazine 4 incubation, 1 = following the Oxazine 4 incubation, 2 = following the first blank co-solvent formulation wash, 3 = following the Nile Red incubation, 4 = following the second blank co-solvent formulation wash, 5 = following the PBS + 0.1% Triton X-100 wash, 6 = following the PBS + 0.1% Tween-20 wash. Time point 0 was considered the baseline fluorescence intensity for each tissue type. The data was determined from images collected at either 1 s exposure time for the time 0 point images or 2.5 ms exposure time for all other time points. All data in presented as mean +/- standard deviation.

Fluorophore Incubation Time

The final fluorophore dose and dual fluorophore staining technique were determined using a 5-min fluorophore incubation time. In an effort to reduce the total direct administration protocol time, fluorophore incubation times of 1 and 3 min were tested (**Fig. 3.5**). The shorter incubation times of each fluorophore during the dual fluorophore tissue stain resulted in decreased nerve and adipose tissue fluorescence intensity. Since the fluorescence intensities of the background tissues did not decrease to the same extent, this led to decreased nerve (**Fig. 3.5A**) and adipose (**Fig. 3.5B**) to background tissue contrast using 1 and 3 min fluorophore incubation.

The nerve and adipose to background tissue ratios were calculated using region of interest analysis to quantify the observed contrast loss at the shorter incubation times. Decreased mean nerve and adipose to background tissue ratios were observed in all but two cases. The 3-min incubation time resulted in a slight increase in the mean A/CM ratio and A/N ratio, however these changes were not significant (**Figs. 3.5C and 3.5D**). Five min was selected as the final incubation time for direct administration since the shorter incubation times yielded lower nerve to background tissue contrast, A/M ratio, and did not provide significant improvement in the A/CM or A/N ratios.

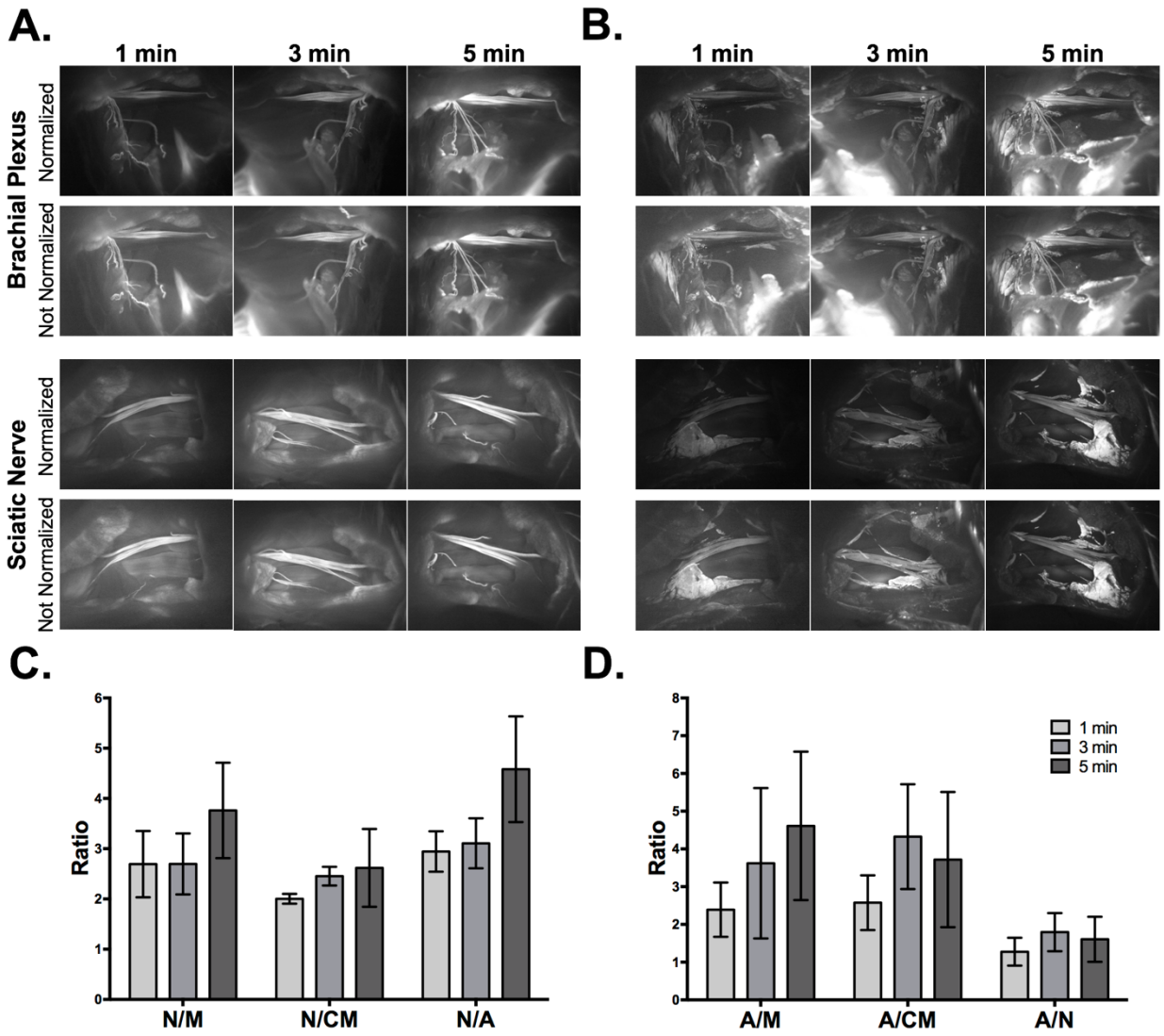

Figure 3.5: *Direct administration fluorophore incubation time testing.* Representative fluorescence images for each incubation time in the **(A)** Oxazine 4 or **(B)** Nile Red channels are shown. All images are representative of data collected for n=3 nerve sites per incubation time. All images were collected after the final wash step at 2.5 ms exposure time. Images within each row labeled "Normalized" are displayed with equal contrast and brightness. The images labeled "Auto Contrast" are displayed with optimal contrast and brightness for each image to enable visualization of the nerve and adipose to background tissue contrast. **(C)** The nerve and **(D)** adipose to background tissue ratios were determined using region of interest analysis on images collected following the final wash step, presented as the mean +/- standard deviation. N/M = nerve to muscle ratio, N/CM = nerve to cut muscle ratio, N/A = nerve to adipose ratio, A/M = adipose to muscle ratio, A/CM = adipose to cut muscle ratio, A/N = adipose to nerve ratio.

Nonspecific Fluorophore Removal Through Optimization of Washing Technique

Generation of nerve-specific contrast following Oxazine 4 incubation was dependent on removal of unbound fluorophore from surrounding muscle and adipose tissues, highlighting the importance of an optimized washing technique. The washing method, solution composition, and duration were tested to maximize the removal of nonspecific fluorescence in the shortest possible time for clinical feasibility. In the dose ranging, incubation time and dual fluorophore staining studies, washing was completed using 1 min incubations of washing solution on the nerve site. These "incubation washes" were completed using a 1 min incubation of a series of solutions including co-solvent formulation without fluorophore (blank co-solvent), PBS + 0.1% Triton X-100, and PBS + 0.1% Tween-20 in that order. To shorten the washing protocol, nerve site flushing was tested. The flushing technique used three short flushes of the nerve site with washing solution, instead of incubating the washing solution on the tissue (**Fig. 3.6A**). Importantly, this reduced the necessary time to perform each wash step by 50%, decreasing the time for the direct administration staining procedure by 3 min. Washing with three short flushes removed nonspecific fluorescence similarly to incubation washing, with no significant difference between the two washing types for any nerve or adipose to background tissue ratio (**Fig. 3.6A**).

To further simplify the washing protocol, flushing with a single washing solution per nerve site was tested. PBS, PBS + 0.1% Tween-20, PBS + 0.1% Triton X-100, and blank co-solvent formulation were tested as the sole washing solution using a series of 10 flushes (**Fig. 3.6B)**. The detergents Tween-20 and Triton X-100 were chosen as surfactants that could potentially improve removal of non-specific fluorescence, both of which are commonly used as excipients in vaccines at concentrations up to 0.4%.[148, 149] Fluorescence images were collected following each flush step to calculate the nerve and adipose to background tissue ratios. All tested washing solutions showed a similar improvement in the nerve and adipose to background tissue ratios, with the blank co-solvent formulation yielding the lowest tissue contrast ratios and all three PBS solutions providing improved tissue contrast ratios (**Fig. 3.6C**).

PBS without any added detergents or surfactants was chosen as the final washing solution since it is most clinically relevant, without any potential regulatory obstacles from added solubilizers or surfactants. The images collected following

each flush step were used to determine the final number of flush steps. Nonspecific muscle fluorescence decreased considerably after two flush steps (**Figs. 3.6B and 3.6C**). However, calculated nerve and adipose to background tissue ratios indicate that the N/M and N/CM ratios increased linearly up to the sixth flush step for PBS washed nerve sites. The N/A ratio reached its highest level after just two flush steps and did not decrease over the ten performed flush steps. In addition, the A/M and A/CM ratios increased within the first 2-3 flush steps and remained at peak levels through the sixth flush step, after which they decreased (**Fig. 3.6C**).

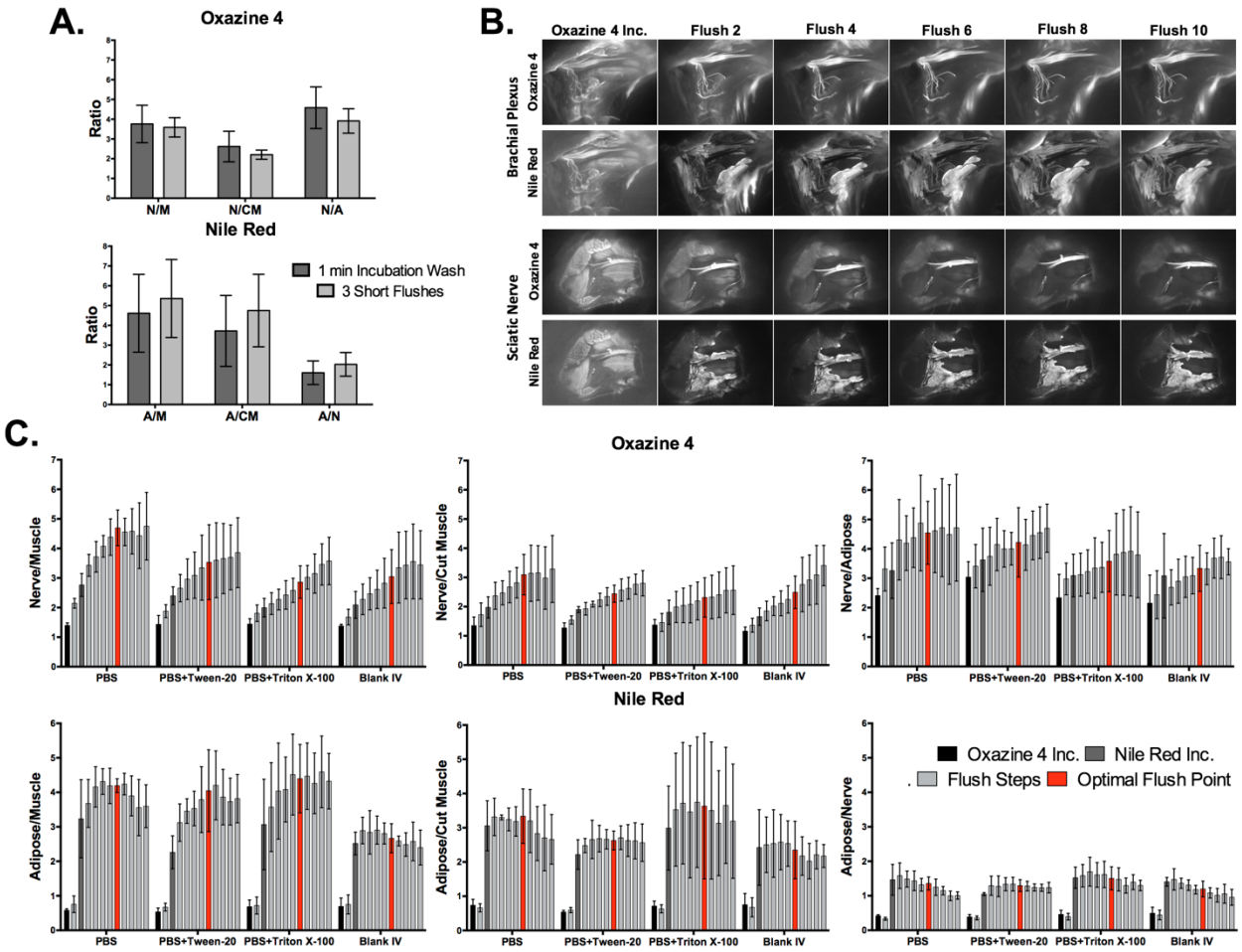

Figure 3.6: *Nonspecific fluorophore removal through optimization of washing technique*. **(A)** The nerve and adipose to background tissue ratios were determined using region of interest analysis on images collected after the final wash step for incubation and flush type washes, presented as the mean +/- standard deviation. **(B)** Representative fluorescence images for nerve sites washed with PBS in a series of 10 flush steps are shown. All images are representative of data collected for n=3 nerve sites following completion of each fluorophore incubation and flush step. All images were collected at 2.5 ms exposure time. **(C)** The nerve and adipose to background tissue ratios were determined using region of interest analysis on images collected after each of 10 flush steps for all washing solutions tested, presented as the mean +/- standard deviation. N/M = nerve to muscle ratio, N/CM = nerve to cut muscle ratio, N/A = nerve to adipose ratio, A/M = adipose to muscle ratio, A/CM = adipose to cut muscle ratio, A/N = adipose to nerve ratio.

Direct Administration vs. Systemic Administration: Comparison and Assessment of Clinical Viability in Murine Models

The final direct administration protocol was completed using a clinically relevant scenario with the chosen fluorophore doses, dual fluorophore staining technique, incubation time, and washing methodology. Images were collected at a

single time point during direct administration and the entire protocol was timed to quantify the total time required for staining and imaging. For comparison, systemic administration of Oxazine 4 and Nile Red was performed with the final fluorophore doses and imaging interval according to previous studies (**Figs. 3.7A and 3.7B**).[74, 108] The necessary exposure time to collect fluorescence images without saturation was 10 ms for the direct administration group in both the Oxazine 4 and Nile Red channels. By comparison, the exposure time to collect fluorescence images without saturation for the systemic administration group was 150 ms for Oxazine 4 and 300 ms for Nile Red. Although the fluorescence intensity was low, 10 ms exposure time images of the systemic administration groups were also collected for equal comparison with the direct administration groups and to represent images taken at video-rate exposure times. As demonstrated by the differences in exposure time, direct administration yielded higher fluorescence intensity in all cases as compared to systemic administration. The direct administration methodology highlighted finer nerve branches and smaller adipose tissue deposits than systemic administration enabling a higher level of detail to be resolved due to improved fluorophore specificity (**Figs. 3.7A and 3.7B**).

The nerve and adipose to background tissue ratios were quantified from both administration types as well as a blank co-solvent administered control group (**Figs 3.7C)**. The direct (10 ms) and systemic (150 ms) Oxazine 4 administration groups both had significantly higher N/M, N/CM, and N/A ratios than the control group for both the individual stain (direct administration: $p=0.0092$ for N/M, $p=0.0098$ for N/CM, and $p<0.0001$ for N/A, systemic administration: $p=0.0007$ for N/M, $p<0.0001$ for N/CM, and $p<0.0001$ for N/A) and the dual fluorophore stain (direct administration: $p=0.0074$ for N/M, $p<0.0001$ for N/CM, and $p=0.0005$ for N/A, systemic administration: $p=0.0001$ for N/M, $p<0.0001$ for N/CM, and $p=0.0004$ for N/A). Dual fluorophore stained tissue at ideal exposure times (10 ms direct, 300 ms systemic, Nile Red channel) had significantly higher A/M and A/CM ratios than the control group in both the direct ($p=0.0004$ for A/M and $p=0.0016$ for A/CM) and systemic administration groups ($p=0.0094$ for A/M and $p=0.0123$ for A/CM). At the optimal exposure time for each administration technique, direct administration provided equivalent nerve to background tissue contrast to systemic administration in both the individual Oxazine 4 ($p=0.29$ for N/M, $p=0.060$ for N/CM, and $p=0.3883$ for N/A) and the dual fluorophore staining ($p=0.10$ for N/M, $p=0.19$ for N/CM, and $p=0.94$ for N/A) groups as no significant differences were seen (**Figs. 3.7A and**

3.7B). In addition, no significant difference was seen between direct and systemic Nile Red administration groups for adipose to background tissue ratios at the ideal exposure times for each administration route (p=0.35 for A/M, p=0.78 for A/CM, p=0.064 for A/N).

However, at video rate exposure time (10 ms), the direct administration group had significantly higher N/M and N/A ratios for the individual stain (p=0.042 for N/M and p=0.0006 for N/A) and significantly higher N/CM and N/A ratios for the dual fluorophore stain (p=0.021 for N/CM and p=0.0033 for N/A) than the systemic administration group (**Fig. 3.7C**). Video rate imaging of systemically administered Oxazine 4 resulted in no significant difference in N/M and N/A ratios from the control group for the dual fluorophore stain (p=0.12 for N/M and p=0.056 for N/A). Additionally, at the video rate exposure time the direct administration group had significantly higher adipose to background tissue ratios than systemic administration (p=0.0032 for A/M, p=0.0004 for A/CM, and p=0.032 for A/N) (**Fig. 3.7C**). Video rate imaging of the systemic administration group did not have significantly higher adipose to background tissue ratios than the control group (p=0.78 for A/M and p=0.29 for A/CM).

Following completion of the final direct administration protocol, images were collected at 5 min intervals for up to 30 min after the final wash step to quantify the nerve and adipose to background tissue ratios over time (**Figs. 3.7D and 3.7E**). The N/M and N/CM ratios increased steadily over the 30-min period in both the Oxazine 4 individual stain (**Fig. 3.7D**) and dual fluorophore staining groups (**Fig. 3.7E**), indicating continued clearance of nonspecific muscle uptake over time. Overall, the final direct administration nerve staining protocol was completed within 15 minutes, after which peak nerve contrast was maintained for up to 30 minutes. By comparison, systemic administration required 5 minutes to complete the injection and 4 hours to obtain peak nerve to background tissue contrast. In addition, direct administration required 16x less dose as well as 15x lower exposure time than systemic administration for an equivalent nerve to background tissue contrast (**Table 3.1**). Biodistribution of Oxazine 4 and Nile Red were evaluated following systemic administration. A mixture of hepatic and renal clearance was observed with significant accumulation in the bladder at the peak fluorophore administration to imaging interval of 4 hours (**Fig. 3.8**). Due to the proximity of the prostate to the bladder, this would cause significant background fluorescence that may overwhelm desired nerve-specific fluorescent signal.

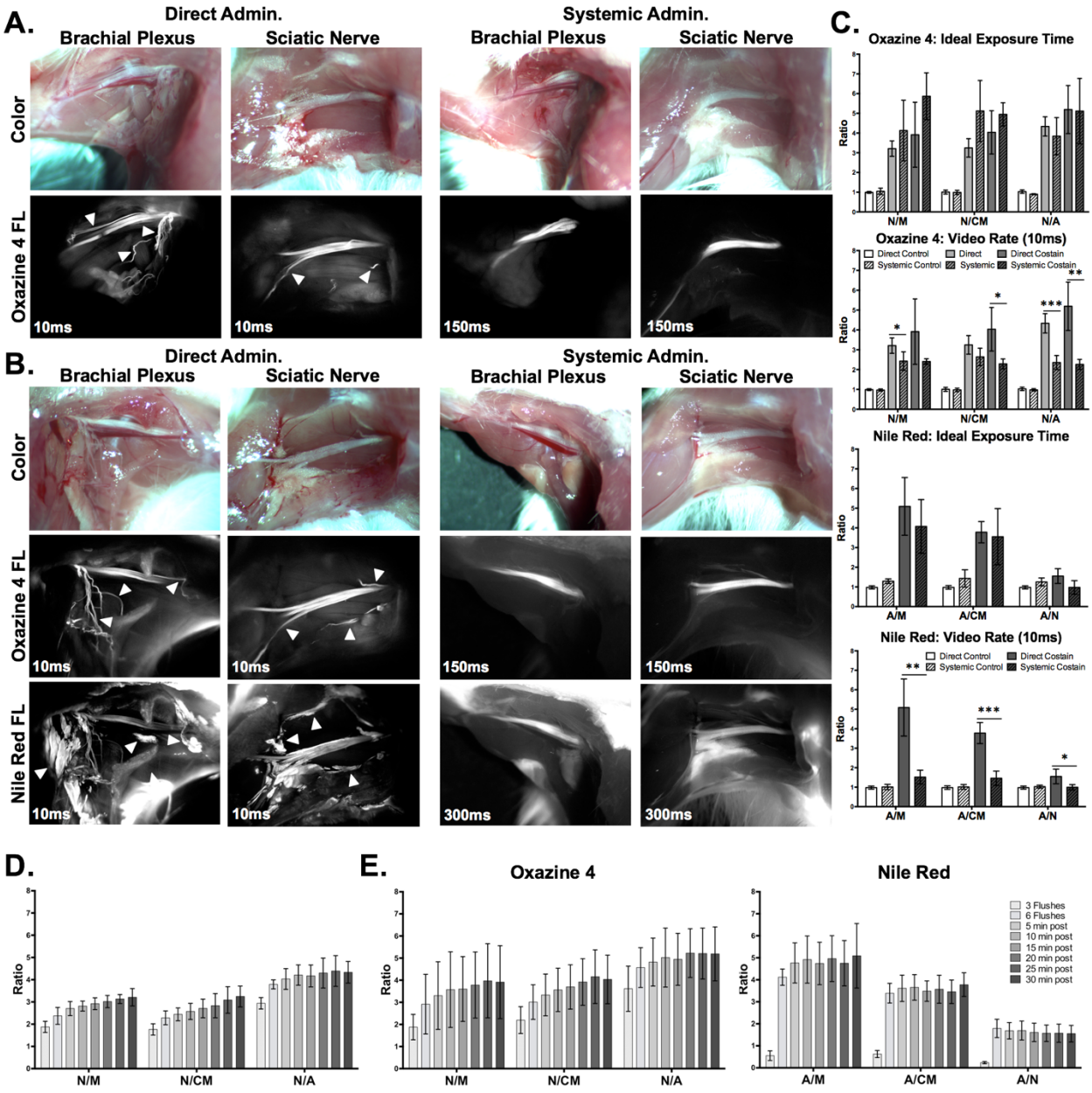

Figure 3.7: *Direct administration vs. systemic administration: comparison and assessment of clinical viability in murine peripheral nerve models*. Representative color and fluorescence images for **(A)** individual Oxazine 4 or **(B)** dual fluorophore stained nerve sites for direct and systemic administration methods are shown. All images are representative of data collected for n=4 nerve sites either 30 min following the final flush step for direct administration or 4 hrs following intravenous injection for systemic administration. **(C)** The nerve and adipose to background tissue ratios were determined using region of interest analysis on images collected at the same time intervals for direct and systemic administration methods. The data for the ideal exposure time graphs was determined using 10 ms exposure time images for the direct administration groups and 150 or 300 ms exposure time images for the systemic administration groups in the Oxazine 4 or Nile Red channel, respectively. The data for the video rate graphs was determined using 10 ms

exposure time images only. **(D)** The nerve to background tissue ratios were determined following completion of the final direct administration protocol of Oxazine 4 individual stain. **(E)** The nerve and adipose to background tissue ratios were determined for the final direct administration dual staining technique. Quantification for the data in **(D)** and **(E)** was completed following 3 flush steps, following 6 flush steps, and every 5 min for 30 min following completion of the staining procedure. The data was determined from images collected at 10 ms. All quantified data is presented as mean +/- standard deviation. FL = fluorescence, N/M = nerve to muscle ratio, N/CM = nerve to cut muscle ratio, N/A = nerve to adipose ratio, A/M = adipose to muscle ratio, A/CM = adipose to cut muscle ratio, A/N = adipose to nerve ratio. * = p value < 0.05, ** = p value < 0.01, *** = p value < 0.001, *** = p value < 0.0001.

Table 3.1: *Clinical viability of direct and systemic administration methods*.

Parameter	Direct Administration	Systemic Administration
Dose:	4.95 µg (12.5 nmol) per nerve site	79.17 µg (200 nmol) per mouse
Time to complete staining procedure:	15 minutes	<5 minutes via IV injection
Time to peak fluorescence:	20-30 minutes	4 hours
Total staining time:	15 minutes	4 hours 5 minutes
Nerve to muscle ratio at ideal exposure time:	3.211 +/- 0.390	4.128 +/- 1.538
Nerve to muscle ratio at video rate:	3.211 +/- 0.390	2.428 +/- 0.467

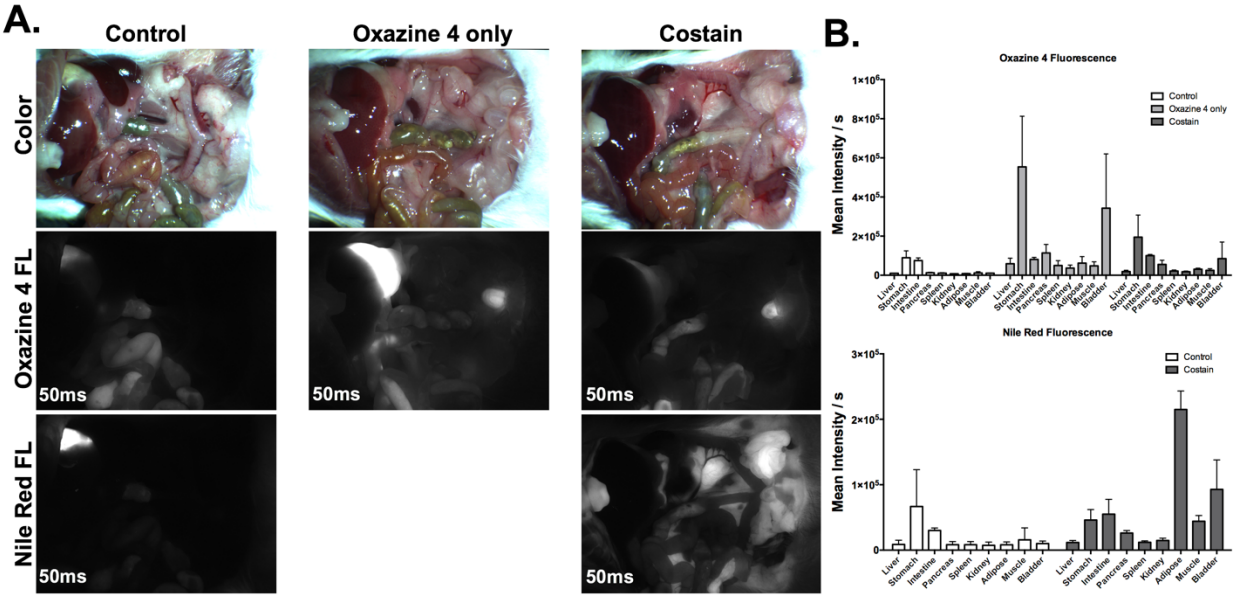

Figure 3.8: *Fluorophore peritoneal biodistribution following systemic administration.* **(A)** Representative color and fluorescence images for control blank co-solvent, Oxazine 4 only, and Oxazine 4 with Nile Red co-stain systemically administered mice. **(B)** Fluorophore biodistribution was quantified using region of interest analysis. The mean intensities normalized to exposure time (Mean Intensity/second (s)) as shown. All images were collected at 50 ms exposure time and are displayed with equal contrast and brightness. The data is presented as mean +/- standard deviation.

Direct Administration vs. Systemic Administration: Comparison and Assessment of Clinical Viability in Rat Autonomic Nerve Models

The final direct administration protocol was applied to the rat hypogastric nerve and aortic plexus, which served as surgically accessible autonomic nerves that model the composition and smaller size of the cavernous nerves as compared to the brachial plexus and sciatic nerves used for murine studies.[139, 146, 147] The rat doses of Oxazine 4 and Nile Red for both direct and systemic administration were scaled from the murine studies by body surface area equivalence.[150] Direct administration was compared to systemic administration of individual staining using Oxazine 4 alone (**Fig. 3.9A**) as well as dual fluorophore staining using both Oxazine 4 and Nile Red to highlight nerve and adipose tissue, respectively (**Fig. 3.9B**). Nerve-specific fluorescence was observed using Oxazine 4 administered either directly or systemically in the hypogastric nerve. However, only direct administration of Oxazine 4 created sufficient contrast in the aortic plexus for visualization (**Figs. 3.9A and 3.9B**). Direct administration of either Oxazine 4 alone or in combination with Nile Red provided equivalent N/M, A/M and A/N ratios to systemic administration

(**Fig. 3.9C**). Interestingly, the N/M ratio was not significantly different from the control blank co-solvent administered group (**Fig. 3.9C**) for either the direct or systemically administered fluorophore groups. This relatively low N/M ratio resulted for different reasons in the directly and systemically administered groups. In the direct administration group, there was visible nerve-specific fluorescence and relatively high nonspecific muscle signal following Oxazine 4 staining, which decreased the overall N/M ratio. In the systemic administration group, the low N/M ratio was the result of relatively low overall signal in both the nerve and muscle tissues (**Fig. 3.9A**). This difference in fluorescence intensity between the direct and systemic administration groups was demonstrated by both the difference in exposure times (10 ms for direct vs. 150 ms for systemic administration) as well as the inability to visualize the aortic plexus, the smaller of the two stained autonomic nerve sites (**Figs. 3.9A and 3.9B**).

Notably, the N/A ratio was significantly higher for the direct administration group as compared to the systemic administration group ($p=0.0082$ for Oxazine 4 alone, $p=0.014$ for Oxazine 4 and Nile Red dual staining, **Fig. 3.9C**). Nerve to adipose contrast is of critical importance for visualization of the NVB during nerve sparing radical prostatectomy, since this nerve tissue is embedded in a fibrofatty plate in humans.[136, 137] The N/A ratios generated using Oxazine 4 alone or in combination with Nile Red have the potential to facilitate intraoperative NVB visualization. This was further demonstrated using the direct administration technique on the aortic plexus and hypogastric nerves, which were stained using the direct administration methodology *in vivo* and then resected with their surrounding tissues to show their proximity to the prostate (**Fig. 3.9D**). During radical nerve sparing prostatectomy, the tissue pedicles containing the NVB are isolated from the prostate and surrounding fascia [138], modeled by the visual isolation shown in **Fig. 3.9D**, where the hypogastric nerve as well as the smaller aortic plexuses were readily visible above any background tissue staining. Additionally, due to the size of these nerves, visualization using conventional white light illumination was challenging (**Fig. 3.9D**), similar to visualization of the NVB during prostatectomy.[54, 129]

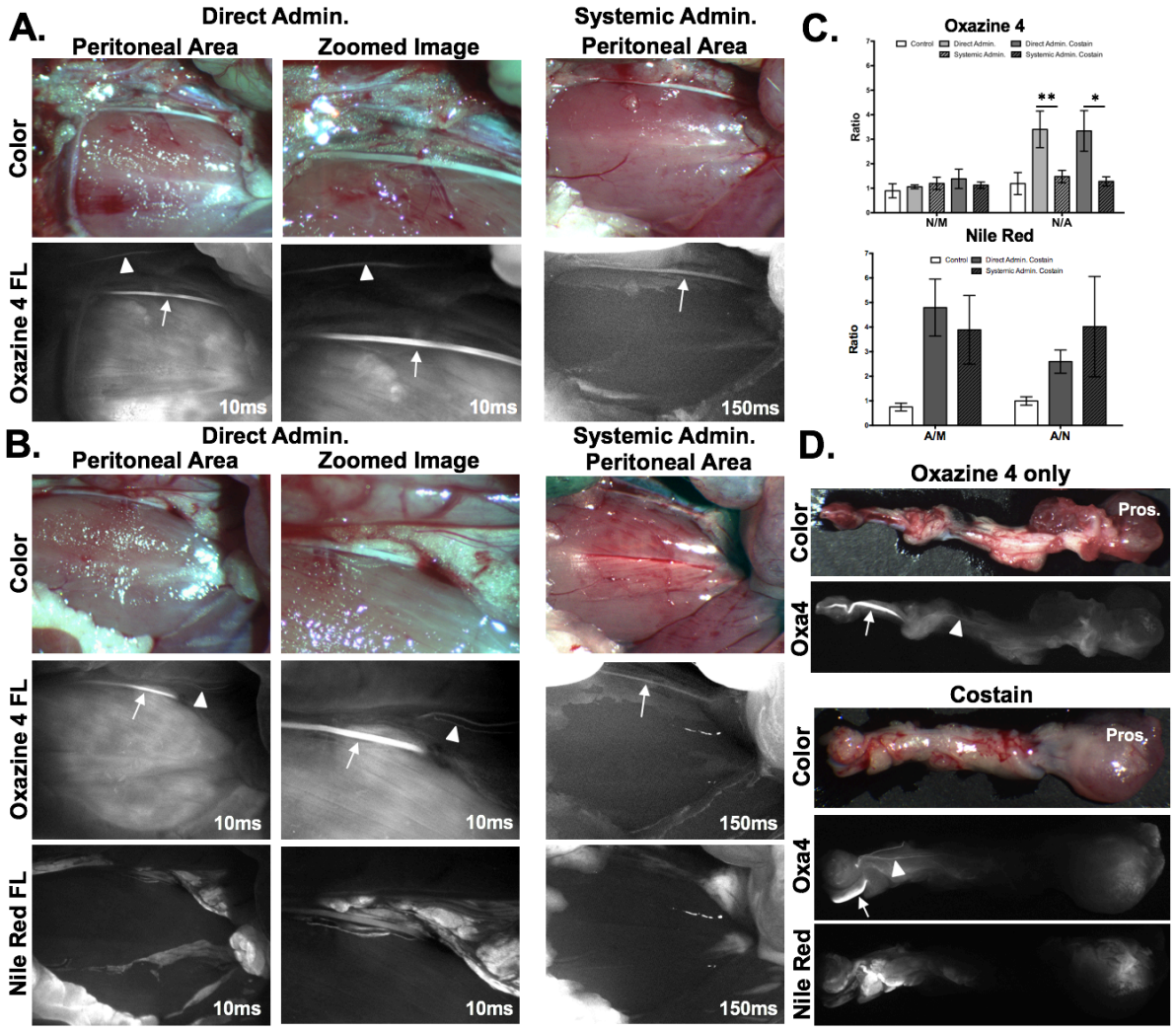

Figure 3.9: *Direct administration vs. systemic administration: comparison and assessment of clinical viability in rat autonomic nerve models.* Representative color and fluorescence images for **(A)** individual Oxazine 4 or **(B)** dual fluorophore stained rat hyogastric and aortic plexus nerve sites for direct and systemic administration methods are shown. All images are representative of data collected for n=4 nerve sites either 30 min following the final flush step for direct administration or 4 hrs following intravenous injection for systemic administration. **(C)** The nerve and adipose to background tissue ratios were determined using region of interest analysis on images collected at the same time intervals for direct and systemic administration methods. **(D)** The stained nerve and surrounding adipose tissue was resected along with the prostate with representative images displayed. In the Oxazine 4 fluorescence images the arrows depicts the stained hypogastric nerve, while the arrowhead shows the stained aortic plexus. All quantified data is presented as mean +/- standard deviation. FL = fluorescence, N/M = nerve to muscle ratio, N/CM = nerve to cut muscle ratio, N/A = nerve to adipose ratio, A/M = adipose to muscle ratio, A/CM = adipose to cut muscle ratio, A/N = adipose to nerve ratio. * = p value < 0.05, ** = p value < 0.01.

To show the utility of fluorescence image-guided surgery in a surgically relevant example of nerve-sparing prostatectomy, varying amounts of blood were placed on top of the stained hypogastric nerve tissue to simulate light and heavy bleeding that can occur during a prostatectomy procedure. Even in the presence of substantial blood cover the nerve tissue, the nerve-specific fluorescence was still clearly visible and easily discernable from the surrounding tissue (**Fig. 3.10A**). For confirmation that the direct administration methodology would highlight prostate innervation, the prostate was stained *in vivo* along with the hypogastric nerve and aortic plexus (Fig **3.10B**). Upon resection and imaging, the hypogastric nerve and the nerve tissue closely associated with the prostate were clearly visible via Oxazine 4 fluorescence, although difficult to identify under white light illumination due to the nerve's small size and bleeding that had occurred in the surrounding tissue. The merged fluorescence and color image demonstrated how the fluorescence signal could be overlaid onto a color video image for rapid nerve identification intraoperatively (**Fig. 3.10B**). Histological confirmation of the hypogastric nerve tissue was performed using tissue sections of resected nerve and surrounding muscle tissue that had been stained *in vivo* using the direct administration methodology (**Fig. 3.10C**). H&E, NeuroTrace, and FluoroMyelin staining was used to confirm the morphology and examine the nerve specific fluorescence microscopically. NeuroTrace and FluoroMyelin are fluorescent stains specific for Nissl substance and myelin, respectively, both of which are abundant in neuronal cells. H&E staining provided clear identification of the nerve from the surrounding muscle tissue and the Oxazine 4 fluorescence signal correlated with both nerve-specific fluorescence stains, confirming the fluorophore's specificity for nerve tissue and providing histological confirmation of the hypogastric nerve.

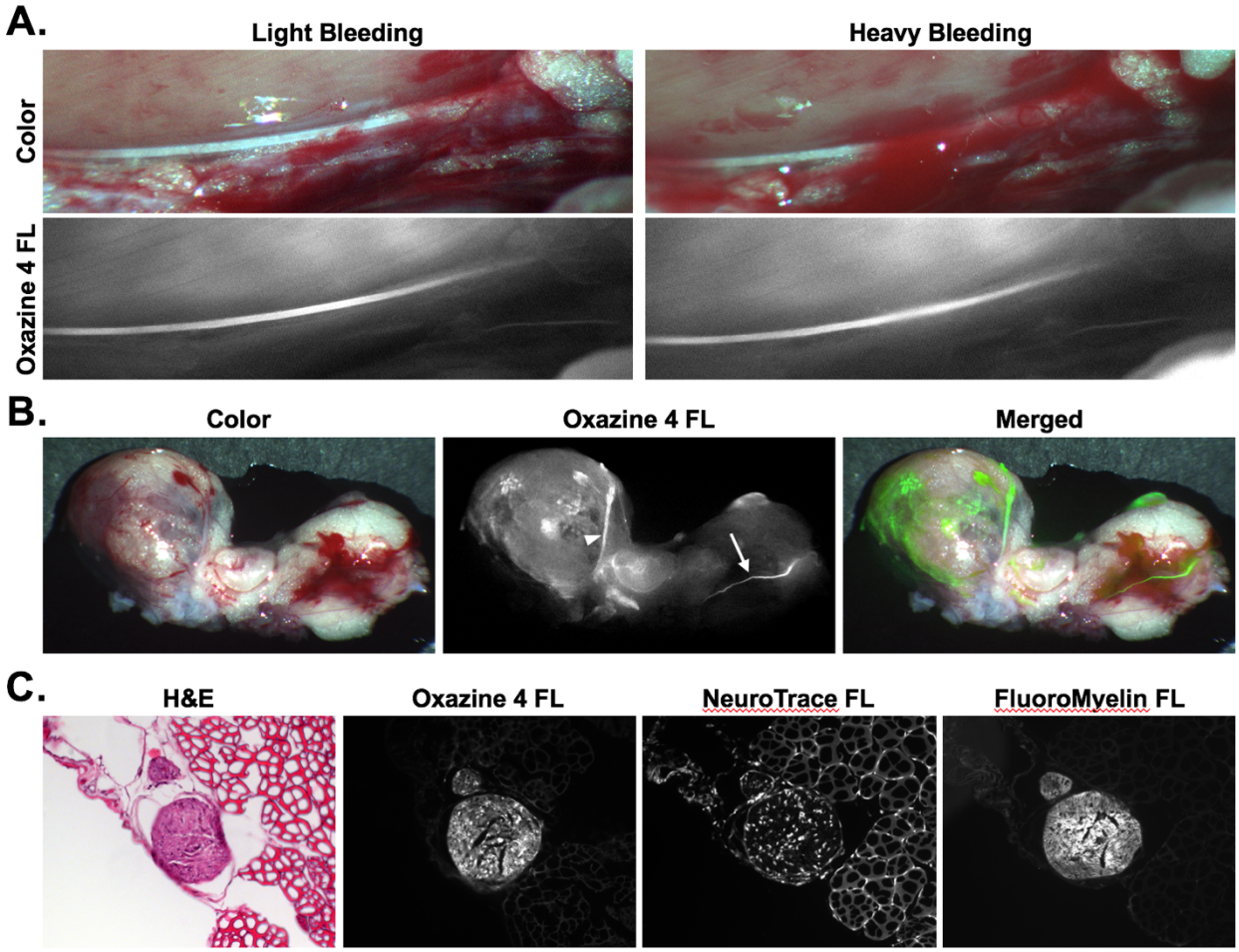

Figure 3.10: *Rat hypogastric and prostate autonomic direct administration nerve staining with bleeding and histological confirmation.* **(A)** Color and fluorescence images for Oxazine 4 stained rat hypogastric and aortic plexus nerve sites with varying degrees of blood over the nerve tissue are shown. All images were collected 30 min following the final flush step of the direct administration procedure. **(B)** Color, fluorescence, and merged fluorescence images for resected rat prostate and hypogastric nerve tissue stained *in vivo* with Oxazine 4 are shown. The tissue was resected and imaged following euthanasia 30 min after the final flush step of the direct administration procedure. In the Oxazine 4 fluorescence images the arrows depicts the stained hypogastric nerve, while the arrowhead shows the stained prostate nerve tissue. **(C)** Histological confirmation of rat hypogastric nerve tissue stained *in vivo* by direct administration of Oxazine 4 is shown with H&E, NeuroTrace, and FluoroMyelin staining. H&E, Oxazine 4 fluorescence, and NeuroTrace/Fluoromyelin costain fluorescence images were acquired from three serial sections of rat hypogastric nerve tissue and adjacent muscle tissue. FL = fluorescence.

DISCUSSION

The primary goal of radical prostatectomy is prostate cancer cure; however, preserving the nerves surrounding the prostate is crucial for post-surgical quality of life. Although nerve-sparing methods have been practiced for decades,[126] nerve identification using current visualization techniques continues to leave patients with nerve damage following radical prostatectomy.[6, 14, 127, 128] Fluorescence guided surgery offers a potential solution, providing the ability to enhance nerve visualization with specific contrast in real time, where several classes of small molecule fluorophores have shown nerve specificity following systemic administration in preclinical models.[20, 64-74] The prostate is highly innervated and all nerve tissue cannot be spared, but preservation of the cavernous nerves has been shown to be sufficient for maintenance of continence and potency post prostatectomy.[61, 62] Systemic administration of a nerve specific fluorophore would highlight all nerve tissue in and around the prostate leading to high background fluorescence and diminished cavernous nerve SBR, hindering the surgeon's ability to identify and visualize the vital nerve structures. Additionally, the candidate nerve-specific contrast agent used herein, Oxazine 4, shows significant renal clearance, accumulating in the urine (**Fig. 3.8**) creating increased background fluorescence for prostatectomy following systemic administration.

A direct administration methodology has been developed that allows for selective nerve labeling as a clinically viable method for enhancing visualization of the cavernous nerves during nerve sparing prostatectomy. Application of the fluorophores directly to the tissue pedicles containing the vital nerve structures would allow cavernous nerve visualization without diminishing the SBR by highlighting all nerves surrounding the prostate. This methodology overcame the non-specific binding that occurred upon direct tissue administration of fluorophores through systematic optimization of the dose, incubation and washing of Oxazine 4 fluorescence in murine model nerve tissues. The resulting nerve to background tissue contrast utilizing the final direct administration methodology was demonstrated to be equivalent or better than systemic administration in peripheral mouse nerves (**Fig. 3.7**) and autonomic rat nerves (**Fig. 3.9)**. Further, by utilizing flush type washing and PBS as the sole washing solution, the direct administration protocol can be completed within 15 minutes, making it viable for nerve sparing prostatectomy and

compatible with current clinical methodology (**Fig. 3.6 and Table 3.1**). Direct administration of Oxazine 4 would provide peak nerve contrast for the entirety of the nerve sparing procedure, with nerve to background tissue ratios increasing for up to 30 min following completion of the staining procedure due to clearance of nonspecific fluorophore from surrounding muscle and adipose tissues (**Figs. 3.7D and 3.7E**).

A significantly lower Oxazine 4 dose was required to provide equivalent nerve contrast using the direct administration methodology as compared to systemic administration (**Figs. 3.7 and 3.9**), where lower doses decreased the nonspecific tissue fluorescence and improved nerve to background tissue ratios (**Fig. 3.2**). Overall, direct administration required 16x less dose at 4.95 μg/nerve site as compared to 79.2 μg for systemic administration in murine models (**Table 3.1**). Even the use of two doses of Oxazine 4 to highlight both cavernous nerves during a nerve-sparing prostatectomy would still result in an 8x lower dose to the patient than systemic administration. This drastic decrease in the required dose has the potential to facilitate clinical translation of nerve-specific fluorophores. Systemic toxicity would be minimized using the direct administration methodology, posing less concern for blood nerve and blood brain barrier fluorophore penetration and accumulation. When the selected Oxazine 4 dose was scaled from mouse to humans by body surface area,[151] the resulting 59.38 μg direct administration dose falls within the Food and Drug Administration (FDA) "microdose" range (≤100 μg), allowing for clinical studies to be performed under exploratory investigational new drug (IND) guidelines without prior clinical safety studies,[150] a significant financial consideration for any agent administered in clinical trials.

Another key benefit of direct administration over systemic administration was the order of magnitude increase in fluorescence signal intensity observed, where nerve fluorescence was readily visualized with 10 ms exposure times following direct administration in both murine and rat models. This provided average nerve tissue fluorescence intensity 8x greater than systemic administration, which required at least 150 ms for visualization. Subsequently, direct administration afforded significantly higher nerve to background tissue ratios than systemic administration at video rate exposure times (**Figs. 3.7 and 3.9**). The required exposure time following systemic administration was ~3x times that of video rate refresh rate, resulting in either increased time for the nerve-sparing procedure or lack of adoption due to inability to be seamlessly integrated into existing surgical workflow. Direct

administration also enabled visualization of finer nerve branches and smaller adipose deposits than systemic administration (**Figs. 3.7 and 3.9**). Direct administration could thus enhance visibility of the delicate structures associated with the cavernous nerve for a more complete nerve sparing procedure.

Since the NVB is embedded in fatty tissue[136, 137] and many nerve specific small molecule fluorophores have been plagued with non-specific adipose accumulation due to the molecular lipophilicity,[20, 66, 68, 69] we developed a dual fluorophore staining method using spectrally-distinct, adipose and nerve-specific fluorophores. Nile Red, which emits orange fluorescence, was chosen as the adipose specific fluorophore for its strong adipose specificity and spectral separation from Oxazine 4.[140-144] Co-staining tissue with both fluorophores enabled image post processing to improve the N/A contrast (**Fig. 3.3**). Such image processing could be performed in real time to provide enhanced tissue separation intraoperatively using clinically available fluorescence imaging systems with dual color functionality, such as the FLARE imaging system.[15, 17, 20, 130, 131] Interestingly, the chosen dual fluorophore tissue staining method provided higher nerve to background tissue ratios than Oxazine 4 staining alone (**Fig. 3.3**), where nerve tissue contrast was highest when a serial co-staining technique was used beginning with Oxazine 4 followed by Nile Red. This co-stain technique would be best for clinical nerve-specific visualization because in addition to providing the highest nerve and adipose contrast, it facilitates application of nerve specific contrast first to assess if dual fluorophore tissue staining would be necessary prior to application of the adipose specific fluorophore. The improvement in the nerve to background tissue contrast with the dual fluorophore staining techniques was a result of incubation with co-solvent formulation containing Nile Red, which removed nonspecific Oxazine 4 fluorophore effectively lowering background fluorescence. Therefore, utilization of the dual fluorophore staining method did not lengthen the direct administration procedure, as the Nile Red incubation served to both stain the adipose tissue and remove non-specific Oxazine 4 fluorescence (**Figs. 3.7D and 3.7E**). Similar to Oxazine 4 direct administration, Nile Red direct administration required a much lower dose than systemic administration to obtain equivalent adipose to background tissue contrast, while yielding a higher intensity signal and more detailed adipose tissue fluorescence images (**Fig. 3.7B**).

Tissue-specific fluorescence intensity was measured in the Nile Red and Oxazine 4 channels following individual and dual fluorophore tissue staining to

confirm that Nile Red fluorescence was spectrally separated from Oxazine 4 fluorescence *in vivo*. (**Fig. 3.4**). While Oxazine 4 fluorescence showed some cross talk into the Nile Red fluorescence channel, Nile Red fluorescence did not cross talk into the Oxazine 4 fluorescence channel and thus did not affect the nerve to background tissue contrast. Therefore, Nile Red was not only compatible with Oxazine 4 for nerve and adipose differentiation, but would also have utility as an adipose tissue counterstain for use in dual fluorophore staining with a further red shifted or NIR nerve-specific fluorophore. Of note, the mechanisms for nerve and adipose tissue contrast generation using Oxazine 4 and Nile Red respectively were distinct. Oxazine 4 nerve contrast was increased by the removal of non-specific tissue fluorescence through adequate washing, while Nile Red adipose contrast was increased by obtaining the highest adipose specific accumulation of the fluorophore, requiring less washing to obtain the highest degree of adipose staining (**Fig. 3.4**). These observations support the selected Oxa4/NR serial dual staining strategy, where Oxazine 4 staining was enhanced by incubation with Nile Red in co-solvent, while Nile Red adipose-specific fluorescence required less washing. The difference in nonspecific tissue fluorescence between the two fluorophores can likely be attributed to the fluorogenic properties of Nile Red. Nile Red is quenched in a primarily aqueous environment and brightly fluorescent in hydrophobic, lipid rich environments, making lipid poor tissue such as muscle have inherently low Nile Red fluorescence signal, reducing the need to remove nonspecific Nile Red accumulation through washing.[142]

The direct administration method using Oxazine 4 alone and in combination with Nile Red was scaled to rat imaging studies to facilitate imaging of surgically available autonomic nerves that were in close anatomical proximity to the prostate with similar composition to the cavernous nerves.[139, 146, 152] The aortic plexus and hypogastric nerves were selected for direct administration studies where the hypogastric nerves were larger and more easily visualized than the aortic plexuses. Direct and systemic administration were compared using the chosen dose scaled by body surface area from murine studies. The N/M, A/M, and A/N ratios were found to be equivalent for the direct and systemically administered groups. The N/A ratios were significantly higher for direct administration as compared to systemic administration groups (**Fig. 3.9**). Unlike the murine nerve imaging studies, the N/M ratio in the rat studies was similar to control, no fluorophore administered animals. However, when the images were examined significant nerve fluorescence was

visible in the rat autonomic nerves (**Figs. 3.9A and 3.9B**). The low N/M ratio likely stemmed from increased muscle background fluorescence in the peritoneal area for the direct administration group, while in the systemic administration group overall fluorescence signal was low in the nerve resulting in a low N/M ratio. The increase in background muscle fluorescence was unexpected and additional formulation strategies are being investigated to decrease nonspecific accumulation in muscle tissue. The utility of the direct administration method for radical nerve-sparing prostatectomy was highlighted by the N/A ratio which is vital to the success of this technique since the NVB is embedded in adipose tissue. Additionally, during radical nerve-sparing prostatectomy tissue pedicles containing the NVB are isolated from the prostate, which largely contain adipose tissue. Direct administration of nerve contrast to these tissue pedicles has the potential to provide the desired contrast to specifically illuminate the cavernous nerves. This possibility was highlighted by resecting the stained autonomic nerves along with the rat prostate where white light visualization of these small nerve structures was difficult, but fluorescence imaging readily detected both the hypogastric nerve as well as the much smaller aortic plexus (**Fig. 3.9D**). Further, direct innervation of the prostate was readily visible alongside hypogastric nerve fluorescence in prostate tissue stained via direct administration (**Fig. 3.10B**). Microscopic evaluation of hypogastric nerve tissue stained via direct administration *in vivo* provided histological confirmation for the nerve specific fluorescence signal (**Fig. 3.10C**). Importantly, Oxazine 4 signal showed positive correlation with other *ex vivo* nerve specific fluorescence stains including FluoroMyelin and NeuroTrace. The possibility to highlight nerve structures intraoperatively using the direct administration methodology was further demonstrated by visualizing nerve specific fluorescence signal through varying amounts of blood (**Fig. 3.10A**). Although monitored closely, heavy bleeding can occur during a prostatectomy procedure,[153] which can interfere with visible fluorescence signals because of hemoglobin's light absorption characteristics.[24] However, the absorption and emission of Oxazine 4 are sufficiently red shifted negating any effect on fluorescence intensity in the presence of blood. Additional fluorophore development of NIR nerve-specific fluorophores would further negate any fluorescence changes in the presence of blood during surgery.

The characterized and validated direct administration methodology provided selective nerve highlighting for fluorescence-guided nerve sparing prostatectomy, with at least equivalent contrast to the previously utilized systemic administration

method while yielding a significantly higher intensity signal at an order of magnitude lower dose. In addition, the dual fluorophore staining technique developed here sets the stage for improving nerve specific contrast with spectrally distinct targeted background tissue fluorescence. Further studies are underway to translate these findings towards clinical trials including tissue depth penetration studies following direct fluorophore administration and the utility of improved formulation strategies to diminish background fluorophore uptake such as micellar encapsulation, which has demonstrated improved nerve-specificity in systemically administered models.[112] Direct administration of nerve-specific contrast has the potential to improve nerve identification and visualization during radical nerve-sparing prostatectomy through specific labeling of the vital nerve structures in a highly innervated organ. Of specific note, the validated direct administration methodology falls within the microdosing range facilitating clinical trials through an eIND, something not possible using systemically administered nerve contrast. The developed direct administration strategy could also highlight vital nervous structures in a variety of other surgical procedures such as retroperitoneal lymph node dissection for testicular cancer, radical pelvic gastrointestinal or gynecologic surgery, and radial neck dissection, potentially improving post-surgical quality of life for numerous surgically treated diseases.

Chapter 4

Oxazine fluorophore derivative library screening and near-infrared nerve-specific probe identification

ABSTRACT

Nerve damage remains a major problem during surgery, affecting up to 63 million patients annually worldwide. Surgeons mainly rely on knowledge of neuroanatomy and conventional white light visualization to identify nerves intraoperatively. Fluorescence guided surgery (FGS) has the potential to revolutionize surgery by allowing direct visualization of targeted tissues like nerves intraoperatively. FGS in the near-infrared (NIR) window enables wide-field, real-time visualization of specifically highlighted tissues with high specificity and sensitivity at millimeter to centimeter depths. Several classes of nerve-specific small molecule fluorophores have been studied preclinically for FGS, however none exhibit peripheral nerve specificity and NIR fluorescence, leaving an unmet need for a viable NIR nerve contrast agent for clinical translation. We have developed and screened a library of 66 novel oxazine fluorophore derivates based on the promising Oxazine 4 fluorophore and identified several NIR fluorophores that exhibit high nerve specificity following both direct and systemic administration in mice. Additionally, the top candidate from the library, LGW01-08, demonstrated excellent nerve specific contrast in large animal screening studies, enabling the visualization of buried nerve tissue invisible in white light illumination. The library of oxazine derivatives and screening data presented herein provide useful information in determining the factors important for nerve-specificity of small molecules and the identification of a NIR nerve specific fluorophore that fills the gap for a candidate nerve-specific probe for use in clinical FGS.

INTRODUCTION

The utility of fluorescence guided surgery (FGS) has been demonstrated in numerous clinical and preclinical applications. A variety of FGS imaging systems are available for clinical use including the FLARE (Curadel Marlborough, MA),[15-20] Fluobeam 800 (Fluoptics Imaging Inc., Cambridge, MA),[21] Photodynamic eye (Hamamatsu Photonics, Hamamatsu, Japan),[22] HyperEye Medical System (Mizuho Medical Company, Tokyo, Japan),[23] and Firefly fluorescence-imaging channel in the da Vinci surgical robot (Intuitive Surgical, Inc., Sunnyvale, CA). These systems mainly operate in the near-infrared (NIR) wavelengths (650-900 nm), where tissue chromophore absorbance, autofluorescence and scattering are all at local minima, allowing for tissue to be highlighted and visualized at centimeter depths against a black background.[24, 25] However, only two NIR fluorescent dyes are approved for clinical FGS; methylene blue and indocyanine green, both of which are blood pool agents with no specific tissue targeting.[25] Development and clinical translation of tissue and disease targeted fluorescence probes would greatly increase the impact of FGS, expanding its application to an array of surgical procedures to improve tissue resection and sparing outcomes.

One such tissue-specific FGS probe is a nerve-specific fluorophore, which could have a profound impact on overall surgical outcomes and post-surgical complications. Surgery is performed commonly in the United States with approximately 40 million operations annually, incurring up to 600,000 iatrogenic nerve injuries.[154] Iatrogenic nerve injury is a major source of morbidity that occurs across all surgical specialties including general, thoracic, cardiac, urologic, plastic, colorectal, spinal, neuro-, vascular and otolaryngologic and orthopedic surgery.[155] Unlike other critical tissues, such as blood vessels, nerve injuries cannot be repaired with reliable functional improvement.[156] Therefore iatrogenic nerve injury is often permanent and, in the setting of peripheral nerve injury, leads to disabled motor and protective sensory function that can limit patients' ability to work and participate in activities of daily living, and disposes them to injury. Thus, nerve injury prevention strategies are the only known method of successfully counteracting iatrogenic peripheral nerve injury.[156] Notably, there is no clinically approved technology to enhance a surgeons' visual recognition of nerve tissue during surgery. Surgeons still

rely mainly on knowledge of neuroanatomy and conventional white light visualization to identify nerves intraoperatively.

Experienced surgeons have little difficulty identifying major nerves under the circumstances of normal anatomy and routine, uncomplicated surgical approaches. Nerve identification can become challenging, however, in situations where the normal location, appearance, or physical properties of patient tissues are changed. Conditions where nerve characteristics are altered in the surgical setting are common and may occur with acute or prior trauma, tumors, prior surgery, congenital anomalies, and radiation therapy. Minimally invasive surgical techniques also put peripheral nerves at higher risk because these procedures rely on assumptions about anatomical landmarks, rather than on direct visual identification of these important structures during the dissection process. Other important peripheral nerves, such as the delicate cavernous nerves responsible for continence and potency in men—often injured during prostatectomy—are so small that they are difficult to recognize even under surgical camera magnification.[157] Therefore, the ability to distinctly and visually label important peripheral nerves during the dissection process would enable surgeons to identify and safeguard these vital structures. Nerve stimulation and several imaging modalities have been employed to aid in the identification of nerve tissue including ultrasound, optical coherence tomography, and confocal endomicroscopy.[55-60] However, these lack specificity, resolution, and wide-field imaging functionality, making it difficult to identify nerve tissues in real time during surgery. Recent development of nerve targeting agents for FGS has shown promise for providing wide field, real time nerve identification and advancements in administration techniques have improved clinical viability of these promising probes (**Chapter 3**).

Several classes of nerve specific small molecule fluorophores have been demonstrated preclinically, including stilbene derivatives,[64] a coumarin analog,[65] distyrylbenzene derivatives,[20, 66-70] styryl pyridinium fluorophores,[71, 72] a tricarbocyanine fluorophore,[73] and an oxazine fluorophore.[63, 74] However, no NIR nerve-specific fluorophore exists, requiring further directed fluorophore design and development to obtain a candidate for clinical translation. Of the six classes of nerve-specific fluorophores, the oxazine fluorophore, Oxazine 4, is the most promising candidate for further development, as it shows both high peripheral nerve-specificity and red shifted absorption and emission spectra.[74] However, shifting the excitation and emission of this fluorophore into the NIR range is particularly challenging

because nerve-specific contrast agents must have a relatively low molecular weight to cross the blood-nerve barrier (BNB);[20, 158, 159] however, fluorophores must have a sufficient number of double bonds to reach NIR wavelengths, thereby increasing their molecule weight.[130] Due to these constraints, the small molecule must act as both the nerve binding agent and the fluorophore, making synthetic optimization challenging. In these studies, we have built a library of Oxazine-based fluorophores designed to combine the NIR fluorescence profile of Oxazine 1 and the nerve-binding properties of Oxazine 4.[74] Oxazine 1 has desirable red-shifted excitation and emission wavelengths but shows pan-tissue fluorescence following local or systemic administration. Conversely, Oxazine 4 demonstrates exquisite nerve specificity following both systemic and local administration with excitation and emission wavelength maxima shorter than NIR. Through purposeful structural modifications of these two compounds, we have created a library of 66 novel Oxazine fluorophore derivatives that we screened for NIR optical properties and nerve-specificity following systemic and local administration with the goals of defining the factors that modulate a fluorophore's nerve specificity and identifying NIR candidate(s) for clinical translation.

MATERIALS & METHODS

Oxazine derivative library

Oxazine 4 perchlorate and Oxazine 1 perchlorate were obtained from Exciton (Lockbourne, OH). The remaining 64 oxazine derivatives were synthesized in the Gibbs laboratory by Dr. Lei Wang. All synthesis, purification, and characterization of the oxazine derivatives was carried out by Dr. Wang at the OHSU and PSU campuses. All reagents were purchased from Sigma Aldrich, Fisher Scientific, TCI, or Ark Pharm. Unless otherwise indicated, all commercially available starting materials were used directly without further purification. Analytical thin layer chromatography (TLC) was performed on Millipore ready-to-use plates with silica gel 60 (F254, 32-63 μm). Flash chromatography was performed on Sorbent Technologies silica gel for column chromatography or on a Biotage Isolera Flash System using SNAP Ultra cartridges. High-resolution mass spectra (HRMS) were measured on a ThermoElectron LTQ-Orbitrap high resolution mass spectrometer

with a dedicated Accela HPLC system, or an Agilent 6244 time-of-flight LCMS with diode array detector VL+. All oxazine derivatives were solubilized in PBS, pH 7.4 with 10% DMSO for optical and physiochemical property measurements. To solubilize all fluorophores for *in vivo* use a co-solvent formulation containing 10% dimethyl sulfoxide (DMSO), 5% Kolliphor EL, 65% serum, and 20% phosphate buffered saline (PBS) was used.[20]

LCMS and purity characterization

Mass-to-charge ratio and purity of the oxazine derivatives were characterized on an Agilent 6244 time-of-flight LCMS with diode array detector VL+. The Oxazine sample (10 μL) was injected into a C18 column (Poroshell 120, 4.6 × 50 mm, 2.7 micron), and eluted with a solvent system of A (H_2O, 0.1% FA) and B (MeCN, 01.% FA) at 0.4 mL/min, from A/B = 90/10 to 5/95 over 10 min, maintained at A/B = 5/95 for additional 5 min. Ions were detected in positive ion mode by setting the capillary voltage at 4 kV and gas temperature at 350° C. Purity was calculated through area under the curve analysis of the absorbance at 254 nm.

Absorption and fluorescence spectroscopy

Absorbance spectra were collected in 10% DMSO in PBS with a Cary 50 UV-Vis spectrophotometer at room temperature, using a 1-cm quartz cuvette. Fluorescence spectra were collected on a Cary Eclipse fluorescence spectrophotometer at room temperature, using a 1-cm quartz cuvette (Agilent Technologies). All absorbance spectra were reference corrected. Extinction coefficients for all oxazine derivatives were calculated from Beer's Law plots of absorbance versus concentration. Fluorescence spectra were corrected for the wavelength dependent response of the R928 photomultiplier tube using a manufacturer generated correction file. Relative quantum yields were reported as the average of multiple measurements using multiple references, including Oxazine 1 and Oxazine 170. Excitation emission matrices (EEMs) were collected over various spectral regions, using 5-nm step sizes for emission and 10-nm step sizes for excitation. The band pass for excitation and emission was 5 to 10 nm.

Physicochemical property calculation

Physicochemical partition coefficients (Log D) values at pH 7.4, number of hydrogen bond donors and acceptors, polar surface area, and the number of rotatable bonds were calculated using Marvin and JChem calculator plugins (ChemAxon, Budapest, Hungary).

Animals

Approval for the use of all animals in this study was obtained from the Institutional Animal Care and Use Committee (IACUC) at Oregon Health and Science University (OHSU). Male CD-1 mice weighing 22-24g were purchased from Charles River Laboratories (Wilmington, MA). Prior to surgery, animals were anaesthetized with 100 mg/kg ketamine and 10 mg/kg xylazine (Patterson Veterinary, Devens, MA) administered intraperitoneally (IP). The brachial plexus and sciatic nerves were surgically exposed by removal of overlaying adipose and muscle tissues for direct nerve staining and imaging.

In vivo nerve-specificity screening

Each compound was screened for its tissue-specificity using a previously published direct administration strategy in murine brachial plexus and sciatic nerves (**Chapter 3**). Each compound from the oxazine derivative library was formulated at 125 μM in the co-solvent formulation. 100 μL of the formulated oxazine fluorophore were incubated on the exposed brachial plexus or sciatic nerve for 5 minutes. The fluorophore containing solution was removed and the area was irrigated with saline 18 times to remove any unbound fluorophore. Images were acquired 30 minutes following completion of staining. Unstained nerve sites were used for all control images (n=3 mice or 6 nerve sites/fluorophore).

Each compound was also screened for its tissue-specificity following systemic administration per the kinetics and dose determined for Oxazine 4.[63, 74] 200 nmol of each compound in 100 μL of co-solvent formulation was administered intravenously. Intravenous administration was performed 4 hours prior to imaging, which has been shown previously to provide the highest nerve to background tissue fluorescence for Oxazine 4 and several other nerve specific fluorophores.[20, 66, 74]

Uninjected animals were used for all control images (n=3 mice or 12 nerve sites/dye).

Intraoperative fluorescence imaging system

A custom-built small animal imaging system capable of real-time color and fluorescence imaging was used to acquire rodent *in vivo* images. The imaging system consisted of a QImaging EXi Blue monochrome camera (Surrey, British Columbia, CA) for fluorescence detection with a removable Bayer filter for collecting co-registered color and fluorescence images. A PhotoFluor II light source (89 North, Burlington, VT) was focused onto the surgical field through a liquid light guide and used unfiltered for white light illumination. For fluorescence excitation, the PhotoFluor II was filtered with a 620 ± 30 nm bandpass excitation filter. Resulting fluorescence was collected with a 700 ± 37.5 nm bandpass emission filter for image collection. All filters were obtained from Chroma Technology (Bellows Falls, VT). Camera exposure times ranged from 5 – 2000 ms for fluorescence image collection.

A custom-built laparoscopic imaging system also capable of real-time color and fluorescence imaging was used to acquire swine *in vivo* images. The imaging system was integrated into the da Vinci Si surgical system from Intuitive Surgical, Inc. (Sunnyvale, CA) and consisted of a Necsel Neon 5W 640nm laser (Necsel, Milpitas, CA) coupled to the da Vinci Si endoscope with a Semrock 642 nm StopLine single-notch blocking filter (Semrock, Rochester NY) to remove excitation light from the acquired fluorescence image. The 642 nm StopLine blocking filter was placed in the Si camera sterile adaptor between the rod lens endoscope and the Si camera head. Fluorescent signal acquisition occurred in the Si white light mode with the blocking filter removing the 642 nm excitation light and the fluorescent signal detected primarily on the RGB red-Bayer elements. Laser power at the endoscope tip measured 800mW with optical power loses occurring primarily at the laser fiber/light guide and the Si camera head/rod lens interfaces. Fluorescence and color videos were captured using the Si Vision Side Cart at an exposure time of 2 ms. Images were taken from screen captures of the *in vivo* video clips. Videos were recorded on a Panasonic SDI recorder connected to the TilePro video out connections on da Vinci Si Vision Side Cart.

Intraoperative nerve imaging and image analysis

Nerve specific contrast was assessed for all oxazine derivative library screening studies using the intraoperative fluorescence imaging system to collect images of the nerves and surrounding tissues. For direct administration studies, images were collected after the final wash step and 30 min after the completion of the final wash step to observe any changes in the signal to background ratio (SBR) that occurred following completion of staining. For systemic administration screening studies, the brachial plexus and sciatic nerves were exposed and images were collected for each mouse 4 hours post injection. Additional unstained control animals were imaged to assess tissue autofluorescence.

Custom written MatLab code was used to analyze the tissue specific fluorescence where regions of interest were selected on the nerve, muscle and adipose tissue using the white light images, but blinded to the fluorescence images. These regions of interest were then analyzed on the co-registered, matched fluorescence images permitting assessment of the mean tissue intensities and nerve to muscle (N/M), nerve to cut muscle (N/CM) and nerve to adipose (N/A) ratios. Intensity measurements were divided by the exposure time to obtain normalized intensity per second measurements. Mean nerve to background tissue ratios (N/M, N/CM, N/A) were calculated for each oxazine derivative. No cut muscle tissue was analyzed for the systemic administration studies.

Statistical analysis

Significant differences between nerve SBR means were evaluated using a one-way ANOVA followed by a Fisher's LSD multiple comparison test with no assumption of sphericity using the Geisser-Greenhouse correction to compare all mean nerve to background tissue ratios. The α value was set to 0.05 for all analyses. Results were presented as mean ± standard deviation (S.D.). All statistical analysis was performed using GraphPad Prism (La Jolla, CA).

RESULTS

Oxazine derivative library optical and physicochemical property characterization

A library of 66 oxazine fluorophore derivatives were synthesized as structural variants of Oxazine 4 and Oxazine 1, which have demonstrated strong nerve-specificity and pan tissue fluorescence, respectively. From the library of 66 oxazine fluorophores, 64 novel compounds plus Oxazine 4 and Oxazine 1, were characterized for their optical and physicochemical properties. The maximum absorbance and emission values ranged from 603 to 702 nm and 625 to 720 nm, respectively, resulting in 42 compounds with near-infrared (NIR) emission (**Table 4.1**). The extinction coefficient and quantum yield for each oxazine derivative were quantified and used to calculate fluorophore brightness, which varied from 0.05 to 39.28 (**Table 4.1**). Molecular properties of each oxazine derivative including molecular weight (MW), partition coefficient (LogD), number of hydrogen bond donors and acceptors, polar surface area (PSA), and number of rotatable bonds were calculated (**Table 4.2**). The MW of the oxazine library varied from 240.3 to 428.6 g/mol, LogD values varied from 2.59 to 7.21, number of hydrogen bond donors and acceptors varied from 0 to 2 and 3 to 5 respectively, number of rotatable bonds varied from 0 to 5, and polar surface area values varied from 27.84 to 73.2 $Å^2$.

Table 4.1.1: *Oxazine derivative library optical properties.*

Number	Compound ID	Max Abs (nm)	Max Ex (nm)	Max Em (nm)	Extinction coefficient ($M^{-1}cm^{-1}$)	Quantum yield (%)	Brightness ($M^{-1}cm^{-1}$)
1	Oxazine 1	655	660	671	93211	7.40	6.90
2	Oxazine 4	618	620	634	77156	38.37	29.61
3	LGW01-08	638	640	659	78650	5.68	4.47
4	LGW01-18	617	620	636	60731	32.91	19.99
5	LGW01-21	617	620	634	28745	30.12	8.66
6	LGW01-23	645	620	635	62445	0.67	0.42
7	LGW01-25	635	640	660	41771	3.31	1.38
8	LGW01-39	648	650	667	76144	9.56	7.28
9	LGW01-44	648	650	664	40124	21.63	8.68
10	LGW01-56	664	670	684	38832	11.68	4.53
11	LGW01-61	612	610	631	21783	40.27	8.77
12	LGW01-64	620	620	638	50166	42.15	21.15
13	LGW01-99	648	650	667	56046	10.14	5.68
14	LGW02-57	635	635	653	56713	11.15	6.32
15	LGW02-58	620	620	635	42685	25.26	10.78
16	LGW02-59	611	615	636	41229	31.74	13.09
17	LGW02-60	645	650	661	65369	8.98	5.87
18	LGW02-61	630	635	658	68548	6.12	4.20
19	LGW02-86	661	665	680	39472	13.18	5.20
20	LGW02-87	678	680	690	59937	15.03	9.01
21	LGW02-91	640	645	657	59971	23.58	14.14
22	LGW02-92	656	660	673	43659	9.27	4.05
23	LGW02-95	606	605	627	48653	32.50	15.81
24	LGW02-99	640	665	675	59971	24.67	14.80
25	LGW03-01	677	680	695	44453	17.27	7.68
26	LGW03-06	640	640	661	35942	11.94	4.29
27	LGW03-07	654	660	672	52356	9.28	4.86
28	LGW03-12	624	630	638	40041	27.22	10.90
29	LGW03-13	641	645	659	64045	6.49	4.16
30	LGW03-18	661	665	680	66206	3.49	2.31
31	LGW03-21	642	640	661	36049	2.25	0.81
32	LGW03-23	664	645	690	23099	1.53	0.35
33	LGW03-31	655	655	674	48226	15.78	7.61

*Abs: Absorbance; Ex: Excitation; Em: Emission

Table 4.1.2: *Oxazine derivative library optical properties.*

Number	Compound ID	Max Abs (nm)	Max Ex (nm)	Max Em (nm)	Extinction coefficient ($M^{-1}cm^{-1}$)	Quantum yield (%)	Brightness ($M^{-1}cm^{-1}$)
34	LGW03-32	631	630	644	45650	29.92	13.66
35	LGW03-37	646	650	670	48849	4.34	2.12
36	LGW03-41	607	625	641	19729	25.80	5.09
37	LGW03-52	678	680	699	38039	6.82	2.59
38	LGW03-57	661	665	680	54072	18.17	9.83
39	LGW03-65	629	630	643	28067	27.39	7.69
40	LGW03-76	654	655	669	66111	7.99	5.28
41	LGW03-88	631	640	659	59737	6.22	3.71
42	LGW04-31	641	640	661	59586	5.01	2.99
43	LGW04-32	620	620	638	61084	39.77	24.29
44	LGW04-36	636	635	657	60819	8.15	4.96
45	LGW04-81	616	615	634	52291	39.47	20.64
46	LGW04-84	637	640	658	50981	3.95	2.02
47	LGW04-91	663	665	689	85597	2.77	2.37
48	LGW05-33	638	640	660	36166	3.84	1.39
49	LGW05-39	620	620	638	18223	34.29	6.25
50	LGW05-42	612	615	636	41527	37.22	15.46
51	LGW05-65	661	665	684	61535	7.85	4.83
52	LGW05-66	701	710	718	34002	36.68	12.47
53	LGW05-73	657	660	676	55570	32.95	18.31
54	LGW05-75	638	640	659	57360	31.70	18.19
55	LGW05-76	628	630	650	45449	32.68	14.85
56	LGW05-81	611	610	632	58410	43.02	25.13
57	LGW05-82	636	640	661	36833	2.70	1.00
58	LGW05-84	643	650	675	46048	4.85	2.23
59	LGW05-85	613	615	640	45382	41.05	18.63
60	LGW05-91	606	610	626	16763	33.45	5.61
61	LGW06-10	602	605	621	55807	26.54	14.81
62	LGW06-11	628	625	650	31843	2.52	0.80
63	LGW06-14	590	590	606	39303	37.61	14.78
64	LGW06-97	599	600	617	38616	25.39	9.81
65	LGW07-55	619	620	634	20163	28.25	5.70
66	LGW07-59	649	655	665	51130	32.17	16.45

*Abs: Absorbance; Ex: Excitation; Em: Emission

Table 4.2.1: *Oxazine derivative library physiochemical properties.*

Number	Compound ID	Molecular weight	LogD (pH7.4)	Number of H bond donor/acceptor	Polar surface area	Number of Rotatable bonds
1	Oxazine 1	324.45	5.21	0/3	27.84	5
2	Oxazine 4	296.39	4.26	2/3	47.59	3
3	LGW01-08	310.42	4.73	1/3	36.63	4
4	LGW01-18	282.37	3.74	2/3	47.59	3
5	LGW01-21	268.34	3.23	2/3	47.59	3
6	LGW01-23	324.45	5.25	1/3	36.63	4
7	LGW01-25	296.39	4.22	1/3	36.63	4
8	LGW01-39	268.34	3.79	0/3	27.84	1
9	LGW01-44	334.44	4.74	2/3	47.59	2
10	LGW01-56	348.47	5.22	1/3	38.8	3
11	LGW01-61	268.34	3.54	2/3	47.59	1
12	LGW01-64	324.45	5.3	2/3	47.59	5
13	LGW01-99	319.38	5.07	1/3	44.83	2
14	LGW02-57	334.44	4.99	1/3	36.63	2
15	LGW02-58	296.39	4.26	2/3	47.59	3
16	LGW02-59	296.39	4.26	2/3	47.59	3
17	LGW02-60	296.39	4.26	2/3	47.59	3
18	LGW02-61	310.41	4.73	1/3	36.63	4
19	LGW02-86	310.41	4.73	1/3	36.63	4
20	LGW02-87	348.46	5.47	0/3	27.84	2
21	LGW02-91	372.48	5.72	0/3	27.84	0
22	LGW02-92	322.42	4.86	1/3	38.8	2
23	LGW02-95	336.45	5.34	0/3	27.84	3
24	LGW02-99	296.39	4.26	2/3	47.59	3
25	LGW03-01	348.46	5.47	0/3	27.84	2
26	LGW03-06	372.48	5.23	2/3	47.59	0
27	LGW03-07	308.40	4.43	1/3	38.8	2
28	LGW03-12	322.42	4.9	0/3	27.84	3
29	LGW03-13	294.37	3.87	2/3	47.59	1
30	LGW03-18	308.40	4.35	1/3	36.63	2
31	LGW03-21	336.45	5.35	0/3	27.84	3
32	LGW03-23	322.42	4.87	1/3	38.8	2
33	LGW03-31	338.47	5.73	0/3	27.84	5

*H bond: Hydrogen Bond

Table 4.2.2: *Oxazine derivative library physiochemical properties.*

Number	Compound ID	Molecular weight	LogD (pH7.4)	Number of H bond donor/acceptor	Polar surface area	Number of Rotatable bonds
34	LGW03-32	320.41	4.6	0/3	27.84	1
35	LGW03-37	292.35	3.48	2/3	47.59	0
36	LGW03-41	310.37	3.53	1/4	45.86	2
37	LGW03-52	296.34	3.06	2/4	56.82	1
38	LGW03-57	376.51	6.21	0/3	27.84	3
39	LGW03-65	352.49	6.24	0/3	27.84	5
40	LGW03-76	296.39	4.5	0/3	27.84	3
41	LGW03-88	294.37	3.9	1/3	36.63	2
42	LGW04-31	324.45	5.26	1/3	36.63	5
43	LGW04-32	310.42	4.78	2/3	47.59	4
44	LGW04-36	282.37	4.02	1/3	38.8	2
45	LGW04-81	282.37	3.9	2/3	47.59	2
46	LGW04-84	296.39	4.38	1/3	36.63	3
47	LGW04-91	348.47	5.49	0/3	27.84	1
48	LGW05-33	330.84	4.82	1/4	36.63	4
49	LGW05-39	337.22	4.44	2/5	47.59	3
50	LGW05-42	316.81	4.35	2/4	47.59	3
51	LGW05-65	338.43	4.53	0/4	37.07	3
52	LGW05-66	428.60	7.21	0/3	27.84	2
53	LGW05-73	352.41	3.84	0/5	46.3	2
54	LGW05-75	324.40	4.05	1/4	48.03	2
55	LGW05-76	308.40	4.42	1/3	38.8	2
56	LGW05-81	300.36	3.88	2/4	47.59	3
57	LGW05-82	314.38	4.36	1/4	36.63	4
58	LGW05-84	322.43	4.9	0/3	27.84	3
59	LGW05-85	280.35	3.42	2/3	47.59	1
60	LGW05-91	304.32	3.51	2/5	47.59	3
61	LGW06-10	268.34	3.6	2/3	62.58	1
62	LGW06-11	282.37	4.08	1/3	50.62	2
63	LGW06-14	240.29	2.94	2/3	73.2	0
64	LGW06-97	254.31	3.08	2/3	61.58	1
65	LGW07-55	264.31	2.59	2/3	47.59	0
66	LGW07-59	320.42	4.58	0/3	27.84	2

*H bond: Hydrogen Bond

Table 4.3 *Physiochemical property agreement with rules for in vivo nerve targeted small molecules*

Property	Low - High	Lipinski & Veber	Pajouhesh & Lenz
Max Abs./Em.:	Abs: 603 – 702nm / Em: 625 – 720 nm		
Brightness:	0.05 – 39.28		
Molecular Weight:	240.3 g/mol – 428.6 g/mol	MW: < 500 g/mol (all)	MW: <450 g/mol (all)
LogD:	2.59 – 7.21	LogD: < 5 (47)	LogD: < 5 (47)
H Bond Donors/Acceptors:	HBD: 0 – 2 / HBA: 3 – 5	HBD: < 5 (all) / HBA: < 10 (all)	HBD: < 3 (all) / HBA: < 7 (all)
Polar Surface Area:	27.84 – 73.2 Å^2	PSA: < 140 Å^2 (all)	N/A

In vivo direct and systemic administration nerve-specificity screening

Each compound in the oxazine library was screened *in vivo* using both direct and systemic administration to determine nerve specificity and assess nerve contrast generated using each administration strategy. The direct administration strategy enabled quantification of nerve-specificity and contrast following direct contact of the fluorophore with the nerve and its surrounding tissues without the requirement of BNB penetration. The systemic administration screening studies required not only nerve-specificity, but also BNB penetration to generate nerve-specific signal and contrast. Following either direct or systemic administration, fluorescence images of the brachial plexus and sciatic nerves were acquired and nerve, muscle, cut muscle, and adipose signal intensities were quantified (**Fig. 4.1 & 4.2**). Nerve intensity varied widely across the library, with brighter overall signal following direct administration (**Fig. 4.1A)** compared to systemic administration (**Fig. 4.2A**). The tissue intensities were used to generate N/M, N/A and N/CM SBRs, where the N/M SBR was used as a metric of nerve contrast (**Fig. 4.1B & 4.2B**). N/M ratios varied widely between library compounds with values ranging from 0.73 to 5.29 for direct administration (**Fig. 4.1B**) and from 0.69 to 3.43 for systemic administration (**Fig. 4.2B**). All oxazine derivatives with a significantly higher N/M ratio compared to the control group (* = $p < 0.05$, ** = $p < 0.01$, *** = $p < 0.001$, **** = $p < 0.0001$) were considered to have nerve specificity and provide positive nerve contrast. Thus, following direct administration screening, 51 oxazine derivatives were found to provide positive nerve contrast, while 46 oxazine derivatives provided positive nerve contrast following systemic administration screening. As expected, a handful of compounds displayed positive nerve specificity via direct administration but were negative via systemic administration including LGW06-97, 06-10, 05-91, 02-95, 07-65, 01-64, 01-44, and 03-01. Surprisingly, several compounds displayed negative

nerve specificity via direct administration but were positive via systemic administration including LGW05-84, 02-92, and 03-07.

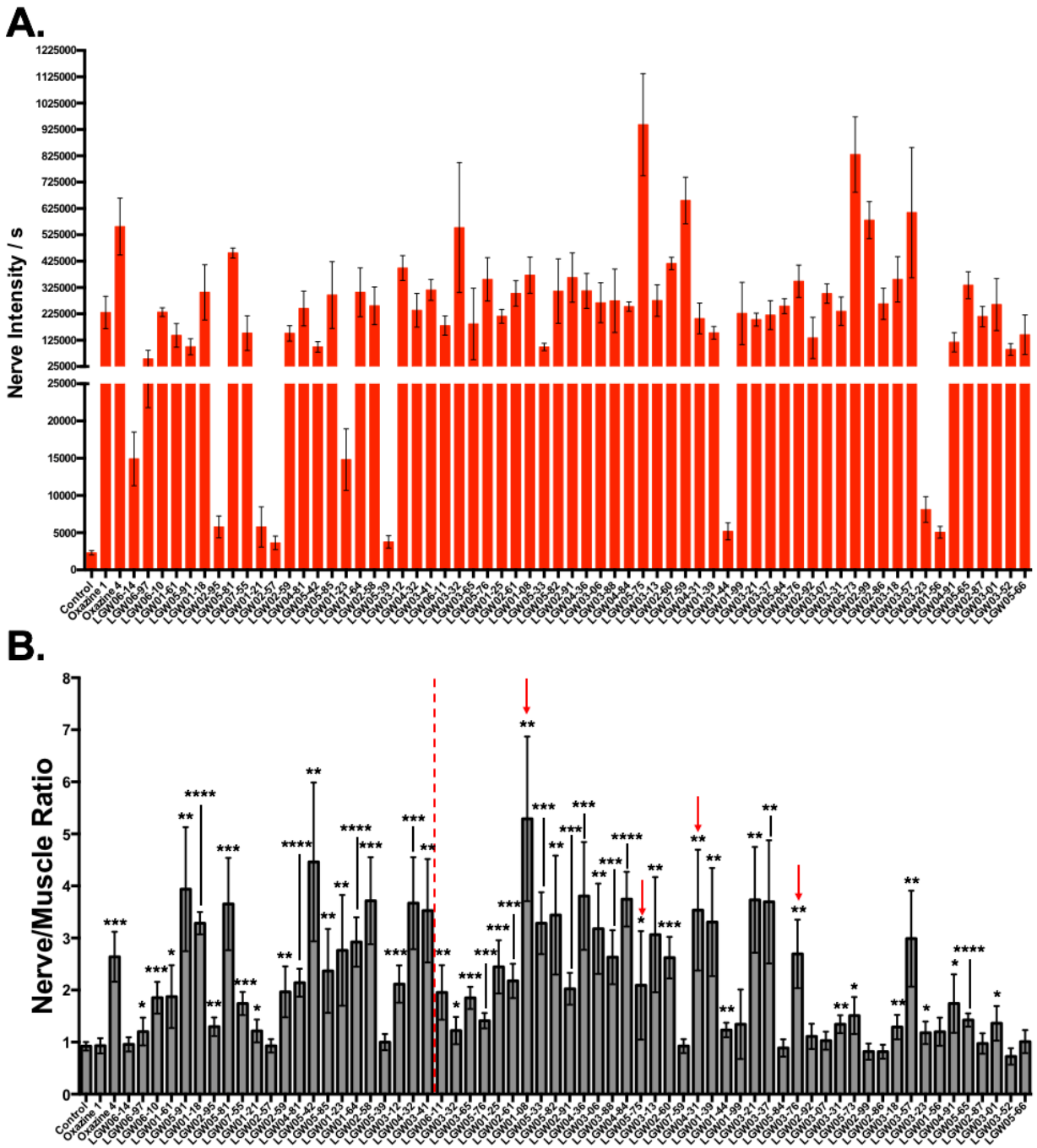

Figure 4.1: *Direct administration oxazine derivative library screening*. Average **(A)** nerve intensities and **(B)** nerve to muscle ratios for all 64 compounds in the oxazine derivative library as well as for unstained control, Oxazine 1, and Oxazine 4 following direct administration staining. All fluorophores in the library are organized by maximum emission wavelength from lowest on

the left to highest on the right. Fluorophores to the right of the red dotted line had emission maxima >650 nm. Red arrows highlight the top candidates chosen for further analysis. Averages are calculated from data collected for n=6 nerve sites per fluorophore and are presented as mean +/- standard deviations. Data for each fluorophore was compared to control unstained data to test for the significance of N/M SBR. * = p value < 0.05, ** = p value < 0.01, *** = p value < 0.001, **** = p value < 0.0001.

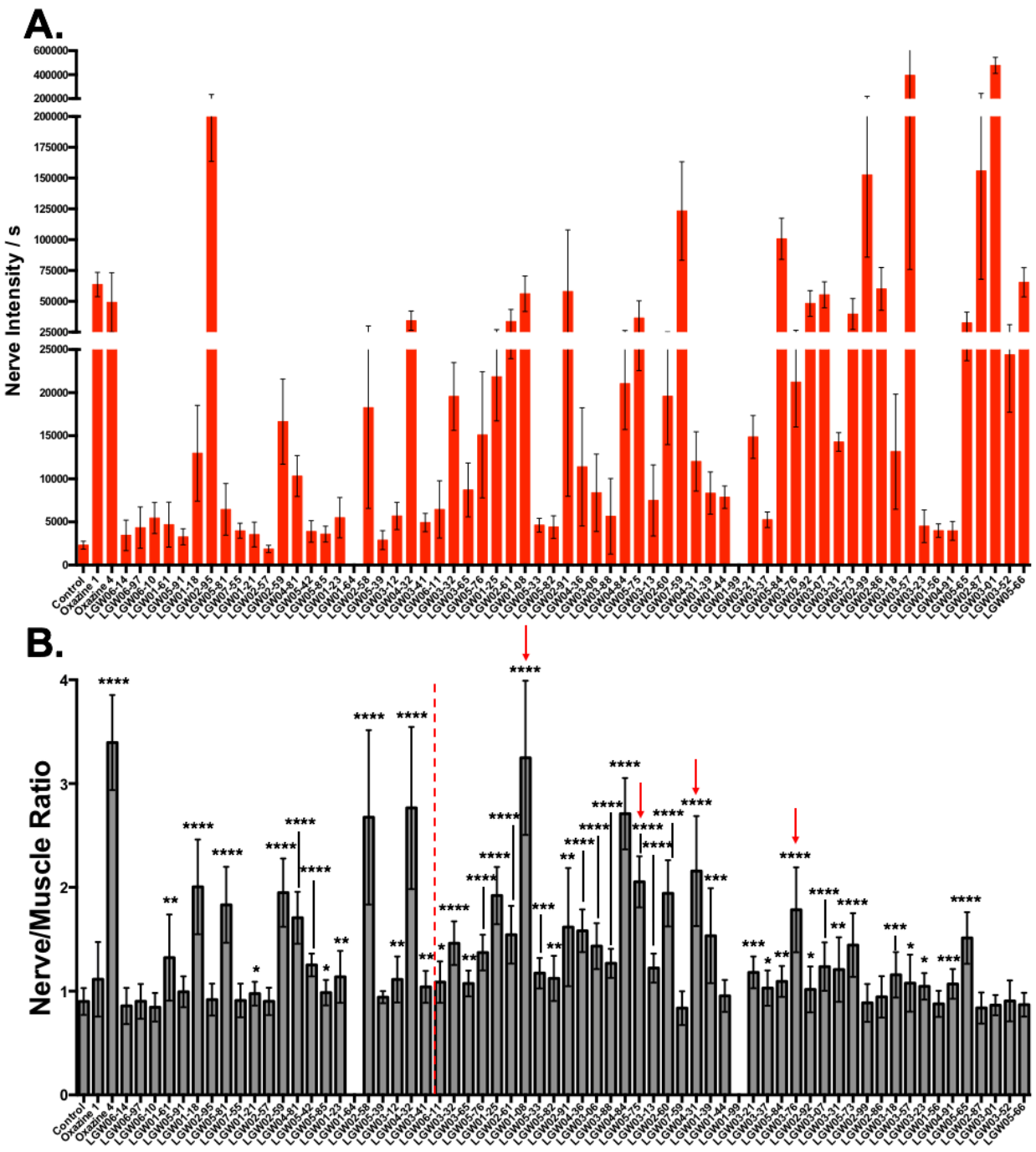

Figure 4.2: *Systemic administration oxazine derivative library screening*. Average **(A)** nerve intensities and **(B)** nerve to muscle ratios for all 64 compounds in the oxazine derivative library as well as for unstained control, Oxazine 1, and Oxazine 4 following systemic administration staining. All fluorophores in the library are organized by maximum emission wavelength from lowest on the left to highest on the right. Fluorophores to the right of the red dotted line had emission maxima > 650 nm. Red arrows highlight the top candidates chosen for further analysis. Averages are calculated from data collected for n=12 nerve sites per fluorophore and are presented as mean +/- standard deviations. Data for each fluorophore was compared to control unstained data

to test for the significance of N/M SBR. * = p value < 0.05, ** = p value < 0.01, *** = p value < 0.001, **** = p value < 0.0001.

Top oxazine derivative selection and large animal screening

Following completion of the *in vivo* nerve specificity screening studies, four top candidate oxazine derivatives were selected for additional study (**Fig. 4.1 & 4.2**). The top four oxazine compounds were selected based on their NIR spectral properties, high nerve specificity following both direct and systemic administration, and structural diversity (**Fig. 4.3**). Representative images, quantified nerve SBRs, and tissue intensities from direct and systemic administration *in vivo* screening studies are displayed in **Figure 4.4 & 4.5**, respectively. The chosen compounds demonstrated variability in the degree of nerve specificity evident through the nerve SBR values and nerve fluorescence intensities in the normalized images and quantified tissue intensity values. Importantly, all compounds displayed significantly higher N/M ratios than the negative control compound Oxazine 1 via both direct and systemic administration (**Fig. 4.4B & 4.5B**). Additionally, all chosen compounds displayed significantly higher N/A and N/CM ratios than Oxazine 1 except for 05-75 via direct administration.

The top library candidate, LGW01-08 was screened in swine via systemic administration and nerves lining the body cavity were visualized using a laparoscopic fluorescence imaging system integrated into the da Vinci Si endoscope (**Fig. 4.6**). Nerve tissue was identified underlying several millimeters of tissue using LGW01-08 fluorescence that were invisible in white light illumination (**Fig. 4.6A**). The nerve tissue detected via fluorescence was subsequently confirmed via white light illumination following dissection through the overlaying tissue (**Fig. 4.6B**).

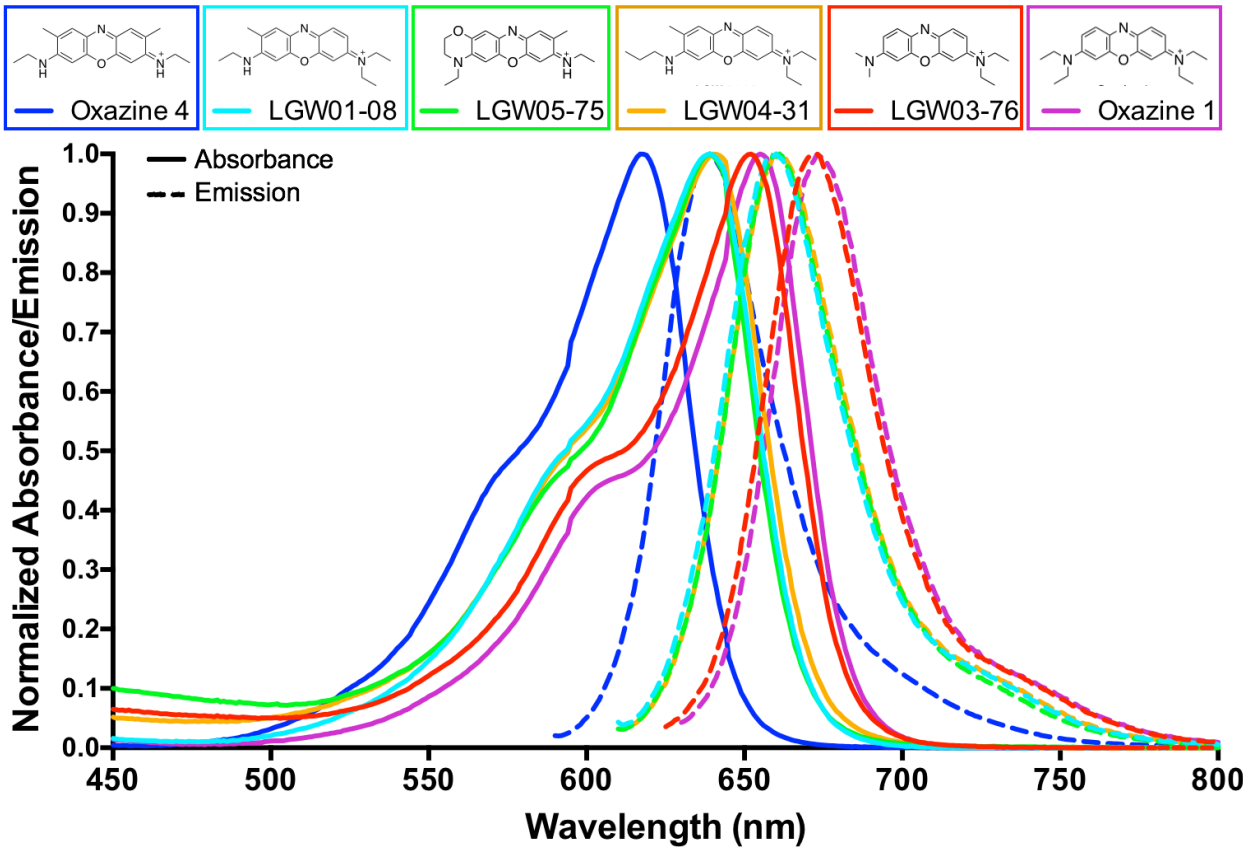

Figure 4.3: *Oxazine library top candidates fluorescence spectra*. Absorbance and emission spectra of the four top candidate Oxazine derivatives for clinical translation chosen from the library of 64 oxazine derivatives shown in comparison with parent compounds Oxazine 4 and Oxazine 1. Absorbance and emission values are normalized to the maximum value for each curve and thus are displayed as a % of maximum.

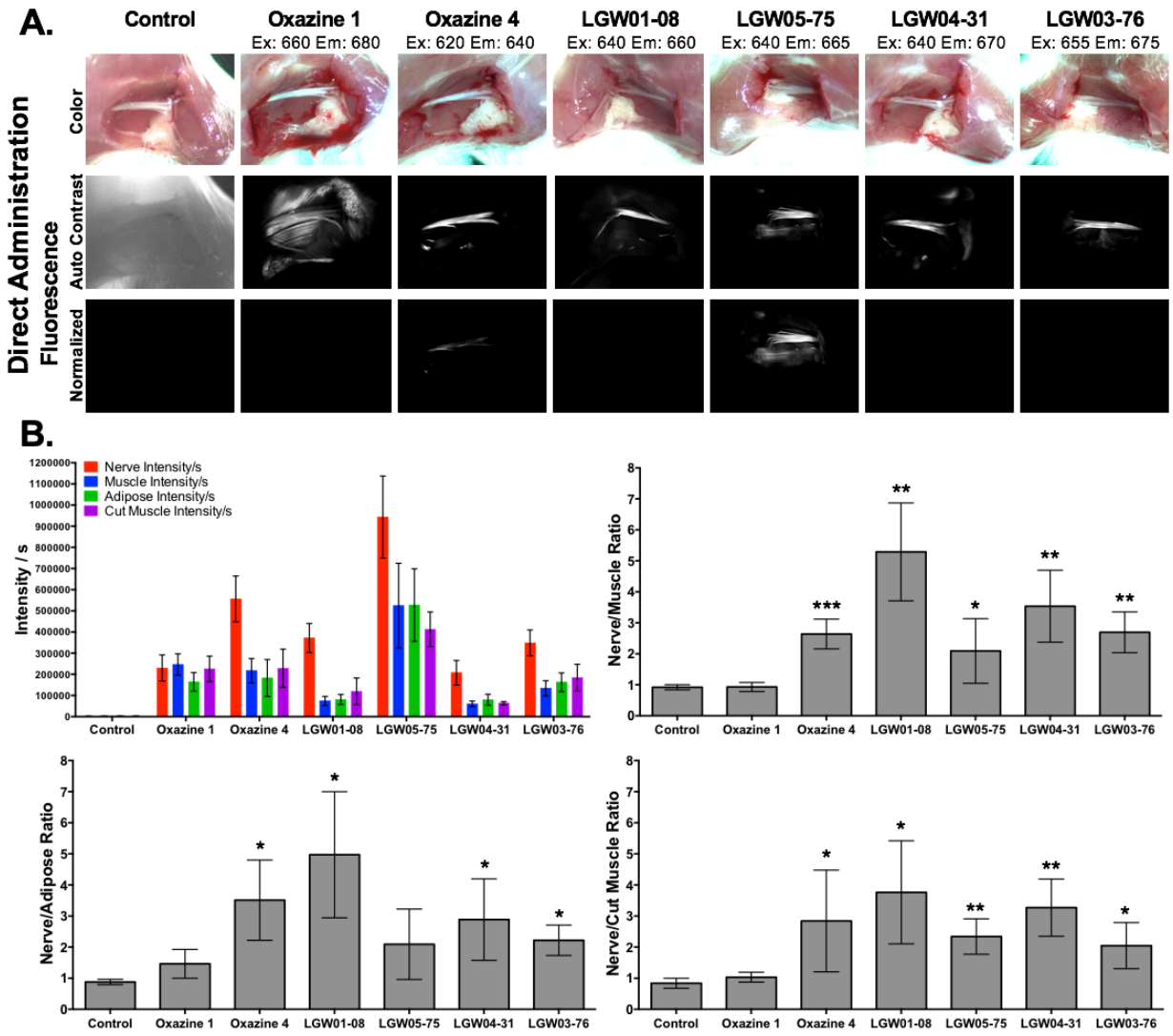

Figure 4.4: *Oxazine library top candidates direct administration screening data*. **(A)** Representative images and **(B)** quantified intensities and nerve SBRs for the top candidates for clinical translation direct administration screening data. All images are representative of data collected for n=6 nerve sites per fluorophore. All quantified data is presented as mean +/- standard deviation. Ex = max excitation (nm), Em = max emission (nm). Data for each fluorophore was compared to Oxazine 1 data to test for significance. * = p value < 0.05, ** = p value < 0.01, *** = p value < 0.001, **** = p value < 0.0001.

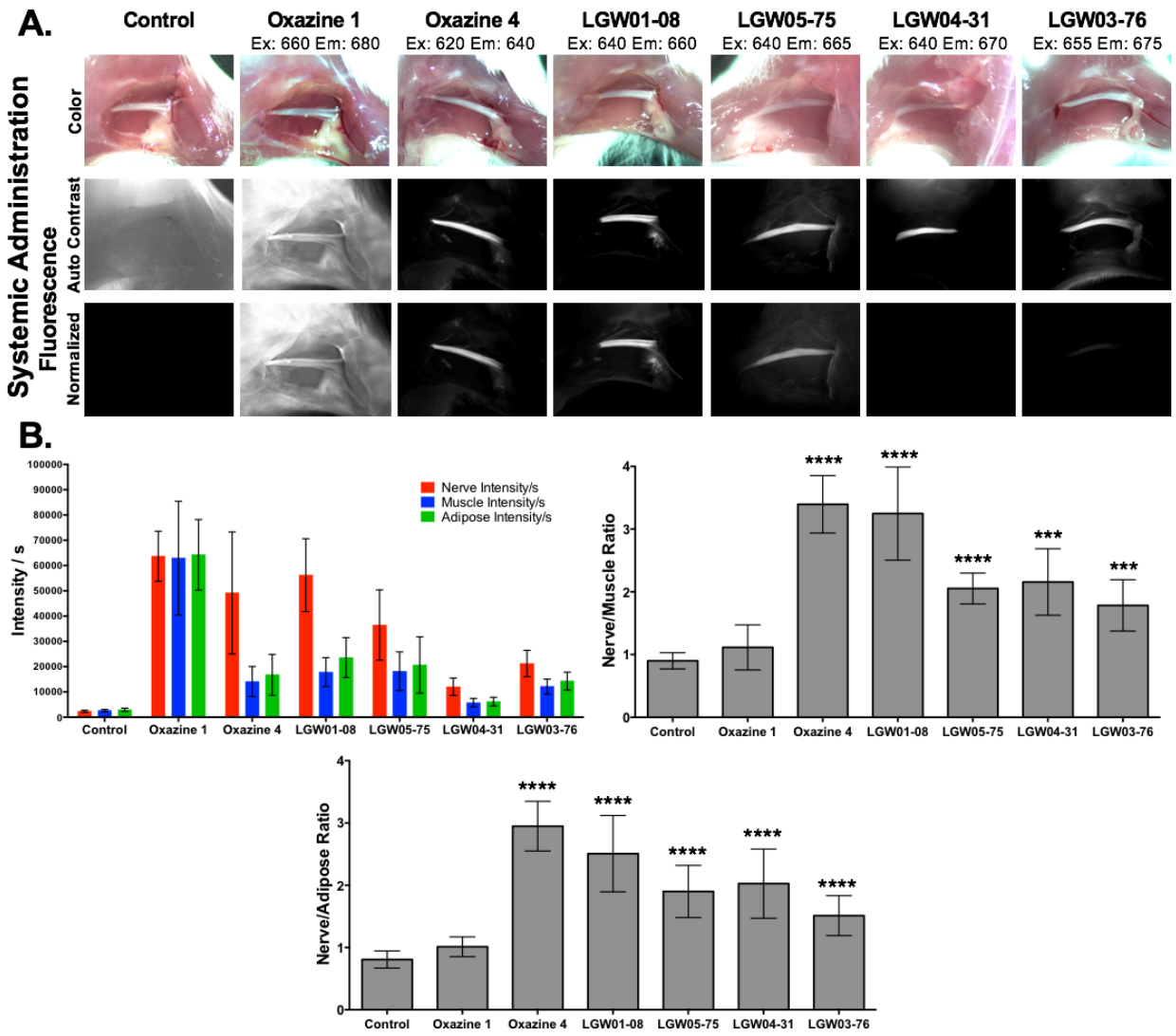

Figure 4.5: *Oxazine library top candidates systemic administration screening data*. **(A)** Representative images and **(B)** quantified intensities and nerve SBRs for the top candidates for clinical translation systemic administration screening data. All images are representative of data collected for n=12 nerve sites per fluorophore. All quantified data is presented as mean +/- standard deviation. Ex = max excitation (nm), Em = max emission (nm). Data for each fluorophore was compared to Oxazine 1 data to test for significance. * = p value < 0.05, ** = p value < 0.01, *** = p value < 0.001, **** = p value < 0.0001.

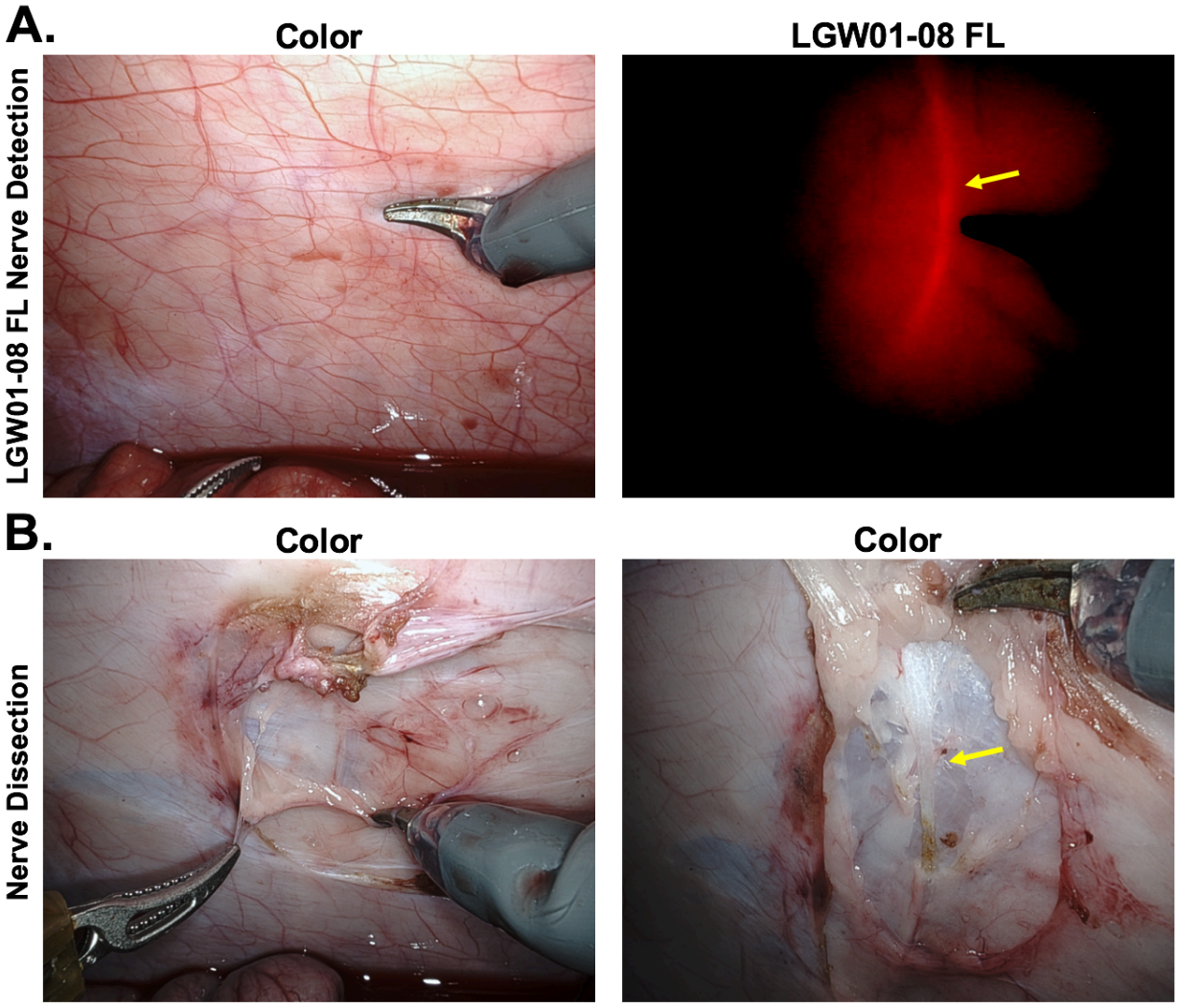

Figure 4.6: *Large animal LGW01-08 screening.* Images displaying LGW01-08 enabled nerve detection **(A)** and confirmation following nerve dissection **(B)** of nerves lining the body cavity during swine laparoscopic surgery using the da Vinci surgical system. Yellow arrows highlight the identified nerve. FL = Fluorescence.

DISCUSSION

FGS has the potential to revolutionize surgery, making it possible for surgeons to more easily identify diseased tissues to be removed and vital tissues to be spared. Sparing of vital nerve structures could be vastly improved through the use of targeted nerve-specific fluorophores that can be visualized in the NIR. In the work presented herein, a focused library of 64 oxazine derivates was synthesized and screened for tissue specificity in order to determine factors that dictate a compound's nerve

specificity and identify NIR nerve-specific fluorophore candidate(s) for clinical translation to FGS. Aspects of each fluorophores photochemical and structural properties were carefully considered during library design and development to maximize diversity and yield nerve targeting molecules. The fluorophore library synthesized and characterized by Dr. Wang contained compounds with a wide range of fluorescent brightness as well as absorbance and emission wavelengths (**Table 4.1**). Importantly, the diversity of the fluorophore library lead to 42 out of the 64 compounds possessing NIR emission wavelengths, representing the first NIR nerve-specific small molecule fluorophores reported to date. Furthermore, the physiochemical properties of the majority of the 64 library compounds are within the requirements for tissue targeting according to the Lipinski[160] and Veber[161] rules and the requirements for nerve uptake and binding according to the Pajouhesh and Lenz[162] rules (**Table 4.3**). LogD values ranged from 2.59 to 7.21 leaving 47 compounds with LogD values <5 as required by the Lipinski rules. All 64 novel oxazine derivatives had molecular weights (Lipinski rule: <500 g/mol, oxazine derivatives: 240.3 to 428.6 g/mol), hydrogen bond donors (Lipinski rule: <5, oxazine derivatives: 0-2), hydrogen bond acceptors (Lipinski rule: <10, oxazine derivatives: 3-5), and polar surface areas (Veber rule: <140 $Å^2$, oxazine derivatives: 27.8 and 73.2 $Å^2$) that fell within the range defined by Lipinski and Veber for tissue targeting.[160, 161] These properties were also in agreement with the rules set out by Pajouhesh and Lenz[162] for successful nerve targeting drugs with all molecular weights <450 g/mol for adequate BNB penetration, all hydrogen bond donors <3, all hydrogen bond acceptors <7, all polar surface areas <70 $Å^2$, and most Log D values <5 (**Table 4.3**).

Library nerve specificity screening was performed *in vivo* using both direct and systemic administration strategies since several oxazine fluorophores, including Oxazine 4, have demonstrated negative *ex vivo* staining in tissue sections.[111] Additionally, *in vivo* screening via two routes of administration allowed for more accurate determination of factors involved with *in vivo* nerve specificity. Following screening using both direct and systemic administration, a large diversity in fluorescence staining intensity and degree of nerve specificity was observed (**Fig. 4.1 & 4.2**). Interestingly, variations in nerve intensity values did not necessarily correlate with fluorophore brightness levels determined via spectrophotometric analysis. This could be due to differences in the nerve uptake characteristics of each compound, which was highly variable as evident by the range of nerve SBRs

reported. In fact, an analysis of the correlation between the calculated physiochemical properties and resulting nerve SBRs yielded no strong relationship between any one of the calculated properties and nerve specificity (data not shown), suggesting that a compound's nerve targeting ability is inherent from a combination of two or more physiochemical properties and/or specific structural fingerprint. Further analysis and quantitative structure activity relationship (QSAR) modelling is needed to fully elucidate the factors responsible for nerve specificity.

Overall nerve intensity and SBR values were higher following direct administration (**Fig. 4.1 & 4.2**), with 51 compounds having positive nerve contrast following direct administration and 46 compounds having positive nerve contrast following systemic administration. These results demonstrate the increased difficulty to obtain positive nerve specificity via systemic administration versus direct administration. Intravenously injected probes must cross the BNB and clear from the surround tissues in order to reach the target tissue and create nerve contrast. Additionally, nerve targeting probes injected systemically will bind to all of the nerve tissue in the body, decreasing the local dose in the nerve structure of interest and making it difficult for dimmer fluorophores to be detected. Therefore, library compounds with unfavorable biodistribution, low BNB penetration characteristics, or low brightness levels will never reach nerve tissue or remain undetected over background autofluorescence levels. Direct administration directly to the nerve structure of interest and the surrounding tissue allows for localized uptake via diffusion resulting in several orders of magnitude higher nerve fluorescence intensity values due to increased local dose for improved nerve detection.

Four library compounds were chosen as the top candidates for clinical translation: LGW01-08, 03-76, 04-31, and 05-75. These compounds were chosen for their high nerve specificity and fluorescence intensity following both direct and systemic administration, NIR fluorescence emission, and structural diversity (**Fig. 4.1-4.3**). Representative images, tissue intensity, and nerve SBRs were compiled for these compounds from direct (**Fig. 4.4**) and systemic (**Fig. 4.5**) screening studies. LGW01-08 provided the highest nerve SBRs using both screening methods, however all candidates demonstrated significantly higher nerve SBRs than the negative control Oxazine 1, aside from 05-75 in direct administration N/A ratio. Interestingly, derivatives that are structural hybrids of Oxazine 4 and Oxazine 1 such as LGW01-08 provided excellent performance, suggesting only part of the parent Oxazine 4 structure is responsible for nerve specificity. Additionally, LGW01-08

was screened in a large animal swine model and enabled the identification of buried nerve tissue in a laparoscopic scenario invisible to conventional white light visualization (**Fig. 4.6**). Based on the excitation and emission wavelengths, *in vivo* fluorescence intensities, and resulting nerve SBRs, LGW01-08 appears to be a strong choice for clinical translation, offering the maximum nerve specificity, a NIR fluorescence emission, and fluorescence excitation possible at the popular 640 nm laser line.

The work presented herein has developed and characterized a focused library of oxazine derivates to determine the factors responsible for nerve binding and identified novel NIR fluorophore candidates for clinical translation. The generated library possessed diverse physiochemical properties and nerve binding characteristics, however no single factor appeared to be responsible for nerve specificity and more in-depth analysis including QSAR modelling is warranted to determine the factors responsible for nerve specificity. Many of the compounds in the library demonstrated NIR fluorescence and positive nerve specificity, and four compounds showed promise for clinical translation and further study. Large animal screening of the lead compound LGW01-08 demonstrated the power of these probes in enabling identification of nerve tissue completely invisible to the naked eye under white light illumination. By yielding the first NIR nerve specific small molecule fluorophores and reporting on their use in FGS application, this study has substantially advanced nerve sparing FGS technology towards first-in-human trials and clinical use for improving surgical outcomes affected by nerve damage.

Chapter 5

A clinically relevant formulation for direct administration of nerve specific probes during fluorescence image guided surgery

ABSTRACT

Iatrogenic nerve injury significantly affects surgical outcomes for procedures like the radical prostatectomy (RP), with up to 60% of patients reporting nerve damage one to two years post-surgery. Although nerve sparing RP techniques have been practices for over 30 years, it remains difficult for surgeons to identify nerve tissue intraoperatively and nerve sparing success rates are strongly correlated with experience level. Fluorescence guided surgery (FGS) offers a potential solution for improved nerve sparing by providing direct visualization of nerve tissue intraoperatively. However, novel probes for FGS face an extraordinary regulatory challenge to achieve clinical translation. Previously, a direct administration methodology was developed that enabled application of nerve-specific fluorophores at a much lower dose than systemic administration for clinical translation via exploratory IND guidance. However, a clinically viable formulation was necessary to advance this promising technology to clinical use. Previously a non-FDA approved co-solvent formulation was utilized which resulted in significant background staining in preliminary large animal studies from a lack of staining control inherent to liquid-based formulations. In the present study, we report on the development of a clinically viable gel-based formulation strategy that enables direct administration of a nerve-specific fluorescent contrast agent with increased control for nerve sparing FGS applications. An F127 Pluronics formulation was used to solubilize a novel near-infrared nerve specific oxazine fluorophore, LGW01-08, providing increased staining control for a variety of tissue surfaces, angles, and morphologies. Additionally, the formulation developed herein possesses unique gelling characteristics, allowing it to easily be spread as a liquid followed by rapid gelling at body temperature for subsequent tissue hold. Further optimization of the direct administration protocol has decreased the total staining time to 1-2 minutes, improving compatibility with surgical procedures. The resulting gel formulation and direct administration methodology provides an excellent platform for clinical translation of novel nerve-specific fluorophores for FGS.

INTRODUCTION

Nerve damage plagues surgical outcomes, significantly affecting post-surgical quality of life. Despite the practice of nerve sparing techniques for decades, intraoperative nerve identification and sparing remains difficult and success rates are strongly correlated with surgeon experience level and ability to master the technique.[14, 126, 128] Fluorescence-guided surgery (FGS) shows promise for enhanced visualization of specifically highlighted tissue, such as nerves, intraoperatively. FGS offers high sensitivity, wide-field, real-time imaging, and with optimized molecular specific probes, targeted tissues could be identified at millimeter to centimeter depths. Several imaging systems have already been developed for FGS applications.[15-23] Importantly, the da Vinci surgical robot, frequently used for robotic assisted radical prostatectomy (RP), a procedure especially affected by nerve damage, can be equipped with an FDA approved fluorescence imaging channel.[6, 127] Several classes of small molecule fluorophores have demonstrated nerve specificity in preclinical models.[20, 64-74] Of these, Oxazine 4 has shown promise for further translation with a red-shifted absorption and emission and high nerve specificity in murine and porcine nerve models.[74] However, few efforts in clinical translation of targeted imaging agents for FGS have been successful to date, largely due to the regulatory challenge and enormous cost of introducing diagnostic imaging agents into the clinic.

Direct administration is an attractive alternative to systemic administration of fluorescent probes for minimizing potential toxicity and easing regulatory burdens for first in human clinical studies. By selectively labeling tissues within the surgical field, direct administration requires a significantly lower dose than systemic administration. Recently, we have developed a direct administration methodology that provides equivalent nerve signal to background (SBR) to systemic administration following a 15-minute staining protocol (**Chapter 3**). This methodology has been successfully applied to autonomic nerve models, which closely mimic the nerves surrounding the prostate. This method has additional benefits in the application to RP since nerve labeling via systemic administration during RP would generate high background from nerves in the prostate, which are not able to be spared, and renal fluorophore clearance, producing significant fluorescence signal in the urine within the adjacent bladder. Both of these extraneous

fluorescence signals would diminish the ability to identify the cavernous nerves within the neurovascular bundle (NVB), which are responsible for continence and potency.[61, 62, 163] Perhaps most importantly, the direct administration methodology requires 16 times lower dose than systemic administration and when scaled to humans by body surface area the dose falls within the requirements for clinical translation under an exploratory investigational new drug (eIND) application to the FDA. Studies conducted under an eIND require minimal preclinical toxicity testing, since only a microdose (<100 μg) is administered to each patient, significantly reducing the cost of first-in-human studies.

While the direct administration methodology has provided high nerve specificity and SBR with a short staining protocol in preclinical rodent models (**Chapter 3)**, preliminary staining studies in large animal models generated significant background. To faciliate clinical translation, an improved formulation strategy that is FDA approved and facilitates increased application control for staining a variety of tissue surfaces, angles, and morphologies will be required. The previously utilized co-solvent formulation is stable at room temperature for <30 minutes, cannot solubilize concentrations above 5mg/mL, and requires the use of dimethyl sulfoxide and Kolliphor EL as solubilizing agents, which will hamper clinical translation due to vehicle induced toxicity issues. Additionally, the co-solvent formulation is liquid based and thus not ideal for staining angled or vertical tissue surfaces. Several gel and foam based formulations are utilized clinically as intraoperative hemostatic agents and surgical sealants including FloSeal (Baxter, Deerfield, IL), Surgiflo (Ethicon, Somerville, NJ), and Duraseal (Integra, Plainsboro, NJ). In the present study, we have developed a gel based formulation modeled after these surgical tools using the clinically approved F127 Pluronics solubilizing agent, which has attractive gelling characteristics for FGS applications. Herein, F127 Pluronics was used to solubilize LGW01-08, a near infrared nerve specific oxazine flurophore chosen as the lead compound of the oxazine derivate library created in our lab (**Chapter 4**). Additionally, we have developed an improved direct administration methodology for application of the gel formulation and a simplified washing protocol, decreasing the overall direct administration staining protocol to 1-2 minutes. The improved platform for direct administration developed herein meets all requirements for rapid and successful clinical translation of nerve-targeted FGS for improved nerve identification during surgeries like the nerve-sparing RP.

MATERIALS & METHODS

Contrast agents and formulations

LGW01-08 was chosen as the lead compound for development from a library of 64 oxazine derivatives synthesized in the Gibbs laboratory by Dr. Lei Wang. All synthesis, purification, and characterization of the novel fluorophore was carried out by Dr. Wang at the OHSU and PSU campuses. The previously used co-solvent formulation containing 10% dimethyl sulfoxide (DMSO), 5% Kolliphor EL, 65% serum, and 20% phosphate buffered saline (PBS) was used for comparison to the gel formulations presented herein.[20] All sodium alginate (Na Alginate) and F-127 Pluronics (Pluronics) formulations were prepared in the Alani laboratory by Dr. Vidhiben Shah. All purification and characterization of the novel formulations was carried out by Dr. Shah at the OHSU and OSU campuses.

Animals

Approval for the use of all small animals in this study was obtained from the Institutional Animal Care and Use Committee (IACUC) at Oregon Health and Science University (OHSU). Male CD-1 mice weighing 22-24g were purchased from Charles River Laboratories (Wilmington, MA). Prior to surgery, animals were anaesthetized with 100 mg/kg ketamine and 10 mg/kg xylazine (Patterson Veterinary, Devens, MA) administered intraperitoneally (IP). The brachial plexus and sciatic nerves were surgically exposed by removal of overlaying adipose and muscle tissues for direct nerve staining and imaging.

Gel formulation screening and viscosity testing

Each novel gel-based formulation was tested in mice using the direct administration methodology developed using the liquid based co-solvent formulation to ensure no significant loss in the resulting fluorescence intensity or nerve signal-to-background ratios (**Chapter 3**). LGW01-08 was formulated in 5, 6.5, and 8% Na Alginate as well as 20, 22, and 25% Pluronics at 125 μM concentration.

Each exposed brachial plexus and sciatic nerve site was incubated with the formulated fluorophore for 5 min, followed by 9 flushes with PBS, a secondary 5 min incubation with blank formulation, and 9 additional washes to remove non-specifically bound fluorophore. Fluorescence and color images were acquired immediately following staining and 30 minutes following staining to observe improvements in nerve SBRs due to clearance. Nerve sites were stained with LGW01-08 in the previously utilized co-solvent formulation as positive controls and unstained nerve sites were imaged as negative controls (n=3 mice or 6 nerve sites per condition).[20, 63, 66]

To determine the most clinically viable amount of viscosity enhancer within each gel formulation, Oxazine 4 at 1 mM in 5, 6.5, and 8% Na Alginate as well as 20, 22, and 25% Pluronics was dropped onto swine intestinal tissue that had been shimmed to 0, 35, and 65º angles. A 1 mL pipette was used to apply 300 µL of each formulation to porcine small intestine held on an angled shim. The small intestine was kept at internal body temperature and only removed externally for testing the formulation. A new section of small intestine was used to test each direct formulation. All small intestine regions were gently wiped with medical gauze to remove any noticeable quantities of serous fluid. A color photograph was taken 30 seconds after direct formulation application for surface area analysis using ruler measurements on the tissue shims adjacent to the tissue. All direct formulations were tested in triplicate. Surface area measurements were used to determine the tissue spread and administration control characteristics.

Direct administration protocol testing

To adapt the previously developed direct administration methodology to gel formulation application, the fluorophore concentration, incubation time, and washing protocols were optimized for the chosen gel formulation. 25, 50, and 200 µg/mL concentrations of LGW01-08 at 1- and 5-minute incubation times in 22% Pluronics were used to stain the brachial plexus and sciatic nerve sites followed by 18 PBS wash steps. Following determination of the most clinically viable concentration and incubation time, efforts to shorten the washing protocol were investigated. Images were collected following each flush step for 6 washes and then every 3 washes out to 18 washes. Washing was completed using PBS stored at 4º Celsius to test for improved ability to liquify the gelled Pluronics solution compared

to warm 37º Celsius PBS. Washes consisted of a short flush of PBS followed immediately by removal by absorption with gauze.

Large animal testing

To validate the direct administration protocol and novel gel formulations in a more clinically relevant surgical model, the gel formulation was applied laparoscopically to the illiac plexus in swine using the da Vinci Si surgical robotic system (Intuitive Surgical, Sunnyvale, CA). The direct administration gel and liquid formulation protocols were used to stain the swine illiac plexus and the surrounding muscle and adipose tissue with 1mM Oxazine 4 solubilized in the Pluronics and co-solvent formulations, respectively. Color and fluorescence images were acquired two and a half hours following staining to ensure adequate nerve contrast due to clearance of the higher dose administered and that resulting nerve signal was maintained for the duration of a typical surgical procedure.

Intraoperative fluorescence imaging system

A custom-built small animal imaging system capable of real-time color and fluorescence imaging was used to acquire rodent *in vivo* images. The imaging system consisted of a QImaging EXi Blue monochrome camera (Surrey, British Columbia, CA) for fluorescence detection with a removable Bayer filter for collecting co-registered color and fluorescence images. A PhotoFluor II light source (89 North, Burlington, VT) was focused onto the surgical field through a liquid light guide and used unfiltered for white light illumination. For fluorescence excitation, the PhotoFluor II was filtered with a 620 ± 30 nm bandpass excitation filter. Resulting fluorescence was collected with a 700 ± 37.5 nm bandpass emission filter for image collection. All filters were obtained from Chroma Technology (Bellows Falls, VT). Camera exposure times ranged from 10 – 2000 ms for fluorescence image collection.

A custom-built laparoscopic imaging system also capable of real-time color and fluorescence imaging was used to acquire swine *in vivo* images. The imaging system was integrated into the da Vinci Si surgical system from Intuitive Surgical, Inc. (Sunnyvale, CA) and consisted of a Necsel Neon 5W 640nm laser (Necsel, Milpitas, CA) coupled to the da Vinci Si endoscope with a Semrock 642 nm StopLine single-notch blocking filter (Semrock, Rochester NY) to remove excitation

light from the acquired fluorescence images. The 642 nm StopLine blocking filter was placed in the Si camera sterile adaptor between the rod lens endoscope and the Si camera head. Fluorescent signal acquisition occurred in the Si white light mode with the blocking filter removing the 642 nm excitation light and the fluorescent signal detected primarily on the RGB red-Bayer elements. Laser power at the endoscope tip measured 800mW with optical power loses occurring primarily at the laser fiber/light guide and the Si camera head/rod lens interfaces. Fluorescence and color videos were captured using the Si Vision Side Cart at an exposure time of 2 ms. Images were taken from screen captures of the *in vivo* video clips. Videos were recorded on a Panasonic SDI recorder connected to the TilePro video out connections on da Vinci Si Vision Side Cart.

Intraoperative nerve imaging and image analysis

Nerve specific contrast was assessed for all initial testing, method testing, and large animal studies using the intraoperative fluorescence imaging systems. Additional unstained control animals were imaged to assess tissue autofluorescence. Custom written MatLab code was used to analyze the tissue specific fluorescence where regions of interest were selected using the white light images. These regions of interest were then analyzed on the co-registered matched fluorescence images permitting assessment of the mean tissue intensities and nerve to muscle (N/M), nerve to adipose (N/A), and nerve to cut muscle (N/CM) ratios. Intensity measurements were divided by the exposure time to obtain normalized intensity per second measurements.

Statistical analysis

Significant differences between nerve SBR means were evaluated using a one-way ANOVA followed by a Fisher's LSD multiple comparison test with no assumption of sphericity using the Geisser-Greenhouse correction to compare all mean nerve signal intensities and nerve to background tissue ratios. The α value was set to 0.05 for all analyses. Results were presented as mean ± standard deviation (S.D.). All statistical analysis was performed using GraphPad Prism (La Jolla, CA).

RESULTS

Preliminary nerve specificity screening using gel-based formulations

Two viscosity enhancers, sodium alginate (Na Alginate) and Pluronics, were used to create gel formulations for administration of the nerve specific fluorophore LGW01-08. Mouse brachial plexus and sciatic nerves were stained using direct administration with varying concentrations of each viscosity enhancer (5, 6.5, and 8% Na Alginate; 20, 22, and 25% Pluronics) to solubilize 125 μM LGW01-08. The staining results were compared to the previously utilized liquid based co-solvent formulation containing 125 μM LGW01-08 (**Fig. 5.1**). No major differences in nerve highlighting ability were observed for all concentrations of Na Alginate or Pluronics compared to the co-solvent formulation (**Fig. 5.1A**). No significant difference in nerve SBRs were observed between all formulations and all stain groups had significantly higher N/M, N/A, and N/CM ratios compared to the control unstained group. Additionally, aside from the highest concentrations of each viscosity enhancer (8% Na Alginate and 25% Pluronics) all gel formulations displayed similar nerve fluorescence intensities to the co-solvent formulation (**Fig. 5.1B**).

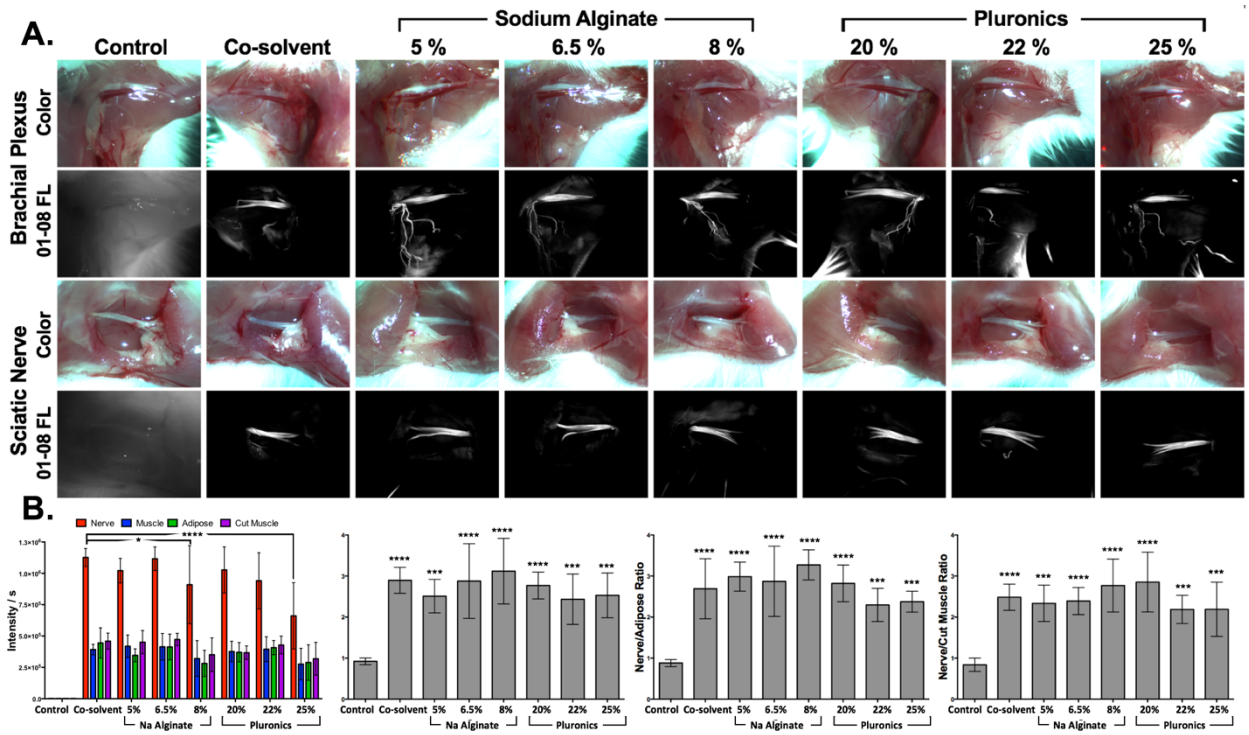

Figure 5.1: *Initial gel formulation screening*. **(A)** Representative images and **(B)** quantified intensities and nerve SBRs for each concentration of Na Alginate and Pluronics in 125µM LGW01-08 gel formulations for initial screening and comparison to the co-solvent formulation. All images are representative of data collected for n=6 nerve sites per fluorophore. Images are displayed without normalization. All quantified data is presented as mean +/- standard deviation. FL = fluorescence. Nerve intensity data for each formulation was compared to the co-solvent formulation data to test for significance. Nerve SBR data for each formulation was compared to control unstained data to test for significance. * = p value < 0.05, ** = p value < 0.01, *** = p value < 0.001, **** = p value < 0.0001.

Formulation composition, stability, and clinical status

The formulations tested herein were chosen for their high stability, clinical approval status, and advantageous viscosity and penetration characteristics. The composition, stability, and clinical toxicity profiles are outlined in **Table 5.1**. Both Na Alginate and Pluronics formulations provided unique and beneficial gel forming characteristics, while the co-solvent formulation was liquid only. Additionally, Na Alginate and Pluronics formulations are FDA approved, providing clinically viable formulation candidates.

Table 5.1: *Gel formulation composition, gel characteristics, and regulatory status.*

Formulation	Composition	Gel forming characteristics	Regulatory status
Cosolvent	10% DMSO, 5% Kolliphor, 85% 75/25 Serum/Buffer	Liquid only	None
Na Alginate	Sodium Alginate	Liquid to solid transition as temperature decreases, can form hydrogel in presence of Ca^{+2} ions in tissue	FDA Approved
Pluronics	F-127 Pluronics (PEO-PPO-PEO triblock copolymers)	Liquid to solid transition as temperature increases over a critical threshold, gel formation is reversible	FDA Approved

Gel formulation viscosity assessment

To assess the clinical utility of the viscosity enhancers for each gel formulation, tissue spread in swine was determined using formulations with 5, 6.5, and 8% Na Alginate as well as 20, 22, and 25% Pluronics at varying degrees of tilt (0º, 35º, and 65º) (**Fig. 5.2**). The lowest concentration of each viscosity enhancer tested (5% Na Alginate and 20% Pluronics) provided little resistance to increased tilt angle and saw significant increases in the measured spread surface area at 35º and 65º tilts. The middle concentration of each viscosity enhancer tested (6.5% Na Alginate and 22% Pluronics) provided adequate hold and did not see a large increase in spread at higher degrees of tilt. The highest concentration of each viscosity enhancer tested (8% Na Alginate and 25% Pluronics) allowed only minimal initial spread and no changes in tissue spread at higher tilt angles (**Fig. 5.2**). Due to the tradeoff between ability to spread following initial application and subsequent hold

at more vertical surface angles, the middle concentrations (6.5% Na Alginate and 22% Pluronics) were chosen as most clinically relevant for each formulation. Additionally, Pluronics was found to have more favorable gelling characteristics compared to Na Alginate. The viscosity of Pluronics increases at body temperature and decreases at cooler temperatures, including room temperature facilitating application to a tissue surface. By comparison, Na Alginate increases viscosity at cooler temperatures and decreases viscosity at higher temperatures, making both application and tissue gelling less advantageous. Due to these characteristics, Pluronics was chosen as the final viscosity enhancer for the gel formulation since it allowed initial spreading in the tissue to occur with relative ease and subsequently gelled quickly, remaining at the site of application on the tissues in the body cavity.

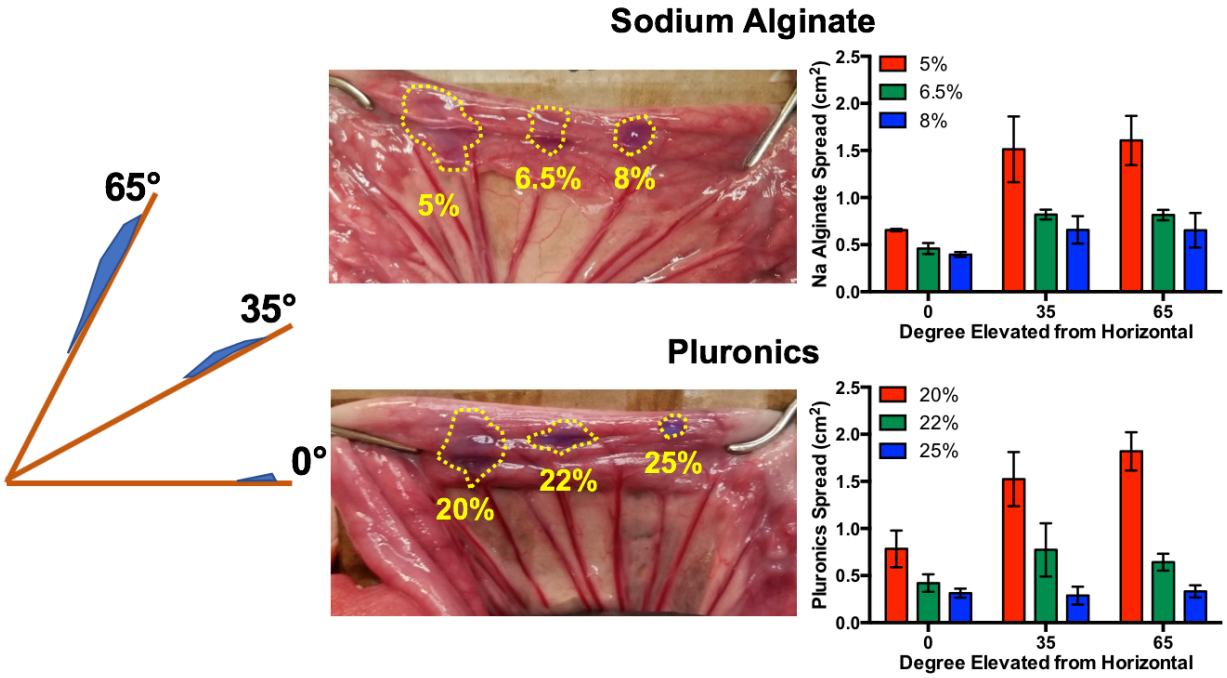

Figure 5.2: *Gel formulation viscosity assessment.* Schematic, representative images, and quantified tissue spread surface areas for the gel formulation viscosity assessment studies. Dotted lines indicate the area of tissue spread of each formulation in each representative image. Data is representative of n=3 reps per formulation and angle tested.

Direct administration method testing

Using the chosen gel formulation, the direct administration protocol was optimized to improve gel formulation staining application. First, several fluorophore concentration and incubation time parameters were tested to determine a clinically viable staining solution and method (**Fig. 5.3**). Nerve contrast remained consistent across concentrations and incubation times tested in brachial plexus and sciatic nerve models (**Fig. 5.3A**). Additionally, nerve SBR values remained relatively consistent across all concentrations and incubation times. However, fluorescence signal intensities decreased at lower concentrations and incubation times (**Fig. 5.3B**). For this reason, the highest concentration tested, 200 μg/mL, which is the highest concentration that when scaled to humans still falls within the microdosing range for eIND studies, was chosen for further studies. In order to minimize the time needed to perform the staining protocol, the one-minute incubation time was chosen for further studies.

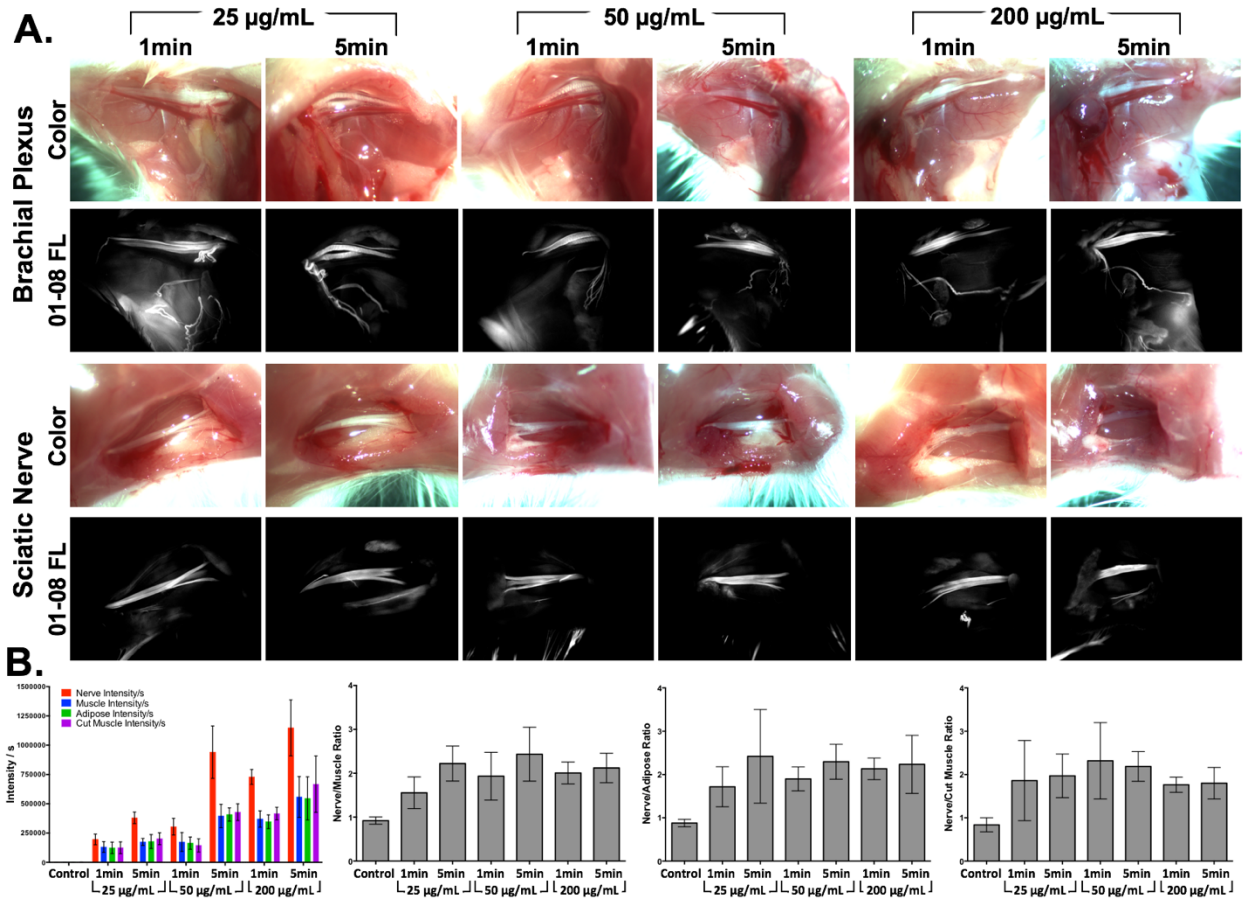

Figure 5.3: *Gel formulation direct administration staining parameter testing.* **(A)** Representative brachial plexus and sciatic nerve images and **(B)** quantified intensity and nerve SBR ratios for each concentration and incubation time tested during staining parameter testing studies. Images are representative of n=6 nerve sites. Images are displayed without normalization. FL = Fluorescence; min = minute.

With the fluorophore concentration and incubation time chosen, wash protocol parameters were altered to determine the final amount of washing and wash solution temperature. Warm (~37 ºC) and cold (~4 ºC) PBS was used to wash nerve sites stained with a 1 min incubation of 200 µg/mL LGW01-08 in 22% Pluronics formulation. Images were taken throughout the washing process to identify the final wash amount (**Fig. 5.4**). An increase in nerve signal was observed in the first 1 to 2 wash steps followed by a decrease in background muscle and adipose fluorescence in later wash steps (**Fig. 5.4A**). Quantified nerve intensities and SBRs agree with this observation for both the cold and warm washes (**Fig. 5.4B**). After 6 washes, nerve intensities and SBRs began to level off, with minimal increase out to the final 18th wash step. Thus, 6 total washes were chosen as the most clinically relevant

amount of washing. In comparing cold PBS washes to warm PBS washes, cold PBS provided minor yet not significant increases in the nerve signal intensity and nerve to adipose ratio. Therefore, the temperature of the wash solution was not deemed as an important factor in overall wash performance. Following completion of the last wash step, images were collected every 5 min out to 30 min to determine the effect of clearance on nerve signal intensities and SBRs (**Fig. 5.4C**). No significant change in nerve signal and slight yet not significant increases in the nerve SBRs occurred during this period, demonstrating the robustness of the final nerve contrast generated from direct gel formulation administration of nerve specific fluorescence.

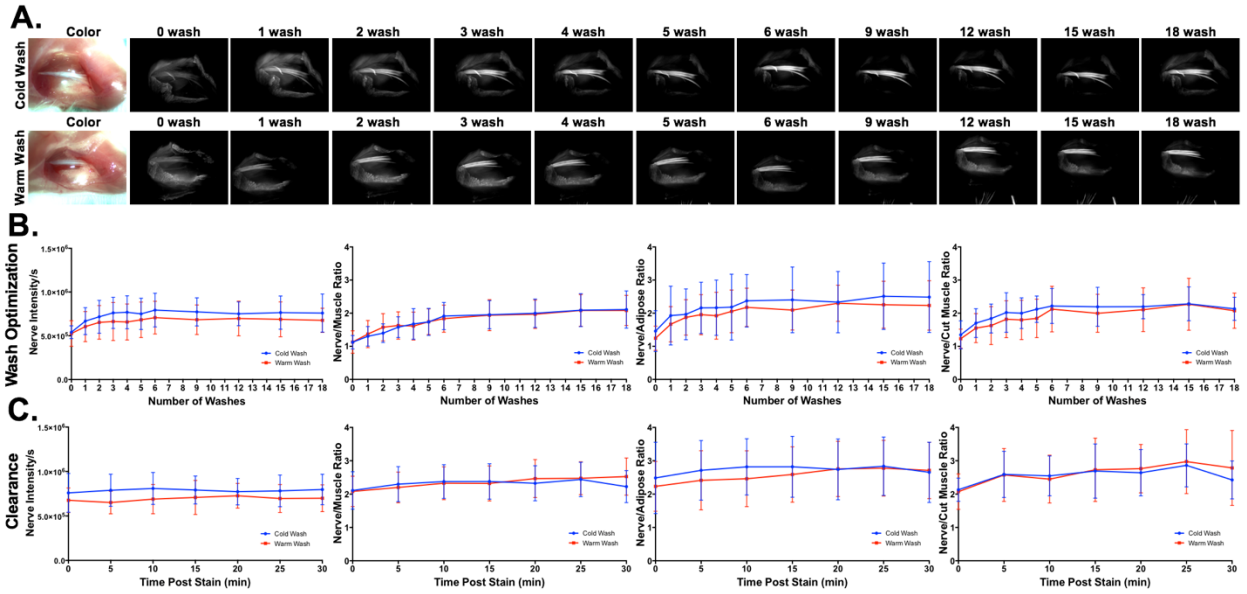

Figure 5.4: *Gel formulation direct administration washing protocol testing*. **(A)** Representative images and **(B)** quantified nerve intensities and SBRs for wash testing studies. All images are representative of data collected for n=6 nerve sites per wash temperature, with images collected at 0, 1, 2, 3, 4, 5, 6, 9, 12, 16, and 18 wash. **(C)** Nerve intensity and SBRs were calculated from images captured for 30 minutes following the final 18th wash step to visualize the effects of clearance. All quantified data is presented as mean +/- standard deviation.

Large animal studies

To compare liquid to gel formulation direct administration in a clinically relevant surgical model, swine illiac plexus nerves were stained via direct administration of Oxazine 4 formulated in the co-solvent and Pluronics formulations (**Fig. 5.5**). During staining with co-solvent formulation the surrounding tissue had to

be tented in order to collect runoff from the near vertical surface of the illiac plexus, generating significant pooling and difficulty controlling the stained area. Resulting fluorescence images, while allowing for clear identification of the main illiac nerve, contained significant background signal from areas where the stain solution had pooled. During staining with the Pluronics formulation, formulated dye was easily applied via syringe through surgical tubing passed through the assist port of the da Vinci system as a liquid and immediately gelled upon contact with the illiac plexus nerve site tissue. Resulting fluorescence images allowed clear identification of the illiac nerve as well as adjacent buried nerve tissue.

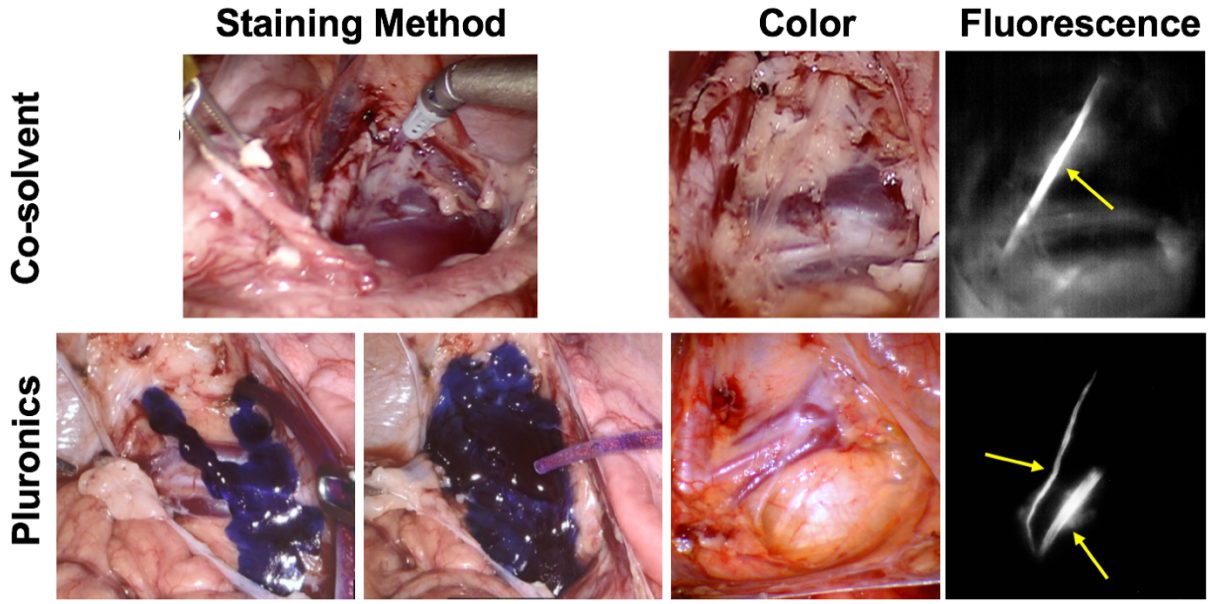

Figure 5.5: *Large animal direct administration formulation comparison.* Color and fluorescence images captured of the swine illiac plexus stained via direct administration of either co-solvent or Pluronics formulated Oxazine 4. Images of the staining method were captured during application of the formulation while color and fluorescence images were captured 2.5 hours following completion of the staining protocol.

DISCUSSION

In the present study, clinically viable gel formulations were tested using the nerve specific contrast agent LGW01-08 in order to develop a platform for enabling robust and effective direct administration methodology for nerve targeted FGS. The formulations tested, Na Alginate and F127 Pluronics, were chosen for their viscosity enhancement characteristics, clinical approval status, and beneficial fluorophore

solubilization and tissue penetration properties (**Table 5.1**). Na Alginate and Pluronics represent different classes of viscosity enhancement, with Na Alginate solidifying at colder temperatures and Pluronics solidifying at warmer temperatures such as body temperature. Na Alginate has been reported to provide excellent coverage on the applied surface and enhanced permeability via a thin hydrogel film that forms after the compound's interaction with the divalent metal ions such as Ca^{+2} present in living tissue.[164, 165] Pluronics' unique gelling characteristics, with a liquid-to-gel transition occurring when temperatures increase above a lower critical gelation threshold, make it attractive for maintaining its solidified state when applied within the body. Additionally, its surfactant characteristics improve its fluorophore solubilizing and tissue penetration potential.[166-168] Additionally, both of these formulations have been reported to provide good basis for foam formulations such as those used clinically during RP like FloSeal (Baxter, Deerfield, IL).[169-171] The range of concentrations of each of these formulating agents was chosen to span the transition from liquid at the lower end of the concentrations to solid at the higher end of the concentrations when left at room temperature.

The initial range of formulation viscosity enhancers were screened *in vivo* using the direct administration methodology previously developed for liquid based formulations. The resulting nerve fluorescence was compared to the co-solvent formulation to ensure no significant loss in nerve contrast or signal intensity occurred (**Fig. 5.1**). No significant loss in fluorescence signal vs. the co-solvent formulation was observed except at the highest concentrations of each viscosity enhancer. Fluorescence signal at all concentrations provided positive nerve SBRs, which were equivalent to the co-solvent formulation. The decrease in signal intensities at the higher concentrations of viscosity enhancer were likely due to a lower release rate of the fluorophore in the more solidified gels these concentrations created. To further test the viscosity of these formulations, the formulation ranges were tested for tissue spread at varying degrees of tilt to assess tissue hold and ease of application (**Fig. 5.2**). From these tests it was determined that the middle concentrations of each viscosity enhancer (6.5% Na Alginate and 22% Pluronics) were most clinically viable, with the lowest concentration allowing significant spread and the highest inhibiting the ability to initially spread onto the tissue. Additionally, from these tests it was determined that the unique gelling characteristics of Pluronics made it best suited for initial application in the surgical

field and subsequent hold for the duration of staining, and thus 22% Pluronics was chosen as the final base gel formulation.

With the base gel formulation chosen and its viscosity characteristics determined, Further testing of the fluorophore dose, staining incubation time, and washing protocol were needed to generate a complete gel formulation direct administration method. 200, 50, and 25 μg/mL concentrations of LGW01-08 in 22% Pluronics were used to stain nerve sites with a 1- or 5-minute incubation time to assess the interplay between fluorophore concentration and incubation time in efforts to obtain high nerve signal intensity and SBR values as well as minimize the time required to stain (**Fig. 5.3**). 50 μg/mL represents the chosen concentration for the direct administration method using liquid formulations and what was used in all initial testing experiments, while the 200 μg/mL concentration represents the maximum dose to remain beneath the microdose requirements for eIND studies.[63, 150] The 25 μg/mL concentration was tested to assess any improvements in nerve SBR from decreased dose. No significant change in nerve contrast and SBR values was observed among the different staining conditions, however nerve signal intensities were positively correlated to changes in concentration and incubation time. Thus the 200 μg/mL concentration and 1 min incubation times was chosen as final dose and stain time due to the tradeoff between a shortened staining protocol and resulting nerve signal.

Following staining parameter testing, several wash conditions were tested to determine the final wash solution and amount of washing for gel formulation application. Warm (~37 ºC) and cold (~4 ºC) PBS were tested as wash solutions through a series of flushes applied to stained nerve sites, with images collected during and following the wash protocol (**Fig. 5.4**). Both temperature wash solutions saw a steady increase in nerve intensity values in the first two wash steps and nerve SBRs values in the first 6 wash steps. The increased nerve signal is likely due to the washing process resolubilizing fluorophore in the wash solutions and allowing for further diffusion into the nerve tissue, while improvements in nerve SBRs likely represent further removal of nonspecifically bound fluorophore. It appears that for both wash solution temperatures, 6 flushes removed the majority of non-specific stain, with further washing providing marginal improvements in nerve SBR. Thus 6 wash steps were chosen as the final washing amount, bringing the overall staining protocol time down to 1-2 minutes. No major differences were observed between the warm and cold wash solutions ability to improve contrast, with the only

consistent change being the increased nerve signal from cold wash solution. This result could be due to the cold temperature wash providing improved ability to liquify any leftover Pluronics formulation and allowing for improved secondary staining during washing. These finding suggest wash solution temperature is not an important factor for wash performance, but wherever possible cold wash solution should be utilized. Additionally, clearance assessment following completion of the washing protocol saw no loss in nerve signal and slight increases in nerve SBRs out to 30 minutes. These results suggest that no significant loss in nerve signal or SBRs will occur during the course of a typical nerve sparing procedure.

The final gel formulation was compared to the co-solvent formulation in large animal screening experiments as a more clinically relevant surgical scenario. The swine illiac plexus was stained via direct administration of the two formulation during laparoscopic surgery using the da Vinci surgical robot from Intuitive Surgical and fluorescence images were captured via a custom fluorescence channel integrated into the da Vinci Si endoscope (**Fig. 5.5**). From images collected during the staining process the benefit of the gel formulation for improved stain control on the vertical surface of the illiac plexus was apparent. While the co-solvent formulation had to be contained via tenting of the surrounding tissue, the Pluronics formulation was easily applied and spread on the tissue as a liquid, but immediately gelled upon contact and was subsequently held in place throughout the incubation process. The resulting fluorescence images demonstrated the benefits of the gel formulation in improved nerve contrast and reduced background resulting from pooling of the co-solvent formulation. Additionally, the gel formulation administration enabled visualization of buried nerve structures adjacent to the illiac nerve, perhaps as a result of increased penetration depth due to increased contact time from the Pluronics gel formulation.

Through systematic optimization and characterization of viscosity enhancer amount, fluorophore concentration, staining incubation time, wash solution, and wash amount the final gel formulation and direct administration methodology developed herein can provide bright, specific nerve staining that can be applied to many tissue shapes, tilts, and morphologies in under two minutes. The Pluronics based formulation's unique physical characteristics allow for nerve-specific stain solution to be applied with relative ease as a liquid and then remain in place following near instantaneous gel formation. The resulting platform provides a clinically viable method for fluorescence guided nerve-sparing during RP and an improved route for rapid clinical translation under exploratory IND (eIND)

regulations. By requiring much less preclinical toxicology testing, eIND approval is possible with substantially less investment in time and money. We anticipate that the nerve specific FGS technology developed herein will reach clinical approval within the next 5 years, a rapid timeline for novel probes.

Chapter 6

Enhanced formulation strategies for systemic administration of nerve-specific fluorophores

ABSTRACT

Fluorescence guided surgery using near-infrared (NIR) optical imaging technology is capable of wide-field, real-time visualization of targeted tissues intraoperatively with high specificity and sensitivity. Nerve-specific small molecule fluorophores could enable vastly improved nerve identification and thus sparing rates to improve surgical outcomes. A novel NIR oxazine fluorophore, LGW01-08, has demonstrated high nerve specificity following systemic administration in preclinical mouse models, making it an attractive candidate for clinical translation. However, a more clinically viable formulation than the previously utilized co-solvent formulation is needed. We have developed and screened a series of clinically relevant formulations for systemic administration of LGW01-08, with a DSPE-PEG micelle formulation chosen as the most clinically relevant vehicle for administration. Toxicology, pharmacokinetics, and pharmacodynamics parameters were also characterized for the chosen formulation. Clinically relevant imaging time points and doses were identified and maximum tolerated dose, drug release kinetics and biodistribution characteristics were determined for DSPE-PEG micelle formulated LGW01-08 injections. The resulting fluorophore formulation provides a strong basis for further testing in large animals and clinical translation.

INTRODUCTION

Fluorescence guided surgery (FGS) has the potential to revolutionize surgery and improve nerve sparing outcomes by allowing direct visualization of nerve tissues intraoperatively. Recent work has generated novel near-infrared nerve specific fluorophores for clinical translation to FGS (**Chapter 4**). From these compounds, LGW01-08 was chosen as the lead compound for advancement to clinical studies. Additionally, a clinically viable direct administration formulation and methodology has been developed for rapid initial translation through an eIND for proof of concept first-in-human clinical trials (**Chapter 3**). However, systemic administration would provide improved nerve-specific imaging guidance as compared to direct administration in some circumstances, such as when nerve identification is required prior to incision or the nerve areas are not accessible for staining.

Although LGW01-08 has been shown to demonstrate high nerve specificity and adequate fluorescence signal for real time imaging following systemic administration, previous studies have been conducted utilizing a laboratory grade co-solvent formulation as a vehicle for intravenous injection (**Chapter 3**).[20, 63] The co-solvent formulation is only stable at room temperature for <30 minutes, cannot solubilize concentrations above 5mg/mL, and requires the use of dimethyl sulfoxide and Kolliphor EL as solubilizing agents, which will hamper clinical translation due to vehicle induced toxicity issues. Therefore, a clinically viable formulation with FDA approval is needed for intravenous injection of nerve-specific fluorophores for FGS.

In the present study, we developed and characterized clinically relevant formulation strategies for intravenous injection of LGW01-08. We identified a formulation for delivery of this promising nerve-specific fluorophore that has improved stability compared to the co-solvent formulation and already has FDA approval for several clinical applications. Additionally, toxicity testing, pharmacokinetics, and dose ranging studies were carried out to determine important pharmacological properties of the novel fluorophore/formulation combination and determine final dose and imaging time points for clinical studies. The work presented herein provides an extensive framework for clinical translation of this

promising nerve-specific contrast agent to improve nerve identification intraoperatively.

MATERIALS & METHODS

Contrast agents and formulations

Oxazine 4 perchlorate was obtained from Exciton (Lockbourne, OH). LGW01-08 was chosen as the lead compound for development from a library of 64 oxazine derivatives synthesized in the Gibbs laboratory by Dr. Lei Wang. All synthesis, purification, and characterization of the novel fluorophore was carried out by Dr. Wang at the OHSU and PSU campuses. The previously used co-solvent formulation containing 10% dimethyl sulfoxide (DMSO), 5% Kolliphor EL, 65% serum, and 20% phosphate buffered saline (PBS) was used for comparison to the clinically viable formulations presented herein.[20] Distearyl-phosphatidylethanolamine-PEG2000 (DSPE-PEG) micelle, F-127 micelle, liposome, and (2-Hydroxypropyl)-β (HP-β) cyclodextrin formulations were prepared by Dr. Vidhiben Shah in the Alani laboratory. All encapsulation, purification, and characterization of the novel formulations was carried out by Dr. Shah at the OHSU and OSU campuses.

Animals

Approval for the use of all animals in this study was obtained from the Institutional Animal Care and Use Committee (IACUC) at Oregon Health and Science University (OHSU). Male CD-1 mice weighing 22-24g were purchased from Charles River Laboratories (Wilmington, MA). Prior to surgery, mice were anaesthetized with 100 mg/kg ketamine and 10 mg/kg xylazine (Patterson Veterinary, Devens, MA) administered intraperitoneally (IP).

Formulation nerve-specificity screening

Each formulation was initially screened in mice via systemic administration per the kinetics and dose determined for several small molecule nerve-specific

fluorophores in the co-solvent formulation.[20, 63, 66, 74] 200 nmol of LGW01-08 in 100 µL of each tested formulation was administered intravenously. Intravenous administration was performed 4 hours prior to nerve imaging, which had been shown previously to provide the highest nerve to background tissue fluorescence ratio for Oxazine 4 and several other nerve specific fluorophores.[20, 63, 74] Uninjected animals were used for all control images (n=3 mice or 12 nerve sites/formulation).

Maximum tolerated dose studies

The maximum tolerated dose (MTD) was determined in mice for LGW01-08 in the top formulation from initial nerve specificity testing, DSPE-PEG micelles. The MTD was determined as half of the lowest lethal dose in mice, with injected doses starting at 12 mg/kg, decreasing by half until 3 mg/kg was reached. Following determination of the MTD, two cohorts of mice per formulations were administered formulated LGW01-08 for blood chemistry analysis and 14-day weight monitoring (n=5 mice per cohort per formulation). Blood chemistry cohort mice were euthanized 24 hours following systemic administration and blood was collected into lithium heparin tubes via cardiac puncture. Blood was also collected following the 14-day weight monitoring studies. Blood was sent to IDEXX laboratory (Veterinary Diagnostic, Portland, OR) for standard blood chemistry analysis. The blood markers evaluated include blood urea nitrogen (BUN), creatinine kinase (CK), alanine transaminase (ALT), aspartate transaminase (AST), and alkaline phosphatase (ALP). Hematological analysis involves assessment of white blood cell (WBC) count, red blood cell (RBC) count, Hematocrit (HC), % neutrophils, % lymphocyte, % monocyte, % eosinophil, and % basophile. The electrolytes assessed include phosphorus, calcium, sodium, potassium, and chloride. Weight monitoring cohort mice were weighed 1, 2, 3, 5, 7, 9, 11, 13, and 14 days following systemic administration.

Pharmacokinetics, biodistribution, and dose response

Imaging and drug release pharmacokinetics (PK) and biodistribution (BioD) studies were completed in mice using the top formulation from the initial testing, DSPE-PEG micelles, as well as the previously utilized co-solvent formulation for equivalent comparison. Formulated LGW01-08 was injected at a 2 mg/kg dose and

blood collection was completed at the time points of 0, 0.5, 1, 2, 4, 8, and 24 hours post injection (n=5 mice per time point per formulation). Following blood collection via cardiac puncture, fluorescence and color images were acquired of the brain, lungs, liver, stomach, intestines, pancreas, spleen, kidney, bladder, brachial plexus, and sciatic nerves (n=3 mice per time point per formulation). Additionally, brain, lung, heart, liver, and kidney tissues were collected for liquid chromatography tandem mass spectroscopy (LCMS/MS) biodistribution analysis (n=5 mice per time point per formulation).

With the clinical imaging time point determined for each formulation, dose response pharmacodynamic (PD) studies were completed in mice for the DSPE-PEG micelle formulation using a dose range up to the MTD: 1.5, 2, 2.5, and 3 mg/kg (n=3 mice per dose per formulation). Nerve imaging was completed 2 hours following injection since this was determined to be the time point chosen for nerve contrast in the PK studies.

Intraoperative Fluorescence Imaging Systems

A custom-built small animal imaging system capable of real-time color and fluorescence imaging was used to acquire rodent *in vivo* images. The imaging system consisted of a QImaging EXi Blue monochrome camera (Surrey, British Columbia, CA) for fluorescence detection with a removable Bayer filter for collecting co-registered color and fluorescence images. A PhotoFluor II light source (89 North, Burlington, VT) was focused onto the surgical field through a liquid light guide and used unfiltered for white light illumination. For fluorescence excitation, the PhotoFluor II was filtered with a 620 ± 30 nm bandpass excitation filter. Resulting fluorescence was collected with a 700 ± 37.5 nm bandpass emission filter for image collection. All filters were obtained from Chroma Technology (Bellows Falls, VT). Camera exposure times ranged from 10 – 2000 ms for fluorescence image collection.

Intraoperative Nerve and Biodistribution Imaging and Image Analysis

Nerve specific contrast and tissue biodistribution intensities were assessed for all initial testing, PK, BioD, and PD studies using the intraoperative fluorescence imaging systems to collect images of the nerves and surrounding tissue as well as

the additional tissues for biodistribution assessment. Additional unstained control animals were imaged to assess tissue autofluorescence.

Custom written MatLab code was used to analyze the tissue specific fluorescence where regions of interest were selected using the white light images. These regions of interest were then analyzed on the co-registered matched fluorescence images permitting assessment of the mean tissue intensities and nerve signal to background ratios. Intensity measurements were divided by the exposure time to obtain normalized intensity per second measurements.

Statistical Analysis

Significant differences between nerve SBR means were evaluated using a one-way ANOVA followed by a Fisher's LSD multiple comparison test with no assumption of sphericity using the Geisser-Greenhouse correction to compare all mean nerve to background tissue ratios. The α value was set to 0.05 for all analyses. Results were presented as mean ± standard deviation (S.D.). All statistical analysis was performed using GraphPad Prism (La Jolla, CA).

RESULTS

Initial nerve specificity testing

Clinically relevant formulation strategies were tested as viable alternatives to the co-solvent formulation for systemic administration of nerve contrast agents for FGS. Cyclodextrin, F127 micelles, DSPE-PEG micelles, and liposomes were used to solubilize Oxazine 4 and LGW01-08 nerve contrast agents for injection using the previously published dose and imaging window for nerve-specific oxazine fluorophores.[63, 74] The resulting nerve contrast was imaged and compared to the co-solvent formulation (**Fig. 6.1**). Tissue-specific fluorescence signal intensities varied between the tested formulations, with DSPE-PEG micelles providing the highest intensity nerve signal, which was roughly equivalent to the nerve signal intensity provided by the co-solvent formulation for both Oxazine 4 (**Fig. 6.1A & 6.1B**) and LGW01-08 (**Fig. 6.1C & 6.1D**). Notably, only the cyclodextrin and DSPE-PEG micelle formulations provided equivalent nerve to muscle SBRs to the co-solvent

formulations for Oxazine 4. While the cyclodextrin, DSPE-PEG micelle, and F127 micelle formulations provided equivalent nerve to muscle SBRs to the co-solvent formulations for LGW01-08. Based on these results, the DSPE-PEG micelle formulation was chosen for further characterization and testing.

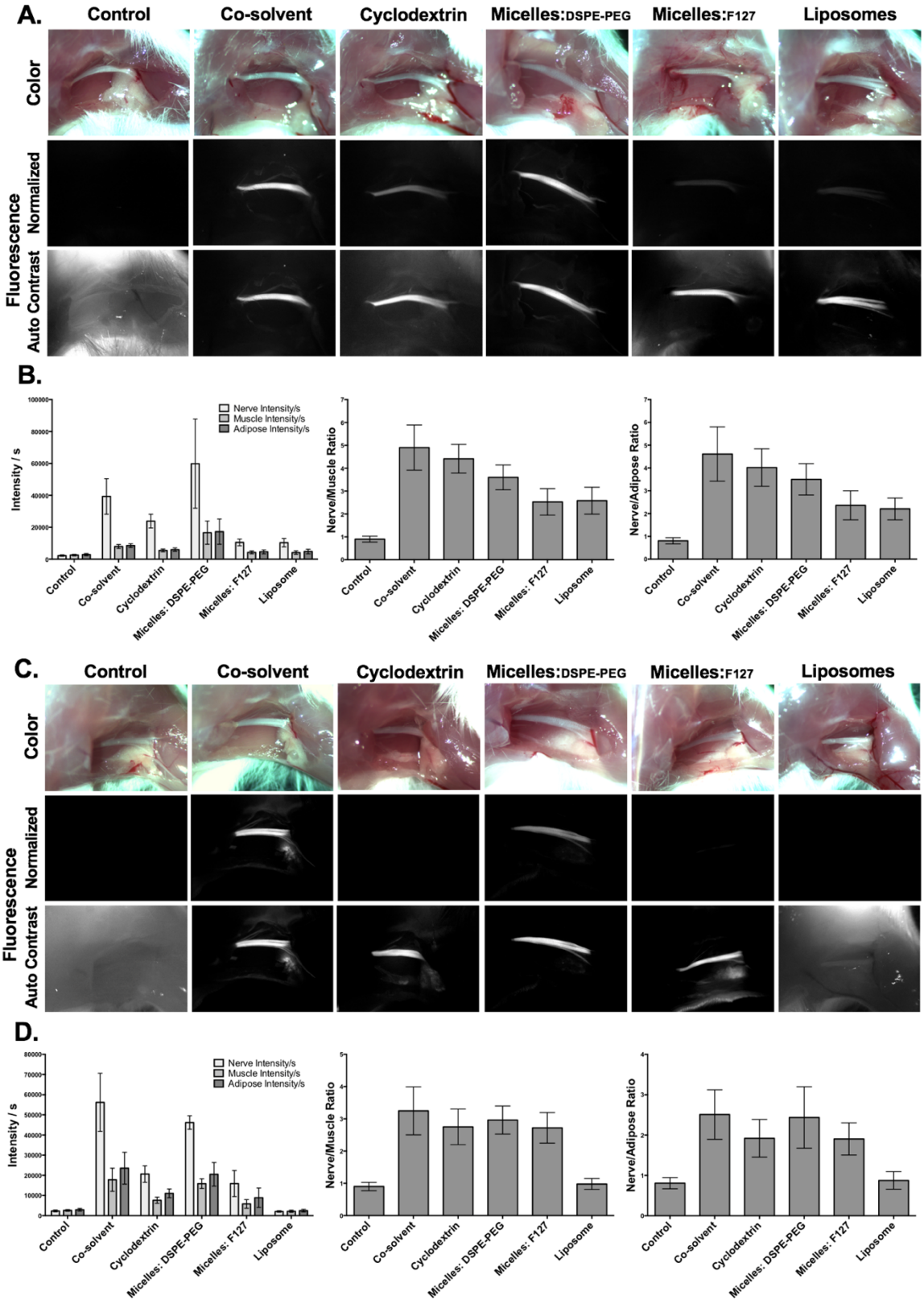

Figure 6.1: *Clinically viable systemic administration formulation initial screening.* **(A)** Representative images and **(B)** quantification for Oxazine 4 using the varied formulation strategies

in murine models. **(C)** Representative images and **(D)** quantification for LGW01-08 using the varied formulation strategies in murine models. All images are representative of data collected for n=12 nerve sites per formulation. All quantified data is presented as mean +/- standard deviation.

Formulation composition, stability, and clinical status

The formulations tested herein were chosen for their high stability, FDA approval status, clinical relevance and advantageous uptake characteristics. The composition, stability, and clinical toxicity profiles are outlined in **Table 6.1**. All formulations are stable for at least 48 hours and can be freeze dried for long term storage, while the co-solvent formulation is stable for less than 30 minutes and has no freeze-drying capability. Additionally, all novel formulations possess FDA approval aside from the PEG-PLA micelles, which are under clinical development in the US and approved in Korea.

Table 6.1: *Clinically viable formulation composition, stability, freeze-drying characteristics, and regulatory status*

Formulation	Composition	Solution stability	Freeze-drying capability	Regulatory status
Cosolvent	10% DMSO, 5% Kolliphor, 85% 75/25 Serum/Buffer	<30 min	No	None
Liposome	Sphingomyelin/cholesterol	48 h	Yes - with cryoprotectant	FDA Approved
Micelle	DSPE-PEG (2K)	72 h	Yes – with/without cryoprotectant	FDA Approved
Micelle	Pluronic F-127	48 h	Yes – with/without cryoprotectant	FDA Approved
Micelle	PEG-PLA (2k-1.8k)	120 h	Yes – with/without cryoprotectant	Under clinical development in US, approved in Korea
Cyclodextrin	(2-Hydroxypropyl)-β-cyclodextrin	72 h	Yes – without cryoprotectant	FDA Approved

Rodent toxicology testing

Toxicology testing was performed in rodents for the chosen DSPE-PEG micelle formulation with LGW01-08 to determine the maximum tolerated dose (MTD), assess any changes in blood chemistry following systemic administration and screen for any long-term toxicity effects. The mouse MTD was determined to be 3 mg/kg for the DSPE-PEG micelle formulation following decreases in dose by

half starting from a lethal dose of 12 mg/kg. This determined MTD was administered to assess any blood chemistry changes and effect on 14-day weight gain (**Fig. 6.2**). Blood markers for kidney (blood urea nitrogen (BUN) and creatine kinase (CK)) and liver (aspartate transaminase (AST) and alkaline phosphatase (ALP)) toxicity were at normal levels in all cases except for CK and AST at one day post injection (**Fig. 6.2A**). However, both CK and AST levels returned to normal by 14 days post administration. Blood electrolyte amounts were within the normal range except for phosphorus levels at one and 14 days post injection (**Fig. 6.2B**). Hematological analysis for white blood cell (WBC) count, red blood cell (RBC) count, % lymphocytes, % neutrophils, % monocytes, and % eosinophils returned to normal values except for WBC levels in the control and one day post injection groups (**Fig. 6.2C**). Following administration of the MTD, mice displayed normal, healthy weight gain during the 14-day monitoring period (**Fig. 6.2D**).

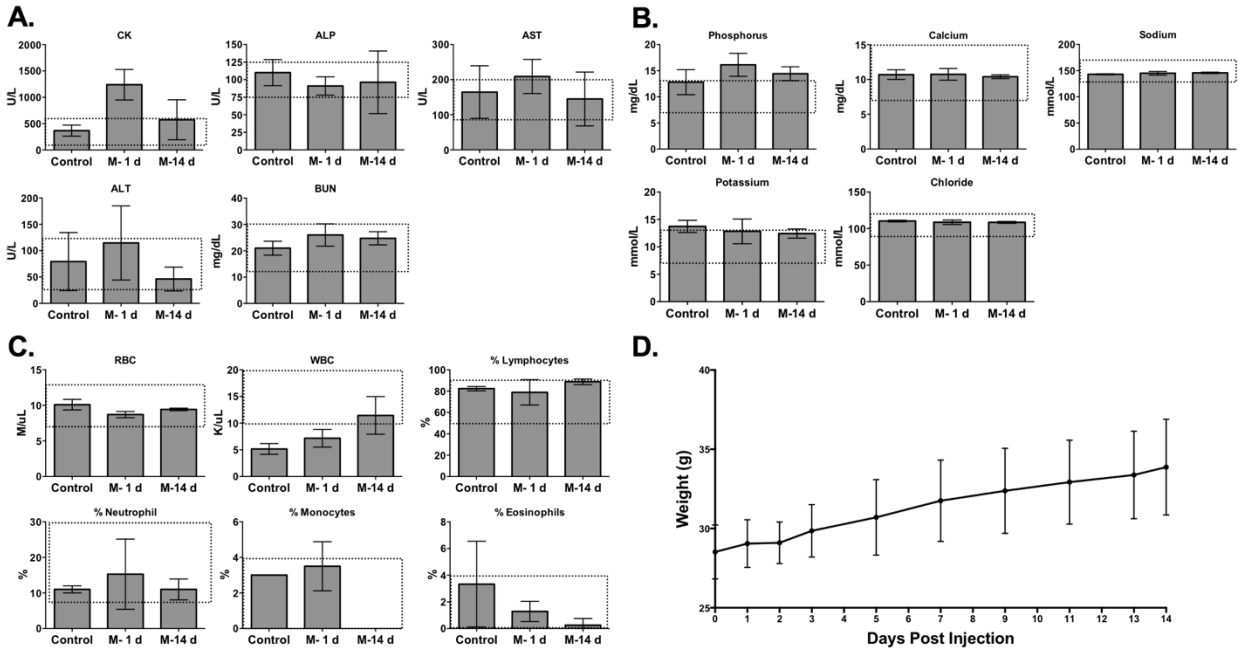

Figure 6.2: *DSPE-PEG Micelle toxicology testing*. **(A)** Blood marker, **(B)** electrolyte, and **(C)** hematological analysis results represented as concentrations (Units per liter (U/L)), milligram per deciliter (mg/dL), millimole per liter (mmol/L), mole per microliter (M/μL), kilo per microliter (K/μL) or percentages following administration of the maximum tolerated dose (MTD, 3 mg/kg). The dashed line boxes on each graph represent the normal expected range of values. **(D)** The measured mean weights for mice 14 days following administration of the MTD. All data are representative of data collected for n=5 mice per formulation. All quantified data is presented as mean +/- standard deviation. CK = creatine kinase; ALP = alkaline phosphatase; AST = aspartate

transaminase; ALT = alanine transaminase; BUN = blood urea nitrogen; RBC = red blood cell; WBC = white blood cell; M – 1 d = measured values one day post injection; M – 14 d = measured values 14 days post injection.

Pharmacokinetics, biodistribution, and imaging time course studies

To further assess co-solvent vs. DSPE-PEG micelle formulated LGW01-08 uptake *in vivo* and optimize the imaging time point for FGS applications pharmacokinetics (PK), biodistribution (bioD), and imaging time course studies were performed using a 2mg/kg dose. Fluorophore uptake was determined using LCMS/MS analysis of murine blood and tissue collected at 0, 0.5, 1, 2, 4, 8, and 24-hour time points to quantify kinetics and tissue biodistribution (**Fig. 6.3A & 6.3B**). LGW01-08 blood concentrations dropped quickly in both formulations with micelles showing increased release at 2- and 4-hour time points as compared to the co-solvent formulation. The terminal rate constant (λ_z), elimination half-life ($t_{1/2}$), total area under the plasma concentration-time curve (AUC_{inf}), and total body clearance of drug from plasma (CL) values calculated from each formulation's curves were roughly equivalent. The volume of distribution during the terminal phase (V_z) values were 1.65 times higher for the co-solvent formulation compared to the DSPE-PEG micelle formulation (**Fig. 6.3A**). Tissue concentration levels followed a similar trend to blood concentration levels, with the most LGW01-08 cleared from the tissue by 4 hours post injection and high levels in highly blood perfused tissues like heart, lung and brain falling rapidly after injection as expected under normal clearance conditions (**Fig. 6.3B**).

Brachial plexus and sciatic nerve images were also collected to assess nerve contrast and identify the most clinically viableimaging time point (**Fig. 6.3C & 6.3D**). Interestingly, nerve uptake occurred immediately following systemic administration and nerve contrast was observed as soon as 30 min following injection which was maintained for up to 8 hours for both the co-solvent and DSPE-PEG micelle formulations (**Fig. 6.3C**). Nerve fluorescence signal intensities decreased significantly in the first two hours following injection, with fluorescence signal intensities falling close to baseline autofluorescence levels 24 hours after systemic administration of LGW01-08 in either formulation (**Fig. 6.3C & 6.3D**). Background tissue (muscle and adipose) fluorescence signal intensities decreased at a greater rate in the first two hours post LGW01-08 administration, resulting in

increasing nerve to muscle and nerve to adipose SBRs. Nerve to muscle ratios were roughly equivalent for all formulations out to four hours post systemic administration, with DSPE-PEG micelle formulation showing a faster increase and more sustained maximum contrast ratio at the one- and two-hour time points compared to the co-solvent formulation. Nerve to adipose ratios were roughly equivalent between the co-solvent and DSPE-PEG micelle formulations. Nerve SBRs peaked at two hours post injection and thus the two-hour time point was chosen as the most clinically viable imaging time point.

In addition to nerve, muscle, and adipose tissues, brain and lung tissues were also imaged and fluorescence signal intensities were measured for biodistribution and kinetics assessment (**Fig. 6.3E**). Notably, fluorescence signal intensities in the lung and brain tissues followed a similar trend to the nerve tissue fluorescence intensities, with signal decreasing significantly in the first two hours for both formulations. High uptake in lung tissue immediately following injection was evident and agrees with the results from the LCMS/MS tissue biodistribution analysis (**Fig. 6.3B & 6.3E**).

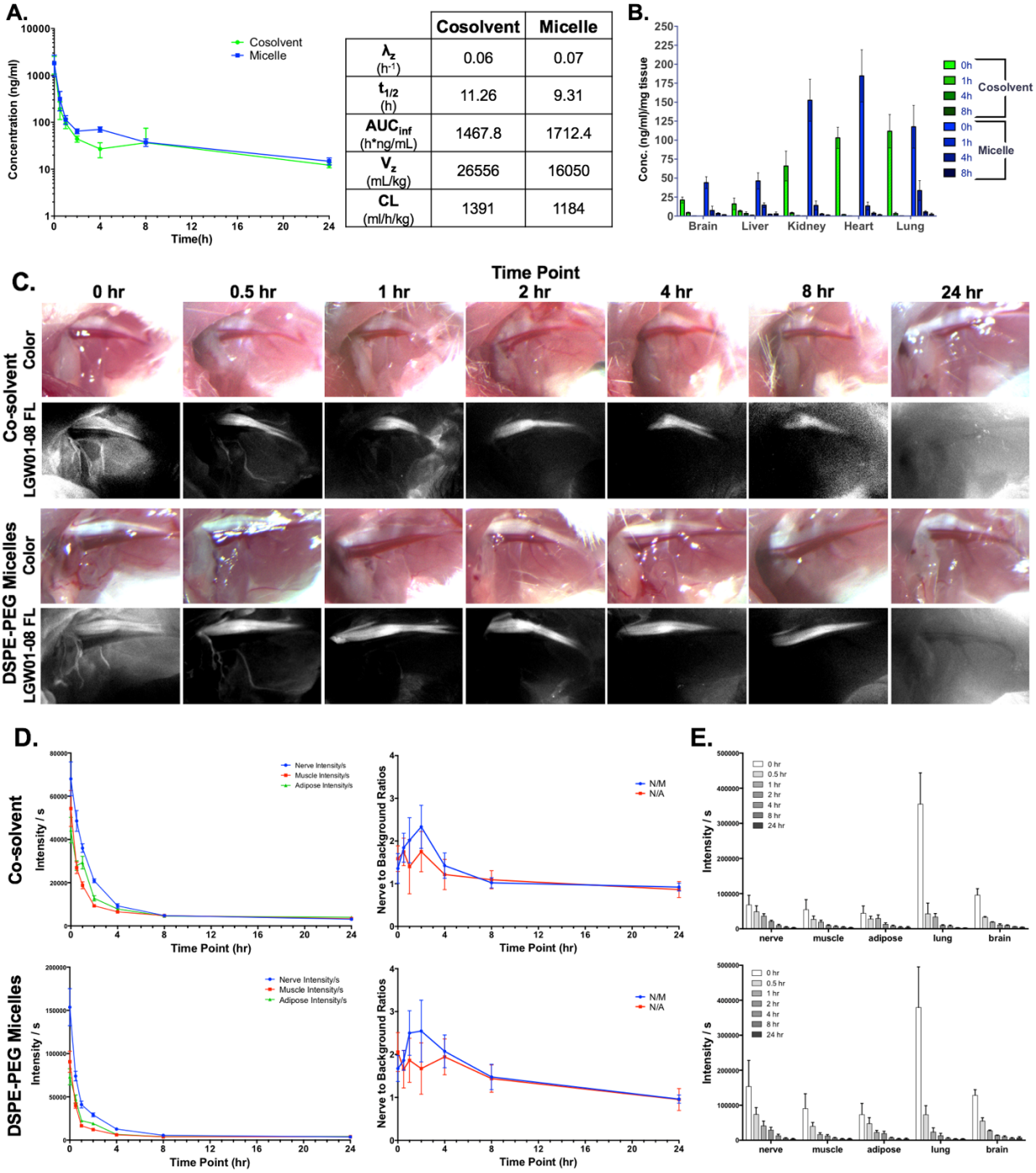

	Cosolvent	Micelle
λ_z (h^{-1})	0.06	0.07
$t_{1/2}$ (h)	11.26	9.31
AUC_{inf} (h*ng/mL)	1467.8	1712.4
V_z (mL/kg)	26556	16050
CL (ml/h/kg)	1391	1184

Figure 6.3: *DSPE-PEG micelle vs. co-solvent pharmacokinetics and biodistribution*. **(A)** The blood LGW01-08 concentrations and release kinetics and **(B)** LCMS/MS tissue biodistribution of DSPE-PEG micelles vs. co-solvent administered LGW01-08. **(C)** Representative nerve images, **(D)** fluorescence signal intensities and nerve SBRs, and **(E)** fluorescence tissue biodistribution for co-solvent and DSPE-PEG micelle formulated LGW01-08. All animals were systemically administered LGW01-08 at 2 mg/kg and imaged at 0, 1, 2, 4, 8, and 24 hours post injection. All images are representative of data collected for n=12 nerve sites or n=5 mice per formulation. All

quantified data is presented as mean +/- standard deviation. λ_z = Terminal rate constant; $t_{1/2}$ = elimination half-life; AUC_{inf} = total area under the plasma concentration-time curve; CL = total body clearance of drug from plasma; V_z = Volume of distribution during terminal phase.

Dose ranging pharmacodynamics imaging studies

Following determination of the nerve imaging time point for each formulation, dose scaling studies were performed to determine the most clinically viable dose for injection of LGW01-08 in the DSPE-PEG micelle formulation. 1.5, 2, 2.5, and 3 mg/kg doses were administered, followed by collection of fluorescence images of the brachial plexus and sciatic nerves two hours post injection to assess the resulting nerve contrast (**Fig. 6.4**). Nerve fluorescence intensity values were highest at the 2.5 mg/kg dose, decreased slightly at the 3 mg/kg dose, and were roughly equivalent at the lower doses in the 1.5 and 2 mg/kg groups (**Fig. 6.4A)**. No significant difference in nerve SBRs was observed across all tested doses (**Fig. 6.4B)**.

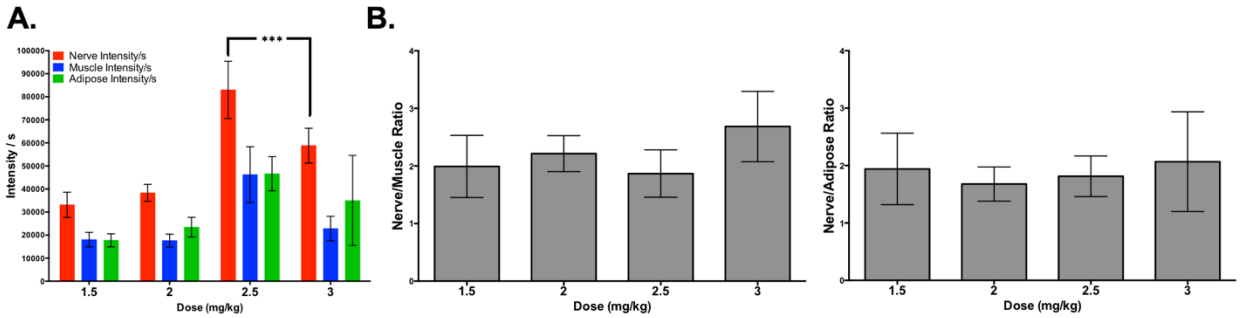

Figure 6.4: *DSPE-PEG micelle pharmacodynamic dose response*. **(A)** The quantified tissue intensity and **(B)** nerve SBR values for 1.5, 2, 2.5, and 3 mg/kg doses of LGW01-08 in DSPE-PEG micelles from images collected 2 hours following injection. The means were calculated from n=12 nerve sites per dose. All quantified data is presented as mean +/- standard deviation. Nerve intensity means were compared between the 2.5 and 3 mg/kg doses to test for significance. *** = p value < 0.001.

DISCUSSION

Clinically relevant formulation strategies were tested for systemic administration of a novel NIR nerve specific fluorophore, LGW01-08, with the ultimate goal of determining a viable formulation for clinical translation of this

promising agent for nerve sparing FGS. A range of formulations with clinical approval or under clinical development (**Table 6.1**) were chosen to compare nerve labelling performance to the previously utilized co-solvent formulation with both Oxazine 4 and LGW01-08 (**Fig. 6.1**). The formulations were chosen for their high stability, storage potential, and clinical use. A liposomal formulation (Sphingomyelin), several micelle formulations (DSPE-PEG, Pluronics, PEG-PLA), and a cyclodextrin formulation (HP-β) were tested. Importantly, all formulations had improved stability when compared to the co-solvent formulation, with all solution stabilities greater than or equal to 48 hours (**Table 6.1**). Additionally, the tested formulations can all be freeze dried, allowing for extended storage potential. With all chosen formulations possessing either FDA approval or in the process of clinical development, these formulations represent excellent candidates as vehicles for clinical administration of LGW01-08. Upon initial screening of each formulation, the DSPE-PEG micelle formulation provided the best performance, with equivalent to greater fluorescence signal intensities compared to the co-solvent formulation for Oxazine 4 and LGW01-08 injections and equivalent nerve SBRs compared to the co-solvent formulation for LGW01-08 injections (**Fig. 6.1**). Thus, the DSPE-PEG micelle formulation was chosen and utilized in further testing.

With a clinically viable formulation chosen, aspects of the formulated fluorophore's toxicity, pharmacokinetics, and dose response were tested. Maximum tolerated dose (MTD) studies were performed to determine the dose-limiting toxicity of the formulated fluorophore and any changes in blood chemistry levels and long-term weight gain following systemic administration in mice (**Fig. 6.2**). Most blood chemistry markers remained within their normal range one and 14 days following injection at the determined MTD of 3mg/kg (**Fig. 6.2A, 6.2B, & 6.2C**). Blood markers for heart (Creatine Kinase, CK) and liver (aspartate transaminase, AST) toxicity were elevated at one day post injection. However, these markers are often elevated due to the stress caused by injections and values returned to normal levels 14 days post injection (**Fig. 6.2A**). Nonetheless, an extended exposure toxicology study should be performed, with complete histological analysis of each tissue following a regiment of regular doses. Among blood electrolytes, phosphorus levels were high at both time points following injection, however all other electrolyte levels were normal following injection (**Fig. 6.2B**). In hematological analysis, white blood cell levels were low at baseline in both the control and DSPE-PEG micelle administered group one day following injection, however these levels returned to the

normal range 14 days post injection (**Fig. 6.2C**). Additionally, mice showed normal continual weight gain when monitored out to 14 days following injection and no abnormal behavioral or physiological symptoms were observed (**Fig. 6.2D**). Therefore, while some blood markers showed elevated levels shortly after injection, no major or long-term toxicity issues were detected for the DSPE-PEG micelle/LGW01-08 drug formulation.

Pharmacokinetics and biodistribution studies were completed with a 2 mg/kg dose at 0, 0.5, 1, 2, 4, 8, and 24-hour time points to evaluate drug release kinetics and tissue uptake in comparison to the co-solvent formulation and to determine the most clinically relevant imaging time point (**Fig. 6.3**). LGW01-08 blood concentration levels and nerve, muscle and adipose tissue fluorescence intensity values agreed well with one another and matched closely between the co-solvent and DSPE-PEG micelle formulations (**Fig. 6.3A & 6.3D**). All drug kinetic parameters were roughly equivalent between both formulations except for the volume of distribution during terminal phase (V_z), which was 1.65 times higher in the co-solvent formulation injected animals as compared to the DSPE-PEG micelle formulation injected animals (**Fig. 6.3A**). The discrepancy in V_z values is likely due to increased clearance of the co-solvent formulated drug, which is more readily broken down in the blood stream. Tissue biodistribution levels followed the expected trend for intravenously administered drugs, with high levels in highly blood perfused organs at initial time points followed by rapid decrease and no prolonged uptake or binding in any major organs (**Fig. 6.3B).** The fluorescence imaging biodistribution analysis data agreed with these findings (**Fig. 6.3E**). Fluorescence imaging time-course studies found that two hours post injection was the time point that generated the highest nerve contrast for both the DSPE-PEG micelle and co-solvent formulated LGW01-08 (**Fig. 6.3C & 6.3D**). Interestingly, the micelle formulation provided a slightly faster increase to peak nerve to muscle ratios at the one-hour time point, which was sustained at two hours post injection. Two hours was chosen as the most clinically relevant imaging time point for systemic administration of DSPE-PEG micelle formulated LGW01-08.

With a clinical imaging time point chosen, pharmacodynamics dose ranging studies were performed to determine the clinical dose for FGS. Doses ranged from half the MTD at 1.5 mg/kg up to the MTD at 3 mg/kg (**Fig. 6.4**). No obvious trend was observed in nerve SBRs as doses were varied with nerve to muscle ratios slightly increased at 3 mg/kg (**Fig. 6.4B**) and signal intensities followed a rough increase as

dose increased, however intensities at 3 mg/kg were slightly lower that at 2.5 mg/kg (**Fig. 6.4A**). Due to the tradeoff between signal intensities and nerve SBR values and to avoid any potential toxicity issues from dosing at the MTD, 2.5 mg/kg was chosen as the most clinically viable dose (**Fig. 6.4C**).

In the present study, clinically relevant formulations strategies were explored to determine a viable formulation for clinical translation of nerve specific FGS enabled via systemic administration of the novel oxazine fluorophore LGW01-08. The chosen DSPE-PEG micelle formulation provided equivalent probe delivery and nerve contrast to the previously utilized co-solvent formulation, is stable for 72 hours and capable of freeze drying for long-term storage, and is FDA approved for a number of applications.[172, 173] Further testing in large animal models is needed to confirm translation of these positive findings and complete toxicity testing will need to be carried out to enable clinical trials. The work presented herein has yielded a platform for clinical translation of this promising nerve specific fluorophore and provided insight into the pharmacological properties of DSPE-PEG micelle formulated oxazine compounds.

Chapter 7

Summary and Future Perspectives

SUMMARY

The main goals of surgery are to repair or remove diseased or damaged tissue(s), while preserving intact vital structures. However, despite many recent advancements in surgical technique and preoperative diagnostic imaging technologies, the majority of intraoperative surgical guidance is performed unaided with only the basic tools of white light visualization and palpation.[6-11] Fluorescence guided surgery (FGS) technologies have the potential to revolutionize surgery, improving surgical outcomes through enhanced visualization of tissues for resection, such as tumors, or preservation, such as nerves or vasculature. Utilizing compact and relatively low-cost imaging systems, FGS can be readily implemented into many procedures to bridge the gap between preoperative imaging and intraoperative reality.[15-23]

Fluorescence has been used in surgery as far back as 1948, when Moore *et. al.* reported on the use of fluorescein sodium to guide brain tumor resection.[174] However, intraoperative guidance technologies did not gain more attention until the 1990s, when near-infrared (NIR) fluorescence agents like indocyanine green (ICG) and methylene blue started to be used as vascular tracers.[175-178] With NIR fluorescence, ICG and methylene blue are capable of visualizing highlighted tissues at centimeter depths and without autofluorescence background from unstained tissues. Additionally, fluorescein, ICG, and methylene blue are approved by the FDA for clinical use, allowing for off-label FGS applications. Thus, ICG, methylene blue, and in some cases, fluorescein have seen widespread adoption and use in many FGS applications. However, as blood pool agents with no specific tissue targeting, these agents are limited in application and rely on the enhanced permeability and retention (EPR) effect to generate contrast in tumor tissue for application to tumor resection. Additionally, while useful for vascular identification, none of these fluorophores have demonstrated nerve targeting for use with nerve sparing FGS applications. Thus, to wield the full power of FGS, there remains a great need for novel fluorescence contrast agents to reach FDA approval status and clinical use.

This thesis focuses on the development of novel tumor and nerve targeted probes for FGS as well as the development of more clinically viable administration strategies and formulations to improve the potential for clinical translation of these promising technologies. Novel contrast agents such as those developed herein face

a challenging clinical translation pathway. As non-curative diagnostic agents that often only require a single administration, navigating traditional drug pathways is difficult due to the immense financial and time requirement to gain investigational new drug (IND) approval and a reduced financial incentive for large pharmaceutical companies.[40, 41] Recently, some groups have developed and utilized exploratory investigational new drug (eIND) pipelines to speed up and reduce the cost of clinical translation for novel FGS probes.[41, 43, 44, 150] eIND studies require minimal preclinical toxicity testing by utilizing microdoses in first-in-human clinical trials, allowing for clinical translation of novel probes to be feasible in a limited funding environment. The work presented herein has sought to utilize this promising pathway by developing direct administration methodologies that require substantially lower doses than traditional systemic administration methods. Additionally, direct administration allows for increased selectively in tissue staining and its principles can even be applied on resected specimens to provide diagnostic guidance with no potential patient toxicity. In this thesis, these concepts have motivated the development of direct staining methodologies for novel tumor and nerve specific fluorescent probes. Additionally, improved formulation strategies were developed to enhance both direct and, for cases where direct administration is not possible and/or whole-body staining is preferred, systemic administration.

Tumor margin status is an important prognostic factor for any tumor resection.[12, 45-47] Involved or close margins are a major problem for breast conserving surgery patients, requiring re-excision at rates up to 60%.[2, 12] In **chapter 2** a novel dual probe direct staining methodology was developed for imaging tumor margin in excised tumor specimens. Using a dual probe difference specimen imaging (DDSI) approach, excised orthotopic breast cancer tumor specimens were stained along with normal adipose tissue, facilitating correction for any nonspecific uptake. The final methodology provided highly sensitive and tumor biomarker specific contrast in a platform that can be applied outside the patient, resulting in no potential patient toxicity and significantly improved clinical translation potential.

Based on the success of the direct administration method developed for tumor targeted antibody probes, in **chapter 3** we sought to leverage our expertise in small molecule nerve specific fluorophore development and develop a direct administration methodology for the application of Oxazine 4, a promising candidate for further development of a NIR nerve specific fluorophore.[74] Nerve damage plagues surgical outcomes, with damage reported in up to 60% of patients in

common procedures such as the radical prostatectomy (RP).[6, 13, 14] Direct administration has additional advantages over systemic administration for application of Oxazine 4 fluorescence guided RP, since nerves within the prostate and renal fluorophore contrast would contribute significant background to identifying those nerve structures responsible for function.[61, 62, 163] In the work presented herein, a direct administration methodology was developed that provides equivalent to greater nerve signal to background ratios (SBRs) to systemic administration while yielding a significantly higher intensity fluorescence signal and requiring a substantially lower dose. In fact, the dose required for direct administration when scaled to humans falls within the microdosing requirements necessary for eIND regulatory guidance (<100 μg). The final direct administration methodology was shown to provide positive nerve contrast in autonomic nerve models, demonstrating the staining method's compatibility with nerves similar to those surrounding the prostate. The direct administration methodology developed herein provides a clinically viable administration protocol for nerve staining during FGS and provides a framework for clinical translation of novel nerve specific fluorophores.

While Oxazine 4 provides excellent nerve-specific contrast following direct or systemic administration, its fluorescence lies outside the NIR range ideal for FGS applications. NIR fluorescence (650-900 nm wavelength) provides increased penetration due to lower tissue chromophore absorption and emission for identifying buried targeted tissues and lower background due to autofluorescence.[24, 25] **Chapter 4** describes the screening of a library of novel oxazine derivatives with the goals of determining the factors responsible for nerve specificity and identifying candidate NIR nerve-specific fluorophores for clinical translation. From the library, 42 compounds possessed NIR fluorescence and 4 compounds were chosen as top candidates for clinical translation, with high nerve tissue fluorescence signals and nerve SBRs following both direct and systemic administration. Additionally, the compound that displayed the highest contrast in both screening methods, LGW01-08, was screened in large animals and provided the ability to identify nerve tissue buried beneath several millimeters of tissue. The library of novel oxazine derivatives developed and screened herein has yielded the first ever reported NIR nerve-specific small molecule fluorophores and contributed significantly toward clinical translation of a nerve specific fluorescent probe for FGS.

The direct administration methodology developed in **chapter 3** provided excellent nerve contrast in rodent nerve models. However, in preliminary large animal studies using laparoscopic surgical systems, the liquid co-solvent formulation caused significant background due to a lack of stain control and pooling from fluorophore runoff from the stained nerve site. Additionally, the co-solvent formulation is not FDA approved for clinical use and thus not viable for clinical translation of the novel nerve specific fluorophores developed in **chapter 4**. In **chapter 5**, gel-based formulations with FDA approval status and advantageous gelling characteristics for *in vivo* application were screened for direct administration of the lead NIR nerve specific fluorophore, LGW01-08. A clinically relevant Pluronics formulation was identified, with a unique liquid to solid transition that occurs rapidly once in contact with body temperature, that provided equivalent staining performance to the co-solvent formulation. The direct administration protocol was subsequently re-optimized for application of gel formulated LGW01-08 and large animal screening demonstrated a substantial improvement in stain control, yielding improved nerve SBR through decrease background resulting in the ability to identify buried nerve tissues. The gel formulation direct administration method allows for staining of complex tissue morphologies and tilt angles with no background due to runoff in just 1-2 minutes total staining time, which is compatible with the surgical workflow.

In some surgical applications, direct administration is not an ideal strategy for staining nerve tissue for FGS. For instance, when nerve tissue must be avoided during initial exposure of the main surgical site or when areas containing important nerve structures are not easily accessible for staining. Therefore, in **chapter 6**, we screened several clinically viable formulation strategies for systemic administration of the lead compound LGW01-08. A DSPE-PEG micelle formulation was identified as the most clinically relevant formulation, with FDA approval, high stability, and equivalent nerve contrast and signal intensities to the co-solvent formulation used previously. Additionally, toxicity testing, pharmacokinetics, biodistribution, and pharmacodynamics studies were performed to obtain useful preclinical information for the formulation/fluorophore combination and identify the clinical dose and imaging time point for systemic administration. The resulting nerve staining platform provides highly specific nerve fluorescence signal within 2 hours of administration with minimal toxicity and highly targeted uptake.

FUTURE PERSPECTIVES

Fluorescence guided surgery has the potential to improve surgical outcomes for many different procedures. In development of technologies and techniques to enable FGS for new applications, care must be taken to generate new probes and administration protocols capable of high specificity and sensitivity as well as improved clinical translation potential to traditional drug routes. The work presented herein utilizing direct administration as opposed to systemic administration provides improved sensitivity and selectivity while requiring lower doses for enhanced clinical translation. The application of this concept to other FGS technologies could provide improved success in both contrast generation and clinical translation. However, aspects of the direct administration methodology and tissue targeted probes presented herein require further study in order to ensure optimal performance clinically and provide an improved understanding of the mechanisms at play biologically and chemically.

First, in order to ensure the direct administration methodology provides adequate penetration to identify buried tissues, the tissue penetration of the developed staining methods should be assessed. Studies could be performed prospectively by staining targeted tissues covered with varying amounts of background muscle or adipose tissue and assessing the resulting contrast or retrospectively by excising tissues stained via direct administration and measuring the fluorescence intensity profiles caused by diffusion of the probes. Either method could be further analyzed through diffusion modelling to determine the diffusion coefficient of the probe, allowing for *in silico* simulation of fluorescence staining via direct administration.[179, 180]

Additionally, further large animal and human specimen screening is necessary to ensure the translatability of the technologies presented herein. Large animal porcine and canine models provide a good surrogate for the conditions and challenges encountered during human surgery, allowing for the identification of any additional optimization required. Human specimen staining ensures that positive results in animal models will translate well into clinical use through assessment of the probe staining patterns in comparison to *in vivo* animal studies. In both cases, positive specific contrast assessed via fluorescence imaging should always be

confirmed via histological analysis to confirm the relevant diagnostic potential of each technology.

For tumor targeted FGS technologies such as the DDSI method presented in **chapter 2**, adequate multiplexing abilities must be developed to ensure accurate assessment of tumor margin status in diverse patient tumors with heterogenous biomarker expression patterns. Several groups are utilizing novel imaging and Raman spectroscopy technologies to enable high levels of multiplexing.[98-101, 116] Additionally, small molecule drugs such as erlotinib, which targets EGFR, can be tagged with fluorescent probes to enable access to intracellular biomarker, which are far more numerous than extracellular biomarkers in cancers. New imaging systems capable of wide multiplexing will need to be introduced into clinical use in order to meet the need for multi-target cancer imaging.

In further clinical translation of nerve specific small molecule fluorophores, additional analysis of the library screening data presented herein and knowledge of the biomolecular target of the compounds will provide useful information about the chemical and biological mechanism behind nerve specificity. QSAR modelling will allow in depth analysis of the structural and physiochemical factors that modulate each compounds nerve uptake and specificity. Identification of the biomolecular target to which nerve specific oxazine compounds binds via proteomics and immunofluorescence investigation will provide further insight into the biochemical interactions that take place to afford the highly specific signal. Additionally, understanding the target of these compounds could open opportunities for drug targeting or neurodegenerative disease imaging applications.

CONCLUSION

Fluorescence guided surgery has the potential to revolutionize surgery and improve outcomes by enhancing visualization for repair or removal of damaged or diseased tissues and preservation of healthy vital structures. The studies described in this thesis have yielded novel targeted probes for tumor and nerve identification as well as improved formulation and administration strategies for rapid clinical translation. Using the innovations developed herein, we anticipate clinical translation of these FGS technologies within the next five years, a rapid timeline for novel probes.

REFERENCES

1. Meara, J.G. et al. Global Surgery 2030: evidence and solutions for achieving health, welfare, and economic development. *Lancet* **386**, 569-624 (2015).
2. Miller, K.D. et al. Cancer treatment and survivorship statistics, 2016. *CA Cancer J Clin* **66**, 271-289 (2016).
3. Bill-Axelson, A. et al. Radical prostatectomy versus watchful waiting in early prostate cancer. *The New England journal of medicine* **364**, 1708-1717 (2011).
4. Holst, K.A., Said, S.M., Nelson, T.J., Cannon, B.C. & Dearani, J.A. Current Interventional and Surgical Management of Congenital Heart Disease: Specific Focus on Valvular Disease and Cardiac Arrhythmias. *Circ Res* **120**, 1027-1044 (2017).
5. Bickler, S.N. et al. in Essential Surgery: Disease Control Priorities, Third Edition (Volume 1). (eds. H.T. Debas et al.) (Washington (DC); 2015).
6. Ghavamian, R., Knoll, A., Boczko, J. & Melman, A. Comparison of operative and functional outcomes of laparoscopic radical prostatectomy and radical retropubic prostatectomy: single surgeon experience. *Urology* **67**, 1241-1246 (2006).
7. Albertsen, P.C. Robot-assisted radical prostatectomy - fake innovation or the real deal? *European urology* **62**, 365-367 (2012).
8. Leal Ghezzi, T. & Campos Corleta, O. 30 Years of Robotic Surgery. *World J Surg* **40**, 2550-2557 (2016).
9. Tan, A. et al. Robotic surgery: disruptive innovation or unfulfilled promise? A systematic review and meta-analysis of the first 30 years. *Surg Endosc* **30**, 4330-4352 (2016).
10. Weissleder, R. & Pittet, M.J. Imaging in the era of molecular oncology. *Nature* **452**, 580-589 (2008).
11. Frangioni, J.V. New technologies for human cancer imaging. *Journal of clinical oncology : official journal of the American Society of Clinical Oncology* **26**, 4012-4021 (2008).
12. Jacobs, L. Positive margins: the challenge continues for breast surgeons. *Ann Surg Oncol* **15**, 1271-1272 (2008).
13. Antoniadis, G. et al. Iatrogenic nerve injuries: prevalence, diagnosis and treatment. *Dtsch Arztebl Int* **111**, 273-279 (2014).
14. Ficarra, V. et al. Systematic review and meta-analysis of studies reporting urinary continence recovery after robot-assisted radical prostatectomy. *Eur Urol* **62**, 405-417 (2012).
15. Lee, B.T. et al. The FLARE intraoperative near-infrared fluorescence imaging system: a first-in-human clinical trial in perforator flap breast reconstruction. *Plastic and reconstructive surgery* **126**, 1472-1481 (2010).
16. Tummers, Q.R. et al. Real-time intraoperative detection of breast cancer using near-infrared fluorescence imaging and Methylene Blue. *European journal of surgical oncology : the journal of the European Society of Surgical Oncology and the British Association of Surgical Oncology* **40**, 850-858 (2014).
17. Troyan, S.L. et al. The FLARE intraoperative near-infrared fluorescence imaging system: a first-in-human clinical trial in breast cancer sentinel lymph node mapping. *Annals of surgical oncology* **16**, 2943-2952 (2009).

18. Ashitate, Y., Stockdale, A., Choi, H.S., Laurence, R.G. & Frangioni, J.V. Real-time simultaneous near-infrared fluorescence imaging of bile duct and arterial anatomy. *The Journal of surgical research* **176**, 7-13 (2012).
19. Verbeek, F.P. et al. Intraoperative near infrared fluorescence guided identification of the ureters using low dose methylene blue: a first in human experience. *The Journal of urology* **190**, 574-579 (2013).
20. Gibbs-Strauss, S.L. et al. Nerve-highlighting fluorescent contrast agents for image-guided surgery. *Molecular imaging* **10**, 91-101 (2011).
21. Hirche, C. et al. An experimental study to evaluate the Fluobeam 800 imaging system for fluorescence-guided lymphatic imaging and sentinel node biopsy. *Surgical innovation* **20**, 516-523 (2013).
22. Gotoh, K. et al. A novel image-guided surgery of hepatocellular carcinoma by indocyanine green fluorescence imaging navigation. *Journal of surgical oncology* **100**, 75-79 (2009).
23. Kitagawa, H. et al. Visualization of the Stomach's Arterial Networks During Esophageal Surgery Using the HyperEye Medical System. *Anticancer research* **35**, 6201-6205 (2015).
24. Chance, B. Near-infrared images using continuous, phase-modulated, and pulsed light with quantitation of blood and blood oxygenation. *Annals of the New York Academy of Sciences* **838**, 29-45 (1998).
25. Gibbs, S.L. Near infrared fluorescence for image-guided surgery. *Quantitative imaging in medicine and surgery* **2**, 177-187 (2012).
26. Kitai, T., Inomoto, T., Miwa, M. & Shikayama, T. Fluorescence navigation with indocyanine green for detecting sentinel lymph nodes in breast cancer. *Breast Cancer* **12**, 211-215 (2005).
27. Peek, M.C., Charalampoudis, P., Anninga, B., Baker, R. & Douek, M. Blue dye for identification of sentinel nodes in breast cancer and malignant melanoma: a systematic review and meta-analysis. *Future Oncol* **13**, 455-467 (2017).
28. Jeschke, S. et al. Visualisation of the lymph node pathway in real time by laparoscopic radioisotope- and fluorescence-guided sentinel lymph node dissection in prostate cancer staging. *Urology* **80**, 1080-1086 (2012).
29. Chang, D.W., Suami, H. & Skoracki, R. A prospective analysis of 100 consecutive lymphovenous bypass cases for treatment of extremity lymphedema. *Plastic and reconstructive surgery* **132**, 1305-1314 (2013).
30. Yamamoto, M. et al. Indocyanine green angiography for intra-operative assessment in vascular surgery. *Eur J Vasc Endovasc Surg* **43**, 426-432 (2012).
31. Boni, L. et al. Clinical applications of indocyanine green (ICG) enhanced fluorescence in laparoscopic surgery. *Surg Endosc* **29**, 2046-2055 (2015).
32. Stummer, W. et al. Intraoperative detection of malignant gliomas by 5-aminolevulinic acid-induced porphyrin fluorescence. *Neurosurgery* **42**, 518-525; discussion 525-516 (1998).
33. Stummer, W. et al. Fluorescence-guided surgery with 5-aminolevulinic acid for resection of malignant glioma: a randomised controlled multicentre phase III trial. *Lancet Oncol* **7**, 392-401 (2006).

34. van Dam, G.M. et al. Intraoperative tumor-specific fluorescence imaging in ovarian cancer by folate receptor-alpha targeting: first in-human results. *Nat Med* **17**, 1315-1319 (2011).
35. van der Vorst, J.R. et al. Near-infrared fluorescence imaging of a solitary fibrous tumor of the pancreas using methylene blue. *World J Gastrointest Surg* **4**, 180-184 (2012).
36. Al-Taher, M., van den Bos, J., Schols, R.M., Bouvy, N.D. & Stassen, L.P. Fluorescence Ureteral Visualization in Human Laparoscopic Colorectal Surgery Using Methylene Blue. *J Laparoendosc Adv Surg Tech A* **26**, 870-875 (2016).
37. Ankersmit, M. et al. Fluorescent Imaging With Indocyanine Green During Laparoscopic Cholecystectomy in Patients at Increased Risk of Bile Duct Injury. *Surgical innovation* **24**, 245-252 (2017).
38. Samkoe, K.S. et al. Application of Fluorescence-Guided Surgery to Subsurface Cancers Requiring Wide Local Excision: Literature Review and Novel Developments Toward Indirect Visualization. *Cancer Control* **25**, 1073274817752332 (2018).
39. Hadjipanayis, C.G., Widhalm, G. & Stummer, W. What is the Surgical Benefit of Utilizing 5-Aminolevulinic Acid for Fluorescence-Guided Surgery of Malignant Gliomas? *Neurosurgery* **77**, 663-673 (2015).
40. Rosenthal, E.L. et al. Successful Translation of Fluorescence Navigation During Oncologic Surgery: A Consensus Report. *J Nucl Med* **57**, 144-150 (2016).
41. Pogue, B.W. et al. Advancing Molecular-Guided Surgery through probe development and testing in a moderate cost evaluation pipeline. *Proc SPIE Int Soc Opt Eng* **9311** (2015).
42. Yamashita, S. & Sugiyama, Y. New strategy for drug development with exploratory IND studies: scientific basis and future directions. *Advanced drug delivery reviews* **63**, 493 (2011).
43. Samkoe, K.S. et al. Toxicity and Pharmacokinetic Profile for Single-Dose Injection of ABY-029: a Fluorescent Anti-EGFR Synthetic Affibody Molecule for Human Use. *Molecular imaging and biology : MIB : the official publication of the Academy of Molecular Imaging* **19**, 512-521 (2017).
44. Elliott, J.T. et al. Microdose fluorescence imaging of ABY-029 on an operating microscope adapted by custom illumination and imaging modules. *Biomed Opt Express* **7**, 3280-3288 (2016).
45. Pawlik, T.M. et al. Effect of surgical margin status on survival and site of recurrence after hepatic resection for colorectal metastases. *Ann Surg* **241**, 715-722, discussion 722-714 (2005).
46. Murakami, Y. et al. Prognostic significance of lymph node metastasis and surgical margin status for distal cholangiocarcinoma. *Journal of surgical oncology* **95**, 207-212 (2007).
47. Huang, D.T., Johnson, C.R., Schmidt-Ullrich, R. & Grimes, M. Postoperative radiotherapy in head and neck carcinoma with extracapsular lymph node extension and/or positive resection margins: a comparative study. *Int J Radiat Oncol Biol Phys* **23**, 737-742 (1992).
48. Waljee, J.F., Hu, E.S., Newman, L.A. & Alderman, A.K. Predictors of re-excision among women undergoing breast-conserving surgery for cancer. *Annals of surgical oncology* **15**, 1297-1303 (2008).

49. Wilke, L.G. et al. Repeat surgery after breast conservation for the treatment of stage 0 to II breast carcinoma: a report from the National Cancer Data Base, 2004-2010. *JAMA Surg* **149**, 1296-1305 (2014).
50. Jeevan, R. et al. Reoperation rates after breast conserving surgery for breast cancer among women in England: retrospective study of hospital episode statistics. *Bmj* **345**, e4505 (2012).
51. Freedman, G. et al. Patients with early stage invasive cancer with close or positive margins treated with conservative surgery and radiation have an increased risk of breast recurrence that is delayed by adjuvant systemic therapy. *Int J Radiat Oncol Biol Phys* **44**, 1005-1015 (1999).
52. Davis, S.C., Gibbs, S.L., Gunn, J.R. & Pogue, B.W. Topical dual-stain difference imaging for rapid intra-operative tumor identification in fresh specimens. *Opt Lett* **38**, 5184-5187 (2013).
53. Bouyer-Ferullo, S. Preventing perioperative peripheral nerve injuries. *AORN J* **97**, 110-124 e119 (2013).
54. Walz, J., Graefen, M. & Huland, H. Basic principles of anatomy for optimal surgical treatment of prostate cancer. *World journal of urology* **25**, 31-38 (2007).
55. Lopez, A. et al. Intraoperative Optical Biopsy during Robotic Assisted Radical Prostatectomy Using Confocal Endomicroscopy. *The Journal of urology* **195**, 1110-1117 (2016).
56. Boyette, L.B. et al. Fiberoptic imaging of cavernous nerves in vivo. *The Journal of urology* **178**, 2694-2700 (2007).
57. Rais-Bahrami, S. et al. Optical coherence tomography of cavernous nerves: a step toward real-time intraoperative imaging during nerve-sparing radical prostatectomy. *Urology* **72**, 198-204 (2008).
58. Aron, M. et al. Second prize: preliminary experience with the Niris optical coherence tomography system during laparoscopic and robotic prostatectomy. *J Endourol* **21**, 814-818 (2007).
59. Ukimura, O., Magi-Galluzzi, C. & Gill, I.S. Real-time transrectal ultrasound guidance during laparoscopic radical prostatectomy: impact on surgical margins. *The Journal of urology* **175**, 1304-1310 (2006).
60. Ponnusamy, K., Sorger, J.M. & Mohr, C. Nerve mapping for prostatectomies: novel technologies under development. *J Endourol* **26**, 769-777 (2012).
61. Tewari, A. et al. The proximal neurovascular plate and the tri-zonal neural architecture around the prostate gland: importance in the athermal robotic technique of nerve-sparing prostatectomy. *BJU international* **98**, 314-323 (2006).
62. Patel, V.R. et al. The role of the prostatic vasculature as a landmark for nerve sparing during robot-assisted radical prostatectomy. *Eur Urol* **61**, 571-576 (2012).
63. Barth, C.W. & Gibbs, S.L. Direct Administration of Nerve-Specific Contrast to Improve Nerve Sparing Radical Prostatectomy. *Theranostics* **7**, 573-593 (2017).
64. Wu, C. et al. Molecular probes for imaging myelinated white matter in CNS. *Journal of medicinal chemistry* **51**, 6682-6688 (2008).
65. Wang, C. et al. In situ fluorescence imaging of myelination. *The journal of histochemistry and cytochemistry : official journal of the Histochemistry Society* **58**, 611-621 (2010).

66. Gibbs, S.L. et al. Structure-activity relationship of nerve-highlighting fluorophores. *PloS one* **8**, e73493 (2013).
67. Stankoff, B. et al. Imaging of CNS myelin by positron-emission tomography. *Proceedings of the National Academy of Sciences of the United States of America* **103**, 9304-9309 (2006).
68. Cotero, V.E. et al. Intraoperative fluorescence imaging of peripheral and central nerves through a myelin-selective contrast agent. *Molecular imaging and biology : MIB : the official publication of the Academy of Molecular Imaging* **14**, 708-717 (2012).
69. Cotero, V.E. et al. Improved Intraoperative Visualization of Nerves through a Myelin-Binding Fluorophore and Dual-Mode Laparoscopic Imaging. *PloS one* **10**, e0130276 (2015).
70. Bajaj, A. et al. Identification of the protein target of myelin-binding ligands by immunohistochemistry and biochemical analyses. *The journal of histochemistry and cytochemistry : official journal of the Histochemistry Society* **61**, 19-30 (2013).
71. Gibbs-Strauss, S.L. et al. Molecular imaging agents specific for the annulus fibrosus of the intervertebral disk. *Molecular imaging* **9**, 128-140 (2010).
72. Meyers, J.R. et al. Lighting up the senses: FM1-43 loading of sensory cells through nonselective ion channels. *The Journal of neuroscience : the official journal of the Society for Neuroscience* **23**, 4054-4065 (2003).
73. Wang, C. et al. Longitudinal near-infrared imaging of myelination. *The Journal of neuroscience : the official journal of the Society for Neuroscience* **31**, 2382-2390 (2011).
74. Park, M.H. et al. Prototype nerve-specific near-infrared fluorophores. *Theranostics* **4**, 823-833 (2014).
75. Jorns, J.M. et al. Intraoperative frozen section analysis of margins in breast conserving surgery significantly decreases reoperative rates: one-year experience at an ambulatory surgical center. *Am J Clin Pathol* **138**, 657-669 (2012).
76. Valdes, E.K., Boolbol, S.K., Cohen, J.M. & Feldman, S.M. Intra-operative touch preparation cytology; does it have a role in re-excision lumpectomy? *Annals of surgical oncology* **14**, 1045-1050 (2007).
77. Ihrai, T. et al. Intraoperative radiological margin assessment in breast-conserving surgery. *European journal of surgical oncology : the journal of the European Society of Surgical Oncology and the British Association of Surgical Oncology* **40**, 449-453 (2014).
78. Moschetta, M. et al. Role of specimen US for predicting resection margin status in breast conserving therapy. *Il Giornale di chirurgia* **36**, 201-204 (2015).
79. Rivera, R.J., Holmes, D.R. & Tafra, L. Analysis of the Impact of Intraoperative Margin Assessment with Adjunctive Use of MarginProbe versus Standard of Care on Tissue Volume Removed. *Int J Surg Oncol* **2012**, 868623 (2012).
80. Singletary, S.E. Surgical margins in patients with early-stage breast cancer treated with breast conservation therapy. *Am J Surg* **184**, 383-393 (2002).
81. Esbona, K., Li, Z. & Wilke, L.G. Intraoperative imprint cytology and frozen section pathology for margin assessment in breast conservation surgery: a systematic review. *Annals of surgical oncology* **19**, 3236-3245 (2012).
82. Riedl, O. et al. Intraoperative frozen section analysis for breast-conserving therapy in 1016 patients with breast cancer. *European journal of surgical oncology : the journal of the European Society of Surgical Oncology and the British Association of Surgical Oncology* **35**, 264-270 (2009).

83. Saarela, A.O., Paloneva, T.K., Rissanen, T.J. & Kiviniemi, H.O. Determinants of positive histologic margins and residual tumor after lumpectomy for early breast cancer: a prospective study with special reference to touch preparation cytology. *Journal of surgical oncology* **66**, 248-253 (1997).
84. Jorns, J.M., Daignault, S., Sabel, M.S. & Wu, A.J. Is intraoperative frozen section analysis of reexcision specimens of value in preventing reoperation in breast-conserving therapy? *Am J Clin Pathol* **142**, 601-608 (2014).
85. Cendan, J.C., Coco, D. & Copeland, E.M., 3rd Accuracy of intraoperative frozen-section analysis of breast cancer lumpectomy-bed margins. *Journal of the American College of Surgeons* **201**, 194-198 (2005).
86. Osako, T. et al. Efficacy of intraoperative entire-circumferential frozen section analysis of lumpectomy margins during breast-conserving surgery for breast cancer. *Int J Clin Oncol* **20**, 1093-1101 (2015).
87. Blohmer, J.U. et al. MarginProbe(c) reduces the rate of re-excision following breast conserving surgery for breast cancer. *Arch Gynecol Obstet* **294**, 361-367 (2016).
88. Gray, R.J., Pockaj, B.A., Garvey, E. & Blair, S. Intraoperative Margin Management in Breast-Conserving Surgery: A Systematic Review of the Literature. *Annals of surgical oncology* (2017).
89. Giacomelli, M.G., Sheikine, Y., Vardeh, H., Connolly, J.L. & Fujimoto, J.G. Rapid imaging of surgical breast excisions using direct temporal sampling two photon fluorescent lifetime imaging. *Biomed Opt Express* **6**, 4317-4325 (2015).
90. Tao, Y.K. et al. Assessment of breast pathologies using nonlinear microscopy. *Proceedings of the National Academy of Sciences of the United States of America* **111**, 15304-15309 (2014).
91. Bydlon, T.M. et al. Advancing optical imaging for breast margin assessment: an analysis of excisional time, cautery, and patent blue dye on underlying sources of contrast. *PloS one* **7**, e51418 (2012).
92. Sharma, V. et al. Auto-fluorescence lifetime and light reflectance spectroscopy for breast cancer diagnosis: potential tools for intraoperative margin detection. *Biomed Opt Express* **3**, 1825-1840 (2012).
93. Kong, K. et al. Diagnosis of tumors during tissue-conserving surgery with integrated autofluorescence and Raman scattering microscopy. *Proceedings of the National Academy of Sciences of the United States of America* **110**, 15189-15194 (2013).
94. Assayag, O. et al. Large field, high resolution full-field optical coherence tomography: a pre-clinical study of human breast tissue and cancer assessment. *Technol Cancer Res Treat* **13**, 455-468 (2014).
95. Erickson-Bhatt, S.J. et al. Real-time Imaging of the Resection Bed Using a Handheld Probe to Reduce Incidence of Microscopic Positive Margins in Cancer Surgery. *Cancer Res* **75**, 3706-3712 (2015).
96. Erickson-Bhatt, S.J. et al. Noninvasive Surface Imaging of Breast Cancer in Humans using a Hand-held Optical Imager. *Biomed Phys Eng Express* **1** (2015).
97. Liu, J., Guo, W. & Tong, M. Intraoperative indocyanine green fluorescence guidance for excision of nonpalpable breast cancer. *World J Surg Oncol* **14**, 266 (2016).
98. Kang, S., Wang, Y., Reder, N.P. & Liu, J.T. Multiplexed Molecular Imaging of Biomarker-Targeted SERS Nanoparticles on Fresh Tissue Specimens with Channel-Compressed Spectrometry. *PloS one* **11**, e0163473 (2016).

99. Wang, Y., Kang, S., Doerksen, J.D., Glaser, A.K. & Liu, J.T. Surgical Guidance via Multiplexed Molecular Imaging of Fresh Tissues Labeled with SERS-Coded Nanoparticles. *IEEE journal of selected topics in quantum electronics : a publication of the IEEE Lasers and Electro-optics Society* **22** (2016).
100. Wang, Y. et al. Quantitative molecular phenotyping with topically applied SERS nanoparticles for intraoperative guidance of breast cancer lumpectomy. *Sci Rep* **6**, 21242 (2016).
101. Wang, Y.W. et al. Multiplexed Molecular Imaging of Fresh Tissue Surfaces Enabled by Convection-Enhanced Topical Staining with SERS-Coded Nanoparticles. *Small* **12**, 5612-5621 (2016).
102. Wang, Y.W., Kang, S., Khan, A., Bao, P.Q. & Liu, J.T. In vivo multiplexed molecular imaging of esophageal cancer via spectral endoscopy of topically applied SERS nanoparticles. *Biomed Opt Express* **6**, 3714-3723 (2015).
103. Chi, C. et al. Intraoperative imaging-guided cancer surgery: from current fluorescence molecular imaging methods to future multi-modality imaging technology. *Theranostics* **4**, 1072-1084 (2014).
104. Urano, Y. et al. Rapid cancer detection by topically spraying a gamma-glutamyltranspeptidase-activated fluorescent probe. *Sci Transl Med* **3**, 110ra119 (2011).
105. Cutter, J.L. et al. Topical application of activity-based probes for visualization of brain tumor tissue. *PloS one* **7**, e33060 (2012).
106. Achilefu, S. Rapid response activatable molecular probes for intraoperative optical image-guided tumor resection. *Hepatology* **56**, 1170-1173 (2012).
107. Sinha, L. et al. Quantification of the binding potential of cell-surface receptors in fresh excised specimens via dual-probe modeling of SERS nanoparticles. *Sci Rep* **5**, 8582 (2015).
108. Choi, H.S. et al. Targeted zwitterionic near-infrared fluorophores for improved optical imaging. *Nature biotechnology* **31**, 148-153 (2013).
109. Benz, C.C. et al. Estrogen-dependent, tamoxifen-resistant tumorigenic growth of MCF-7 cells transfected with HER2/neu. *Breast Cancer Res Treat* **24**, 85-95 (1992).
110. Swinehart, D.F. The Beer-Lambert Law. *Journal of Chemical Education* **39**, 333 (1962).
111. Barth, C.W. & Gibbs, S.L., Vol. 9696 96960R-96960R-96968 (2016).
112. Hackman, K.M. et al. Polymeric Micelles as Carriers for Nerve-Highlighting Fluorescent Probe Delivery. *Molecular pharmaceutics* (2015).
113. Cho, H.S. et al. Structure of the extracellular region of HER2 alone and in complex with the Herceptin Fab. *Nature* **421**, 756-760 (2003).
114. Hanley, J.A. & McNeil, B.J. A method of comparing the areas under receiver operating characteristic curves derived from the same cases. *Radiology* **148**, 839-843 (1983).
115. Choi, H.S. et al. Synthesis and in vivo fate of zwitterionic near-infrared fluorophores. *Angew Chem Int Ed Engl* **50**, 6258-6263 (2011).
116. Wang, Y. et al. Raman-encoded molecular imaging (REMI) with topically applied SERS nanoparticles for intraoperative guidance of lumpectomy. *Cancer Res* (2017).
117. Wolff, A.C. et al. Recommendations for human epidermal growth factor receptor 2 testing in breast cancer: American Society of Clinical Oncology/College of American Pathologists clinical practice guideline update. *Arch Pathol Lab Med* **138**, 241-256 (2014).

118. Hammond, M.E. et al. American Society of Clinical Oncology/College of American Pathologists guideline recommendations for immunohistochemical testing of estrogen and progesterone receptors in breast cancer. *Arch Pathol Lab Med* **134**, 907-922 (2010).
119. Moran, M.S. et al. Society of Surgical Oncology-American Society for Radiation Oncology consensus guideline on margins for breast-conserving surgery with whole-breast irradiation in stages I and II invasive breast cancer. *Journal of clinical oncology : official journal of the American Society of Clinical Oncology* **32**, 1507-1515 (2014).
120. Siegel, R., Ma, J., Zou, Z. & Jemal, A. Cancer statistics, 2014. *CA: a cancer journal for clinicians* **64**, 9-29 (2014).
121. Jacobs, B.L. et al. Use of advanced treatment technologies among men at low risk of dying from prostate cancer. *Jama* **309**, 2587-2595 (2013).
122. Bill-Axelson, A. et al. Radical prostatectomy or watchful waiting in early prostate cancer. *The New England journal of medicine* **370**, 932-942 (2014).
123. Abdollah, F. et al. Comparison of mortality outcomes after radical prostatectomy versus radiotherapy in patients with localized prostate cancer: a population-based analysis. *International journal of urology : official journal of the Japanese Urological Association* **19**, 836-844 (2012).
124. Sooriakumaran, P. et al. Comparative effectiveness of radical prostatectomy and radiotherapy in prostate cancer: observational study of mortality outcomes. *Bmj* **348**, g1502 (2014).
125. Hoffman, R.M. et al. Mortality after radical prostatectomy or external beam radiotherapy for localized prostate cancer. *Journal of the National Cancer Institute* **105**, 711-718 (2013).
126. Walsh, P.C. & Donker, P.J. Impotence following radical prostatectomy: insight into etiology and prevention. *The Journal of urology* **128**, 492-497 (1982).
127. Ficarra, V. et al. Systematic review and meta-analysis of studies reporting potency rates after robot-assisted radical prostatectomy. *Eur Urol* **62**, 418-430 (2012).
128. Damber, J.E. & Khatami, A. Surgical treatment of localized prostate cancer. *Acta oncologica* **44**, 599-604 (2005).
129. Tewari, A. et al. An Operative and Anatomic Study to Help in Nerve Sparing during Laparoscopic and Robotic Radical Prostatectomy. *European Urology* **43**, 444-454 (2003).
130. Gioux, S., Choi, H.S. & Frangioni, J.V. Image-guided surgery using invisible near-infrared light: fundamentals of clinical translation. *Molecular imaging* **9**, 237-255 (2010).
131. Vahrmeijer, A.L., Hutteman, M., van der Vorst, J.R., van de Velde, C.J. & Frangioni, J.V. Image-guided cancer surgery using near-infrared fluorescence. *Nature reviews. Clinical oncology* **10**, 507-518 (2013).
132. Tozburun, S. et al. Temperature-controlled optical stimulation of the rat prostate cavernous nerves. *Journal of biomedical optics* **18**, 067001 (2013).
133. Tozburun, S., Lagoda, G.A., Burnett, A.L. & Fried, N.M. Continuous-wave laser stimulation of the rat prostate cavernous nerves using a compact and inexpensive all single mode optical fiber system. *J Endourol* **25**, 1727-1731 (2011).
134. Tozburun, S. et al. Continuous-wave infrared subsurface optical stimulation of the rat prostate cavernous nerves using a 1490-nm diode laser. *Urology* **82**, 969-973 (2013).
135. Tozburun, S., Lagoda, G.A., Burnett, A.L. & Fried, N.M. Subsurface near-infrared laser stimulation of the periprostatic cavernous nerves. *J Biophotonics* **5**, 793-800 (2012).

136. Walz, J. et al. A critical analysis of the current knowledge of surgical anatomy related to optimization of cancer control and preservation of continence and erection in candidates for radical prostatectomy. *Eur Urol* **57**, 179-192 (2010).
137. Walz, J. et al. A Critical Analysis of the Current Knowledge of Surgical Anatomy of the Prostate Related to Optimisation of Cancer Control and Preservation of Continence and Erection in Candidates for Radical Prostatectomy: An Update. *Eur Urol* **70**, 301-311 (2016).
138. Stolzenburg, J.U. et al. Endoscopic extraperitoneal radical prostatectomy: initial experience after 70 procedures. *The Journal of urology* **169**, 2066-2071 (2003).
139. Costello, A.J., Brooks, M. & Cole, O.J. Anatomical studies of the neurovascular bundle and cavernosal nerves. *BJU international* **94**, 1071-1076 (2004).
140. Bonilla, E. & Prelle, A. Application of nile blue and nile red, two fluorescent probes, for detection of lipid droplets in human skeletal muscle. *Journal of Histochemistry & Cytochemistry* **35**, 619-621 (1987).
141. Fowler, S.D. & Greenspan, P. Application of Nile red, a fluorescent hydrophobic probe, for the detection of neutral lipid deposits in tissue sections: comparison with oil red O. *The journal of histochemistry and cytochemistry : official journal of the Histochemistry Society* **33**, 833-836 (1985).
142. Greenspan, P. & Fowler, S.D. Spectrofluorometric studies of the lipid probe, nile red. *Journal of lipid research* **26**, 781-789 (1985).
143. Greenspan, P., Mayer, E.P. & Fowler, S.D. Nile red: a selective fluorescent stain for intracellular lipid droplets. *The Journal of cell biology* **100**, 965-973 (1985).
144. Maeder, U. et al. Evaluation and quantification of spectral information in tissue by confocal microscopy. *Journal of biomedical optics* **17**, 106011 (2012).
145. Schneider, C.A., Rasband, W.S. & Eliceiri, K.W. NIH Image to ImageJ: 25 years of image analysis. *Nat Methods* **9**, 671-675 (2012).
146. Kim, S.W., Lee, S.H. & Paick, J.S. In vivo rat model to measure hypogastric nerve stimulation-induced seminal vesicle and vasal pressure responses simultaneously. *Int J Impot Res* **16**, 427-432 (2004).
147. Diaz, R. et al. Histological modifications of the rat prostate following transection of somatic and autonomic nerves. *Anais da Academia Brasileira de Ciências* **82**, 397-404 (2010).
148. . (ed. S. Pasteur) (2015).
149. Nema, S.L., John D. Pharmaceutical Dosage Forms - Parenteral Medications, Third Edition: Volume 3: Regulations, Validation and the Future. (Informa Healthcare, 119 Farringdon Road, London EC1R 3DA, UK; 2010).
150. . (ed. F.a.D.A. US Department of Health and Human Services, Center for Drug Evaluation and Research) (Washington DC, USA; 2006).
151. . (ed. F.a.D.A. US Department of Health and Human Services, Center for Drug Evaluation and Research) (Washington DC, USA; 2005).
152. Diaz, R. et al. Histological modifications of the rat prostate following transection of somatic and autonomic nerves. *An Acad Bras Cienc* **82**, 397-404 (2010).
153. Liatsikos, E. et al. Prevention and management of perioperative complications in laparoscopic and endoscopic radical prostatectomy. *World journal of urology* **26**, 571-580 (2008).

154. Burke, S. & Shorten, G.D. When pain after surgery doesn't go away. *Biochem Soc Trans* **37**, 318-322 (2009).
155. Zhang, J., Moore, A.E. & Stringer, M.D. Iatrogenic upper limb nerve injuries: a systematic review. *ANZ journal of surgery* **81**, 227-236 (2011).
156. Li, R. et al. Peripheral nerve injuries treatment: a systematic review. *Cell Biochem Biophys* **68**, 449-454 (2014).
157. Ahlering, T.E., Eichel, L. & Skarecky, D. Evaluation of long-term thermal injury using cautery during nerve sparing robotic prostatectomy. *Urology* **72**, 1371-1374 (2008).
158. Fagerholm, U. The highly permeable blood-brain barrier: an evaluation of current opinions about brain uptake capacity. *Drug Discov Today* **12**, 1076-1082 (2007).
159. Waterhouse, R.N. Determination of lipophilicity and its use as a predictor of blood-brain barrier penetration of molecular imaging agents. *Molecular imaging and biology : MIB : the official publication of the Academy of Molecular Imaging* **5**, 376-389 (2003).
160. Lipinski, C.A., Lombardo, F., Dominy, B.W. & Feeney, P.J. Experimental and computational approaches to estimate solubility and permeability in drug discovery and development settings. *Advanced drug delivery reviews* **46**, 3-26 (2001).
161. Veber, D.F. et al. Molecular properties that influence the oral bioavailability of drug candidates. *Journal of medicinal chemistry* **45**, 2615-2623 (2002).
162. Pajouhesh, H. & Lenz, G.R. Medicinal chemical properties of successful central nervous system drugs. *NeuroRx* **2**, 541-553 (2005).
163. Barth, C.W.G., Summer L. Direct Administration of Nerve-Specific Contrast to Improve Nerve Sparing Radical Prostatectomy. *Theranostics* (2016).
164. Lee, K.Y. & Mooney, D.J. Alginate: properties and biomedical applications. *Prog Polym Sci* **37**, 106-126 (2012).
165. Bouhadir, K.H., Alsberg, E. & Mooney, D.J. Hydrogels for combination delivery of antineoplastic agents. *Biomaterials* **22**, 2625-2633 (2001).
166. Nie, S., Hsiao, W.L., Pan, W. & Yang, Z. Thermoreversible Pluronic F127-based hydrogel containing liposomes for the controlled delivery of paclitaxel: in vitro drug release, cell cytotoxicity, and uptake studies. *Int J Nanomedicine* **6**, 151-166 (2011).
167. Diniz, I.M. et al. Pluronic F-127 hydrogel as a promising scaffold for encapsulation of dental-derived mesenchymal stem cells. *J Mater Sci Mater Med* **26**, 153 (2015).
168. Suntornnond, R., Tan, E.Y.S., An, J. & Chua, C.K. A highly printable and biocompatible hydrogel composite for direct printing of soft and perfusable vasculature-like structures. *Sci Rep* **7**, 16902 (2017).
169. Stolzenburg, J.-U. et al. Hemostasis during nerve-sparing endoscopic extraperitoneal radical prostatectomy. *Journal of endourology* **24**, 505-509 (2010).
170. Liatsikos, E.N., Katsakiori, P. & Stolzenburg, J.-U. in Endoscopic Extraperitoneal Radical Prostatectomy 135-142 (Springer, 2007).
171. Unosson, J., Montufar, E.B., Engqvist, H., Ginebra, M.P. & Persson, C. Brushite foams--the effect of Tween(R) 80 and Pluronic(R) F-127 on foam porosity and mechanical properties. *J Biomed Mater Res B Appl Biomater* **104**, 67-77 (2016).
172. Oerlemans, C. et al. Polymeric micelles in anticancer therapy: targeting, imaging and triggered release. *Pharmaceutical research* **27**, 2569-2589 (2010).
173. Allen, T.M. & Cullis, P.R. Liposomal drug delivery systems: from concept to clinical applications. *Advanced drug delivery reviews* **65**, 36-48 (2013).

174. Moore, G.E., Peyton, W.T. & et al. The clinical use of fluorescein in neurosurgery; the localization of brain tumors. *J Neurosurg* **5**, 392-398 (1948).
175. Sheridan, R.L. et al. Burn depth estimation by use of indocyanine green fluorescence: initial human trial. *J Burn Care Rehabil* **16**, 602-604 (1995).
176. Hongo, K., Kobayashi, S., Okudera, H., Hokama, M. & Nakagawa, F. Noninvasive cerebral optical spectroscopy: depth-resolved measurements of cerebral haemodynamics using indocyanine green. *Neurol Res* **17**, 89-93 (1995).
177. Scheider, A. [Indocyanine green angiography with an infrared scanning laser ophthalmoscope. Initial clinical experiences]. *Ophthalmologe* **89**, 27-33 (1992).
178. Arens, C., Malzahn, K., Dias, O., Andrea, M. & Glanz, H. [Endoscopic imaging techniques in the diagnosis of laryngeal carcinoma and its precursor lesions]. *Laryngorhinootologie* **78**, 685-691 (1999).
179. Kang, S. et al. Microscopic investigation of" topically applied nanoparticles for molecular imaging of fresh tissue surfaces. *J Biophotonics* **11**, e201700246 (2018).
180. Xu, X., Wang, Y., Xiang, J., Liu, J.T.C. & Tichauer, K.M. Rinsing paired-agent model (RPAM) to quantify cell-surface receptor concentrations in topical staining applications of thick tissues. *Phys Med Biol* **62**, 5098-5113 (2017).